

ELECTROCHEMICAL CHARACTERIZATIONS OF NEGATIVE LEAD ELECTRODE IN LEAD-ACID BATTERY

by
Nikhil Milind Chaudhari

A thesis submitted to the Materials Science and Engineering Program,
Cullen College of Engineering
in partial fulfillment of the requirements for the degree of

DOCTOR OF PHILOSOPHY

in Materials Science and Engineering

Chair of Committee: Dr. Stanko R. Brankovic

Committee Member: Dr. Francisco C. Robles Hernandez

Committee Member: Dr. Yan Yao

Committee Member: Dr. Jiming Bao

Committee Member: Dr. Pietro Papa Lopes

Committee Member: Dr. Vojislav Stamenkovic

University of Houston
December 2021

Copyright 2021, Nikhil Milind Chaudhari

DEDICATIONS

I would like to dedicate my work and this PhD dissertation in loving memory of both my uncle, 'Dr. Prashant P. Chaudhari' and my grandfather, 'Dr. Pralhad M. Chaudhari' who gave me courage to face the challenges and succeed in anything I choose to pursue.

ACKNOWLEDGEMENT

First and foremost, I would like to express my sincere gratitude to my PhD research advisor, Dr. Stanko R. Brankovic, for his support, guidance, and encouragement in advancing research during my work while pursuing my PhD. He is one of the most knowledgeable leading experts in electrochemical field and I am grateful to have learned from him. I will never forget all the motivational discussions with him in the labs and in weekly group meetings.

I would also like to thank my co-advisor, Dr. Fransico C. Robles Hernandez for his advice and guidance in projects carried out while working as a graduate student. He has helped me greatly to acquire many skills by accepting me as his teaching assistance and allowing access to variety of equipment in his labs. I would also like to thank my committee members Dr. Yan Yao, Dr. Kiming Bao for being on my PhD dissertation committee.

I would like to express my gratitude to Dr. Vojislav Stamenkovic, to have had an opportunity to collaborate and work with him and his group at Argonne National Laboratory. I will always remember his inspirational talks during our meetings. It was a delightful experience to work with Dr. Pietro Papa Lopes on Lead-acid battery science research project. He has helped me understand many advanced techniques through fruitful discussions on my work. I appreciate the tips and tricks by Dr. Lopes that helped me in solving problems and develop my ability to interpret information from experimental data.

I am thankful for all the support I have gotten from my former colleagues Dr. Dongjun Wu, Dr. Kamyar Ahmadi who helped me use and maintain lab equipment. I appreciate my current labmates Dhaivat Solanki and Crystal Ferels for helping me in the lab.

I am eternally grateful to my family for their unending love and giving me courage to achieve my goals. I would like to specially thank my loving wife, Purva Chopde for believing in me and filling my life with joy and excitement. I am lucky to have my friends Dr. Ujwal Patil and Dr. Dimple Chavan-Patil who are always there for me during the ups and downs.

ABSTRACT

The energy demands of the growing world are increasing at a fast rate and storage of energy is of extreme importance for many industrial and household applications. Batteries are proving to very useful in energy storage and providing power for applications ranging from portable devices to EVs for transportation. Until recently, Lead-acid batteries were the most used and successful for storing energy, and are used in many applications like UPS system, SLI systems in cars, and for industrial power applications. As the demand for high performance batteries is constantly increasing, Lead-acid batteries are in desperate need of advancements so that maximum efficiency and performance can be achieved since with the lead-acid batteries in use right now, only 30 – 40 % of the theoretical efficiency is achieved. Lead-acid battery has some unique advantages such as about 99.9 % recyclability, low cost, wide operating temperature range and lower risk of explosion.

The work included in this dissertation is aimed toward exploring the fundamentals of lead-acid battery electrochemistry using advanced techniques developed in recent past which will help improve their performance. The focus of this work is on understanding and establishing baseline performance of negative lead electrode with variation in temperature. The discharge and kinetic charge acceptance of Pb electrode is explored for a wide range of temperature to understand the performance limits and performance controlling parameters. The cyclic voltammetry electrochemical procedures are established and used for studying discharge and charge processes of Pb electrode. Double layer capacitance

measurement for electrochemically polished Pb surface is used as a metric for lead surface area. Quantification of performance of Pb electrode is evaluated using modified Peukert relationship and Kinetic charge acceptance measured from cyclic voltammetry data. Passivation of lead electrode during discharge forms $PbSO_4$ layer and dissolution of this layer is a limiting process for recharging the electrode. Morphology of $PbSO_4$ layer is related to its dissolution. Here, a relationship of $PbSO_4$ thickness and particle size to discharge capacity and charge acceptance is observed. Therefore, morphology and thickness of $PbSO_4$ layer after discharge at various temperatures is studied using microscopy techniques such as conductive Atomic Force Microscopy and Focused Ion Beam SEM.

Table of Contents

DEDICATIONS	iii
ACKNOWLEDGEMENT	iv
ABSTRACT	vi
LIST OF TABLES	xii
LIST OF FIGURES	xiii
Nomenclature.....	xvi
CHAPTER 1	1
INTRODUCTION	1
1.1. Lead-acid battery invention, history, and market.....	1
1.2. Purpose of lead-acid battery research	3
1.2.1 Motivation.....	5
1.3 Outline of Thesis.....	7
CHAPTER 2	10
BACKGROUND.....	10
2.1 Electrochemistry of Lead-acid Battery	10
2.1.1 Equilibrium potentials of Pb/PbSO ₄ and PbO ₂ /PbSO ₄ electrodes	12
2.1.2 The Electromotive force.....	13
2.1.3 E/pH diagram of pb/PbSO ₄ /H ₂ O system	15
2.1.4 H ₂ SO ₄ dissociation and PbSO ₄ solubility in H ₂ SO ₄	17
2.1.5 PbSO ₄ nucleation, growth, and particle size.....	19
2.1.6 Secondary reactions.....	20
2.2 Carbon additives in Lead Electrodes.....	24
2.2.1 Role of Carbon in Discharge and Charge Processes.....	24
2.2.2 Graphene in Lead-acid battery electrodes.....	26
2.3 Types of Lead-acid batteries	27

2.3.1 Flooded Lead-Acid Batteries:.....	27
2.3.2 Valve Regulated Battery.....	29
2.3.3 Ultra Battery.....	31
2.3.4 Arc Active Battery.....	33
2.4 Challenges in Lead-acid battery chemistry.....	33
2.4.1 Acid Stratification.....	35
2.4.2 Water Loss and Dry Out.....	36
2.4.3 Electrode sulfation.....	36
2.4.4 Electrode Volume Expansion.....	38
2.4.5 Corrosion of Grid.....	39
2.4.6 Shorting of electrodes.....	39
2.4.7 Gassing.....	40
2.4.8 Thermal runaway.....	41
2.5 Graphene Synthesis techniques.....	42
Chapter 3.....	44
Charge-Discharge Evaluation of Lead-acid battery.....	44
3.1 Charge-Discharge Relationship.....	44
3.1.1 Peukert Law.....	44
3.1.2 Peukert Law for Pb^{2+} Ion Gradient.....	46
3.1.3 Peukert Law: Pb^{2+} and HSO_4^- Ion Gradient.....	50
3.2 Charge Acceptance.....	51
3.2.1 Dynamic Charge Acceptance.....	52
3.2.2 Potential Selection for J_{charge} in KCA.....	53
3.2.3 Correlation between KCA and Lead Sulphate Dissolution Kinetics.....	55
Chapter 4.....	57
Materials and Characterization Techniques.....	57
4.1 Materials for graphene synthesis.....	58

4.1.1 Morphed Graphene	59
4.1.2 Copper surface treatment.....	59
4.2 Graphene Characterization using Raman spectroscopy	60
4.2.1 Graphene Quality Assessment	61
4.2.2 Raman Mapping for Graphene Detection.....	62
4.3 Materials and for Lead-acid electrochemistry	63
4.3.1 Lead Disk Preparation.....	64
4.3.2 Lead Electropolishing Solution	65
4.4 Cyclic Voltammetry	65
4.4.1 Staircase cyclic voltammetry.....	65
4.4.2 Linear cyclic voltammetry	67
4.4.3 Theory of Double Layer Capacitance	68
4.4.4 Discharge and Charge Capacity using I-V curves	70
4.4.5 Electrochemical Thickness of PbSO ₄ layer	70
4.5 Imaging Techniques	71
4.5.1 Atomic Force Microscopy	71
4.5.2 AFM Image Processing.....	73
4.5.3 Focused Ion Beam Scanning Electron Microscopy (FIB-SEM).....	73
Chapter 5	75
Experimental Setups and Procedures	75
5.1. Experimental Setup for Graphene Synthesis	75
5.1.1 Experimental Procedure	76
5.2 Experimental setup of Lead electrode in H ₂ SO ₄	77
5.2.1 Electrochemical cell	77
5.2.2 Experimental Procedure	78
i. Electrochemical Polishing.....	78
ii. Cyclic Voltammetry on Pb surface	79

5.2.3 Sample Preparation for Imaging.....	81
Chapter 6.....	82
Results And Discussion	82
6.1 Characterization of Synthesized Graphene	82
6.1.1 Raman Spectroscopy and Mapping of Graphene on Copper	83
6.1.2 SEM, EDX and HRTEM Imaging of Graphene on Copper	84
6.2 Double Layer Capacitance of Pb Surface	86
6.3 Cyclic Voltammetry Reproducibility	87
6.4 Effect of Potential Scan Rate	89
6.5 Effect of Temperature on Peukert Relationship.....	91
6.5.1 Correlation of Peukert Relationship for Discharge under Galvanostatic and Potentiostatic conditions	91
6.5.2 Variation in Discharge and Charge Capacities with Temperature.....	92
6.5.3 Variation in Peukert Coefficient with Temperature	94
6.6 Kinetic Charge Acceptance Analysis.....	96
6.7 PbSO ₄ Layer Thickness.....	99
6.8 Conductive Area of Discharged Pb Surface	102
CONCLUSION	108
REFERENCES	110

LIST OF TABLES

Table 1. Thermodynamically calculated activities of H ₂ SO ₄ and H ₂ O (19, 20).....	14
Table 2. No. of graphene layers for I _{2D} /I _G ratio at 488 nm and 325 nm laser wavelength. ...	62
Table 3. Peukert Coefficient and Intrinsic Discharge Capacity with Temperature.	95

LIST OF FIGURES

Figure 1. Global market of energy storage (5).	3
Figure 2. Lead electrode surface after 1 st discharge and 1 st charge.....	6
Figure 3. (a) Representation of electrochemical interfaces in lead-acid battery at discharge condition, (b) Secondary processes at lead and lead oxide electrodes during charge	11
Figure 4. (a) Calculated and experimental values of Lead-acid cell EMF with H ₂ SO ₄ concentration (19) (b) Cell voltage and H ₂ SO ₄ concentration changes during one discharge and charge cycle (21).	15
Figure 5. E/pH diagram of pb in H ₂ SO ₄ + H ₂ O with $a_{\text{HSO}_4^-} + a_{\text{SO}_4^{2-}} = 1$ at 25 ⁰ C (23).....	15
Figure 6. Active region in H ₂ SO ₄ concentration for lead-acid battery (37).....	18
Figure 7. Solubility of PbSO ₄ in active region (37).....	19
Figure 8. Crystal nucleation on a surface, γ_1 , γ_2 , and γ_3 are interfacial free energies of surface-crystal, surface-electrolyte, and crystal electrolyte.	20
Figure 9. HER exchange current densities for various metals M-H bond strength (45).....	22
Figure 10. Tafel plot for HER on Pb surface (50).	23
Figure 11. Pb electrochemical reduction on Pb and C surfaces during charge (59).....	25
Figure 12. Standard construction of flooded lead-acid battery (66).	28
Figure 13. Internal oxygen recombination cycle in VRLA battery (72).	30
Figure 14. Electrode arrangement in UltraBattery (79).	32
Figure 15. Schematic of PbSO ₄ crystal size and their solubility (84).	37
Figure 16. Carbon and Copper binary phase diagram (99).	43
Figure 17. Schematic of Agglomerate of Sphere model.	46
Figure 18. Pb ²⁺ solubility vs concentration of H ₂ SO ₄	51
Figure 19. Standard DCA test, (A-B) charge pulse, (B-C) rest period, (C-D) discharge pulse and (D-E) is another rest period (109).	52
Figure 20. Choice of potential for $J_{charge} @E(V)$	55
Figure 21. (a)HRTEM image, (b) bright field image, (c) XRD peak of raw carbon black, (d) Raman spectra vs milling time, (e) HRTEM of 0.5 hr and (f) HRTEM of 2 hr milled carbon black(99).	58
Figure 22. (a) 8 hr annealed, (b) 10 hr annealed Cu sample.....	60

Figure 23. (a) graphite and graphene Raman spectra, (c) width variation of 2D peak for graphite and graphene (112).	61
Figure 24. Schematic representation of Raman mapping (113).....	63
Figure 25. (a) Lead rod (b) punched Pb disk (c) hydraulic press with Pb disk against polished steel surface.	64
Figure 26. (a) Cyclic potential scan. (b) current response of CV.....	66
Figure 27. (a) Current vs time response (not to scale) (b) potential step duration for current measurement for linear (red) and staircase CV (blue).	67
Figure 28. AFM TUNA Schematic.	72
Figure 29. FIB-SEM and Pb sample alignment.....	74
Figure 30. (a) Parts of Cu die. (b, c) Cu substrate and carbon in the die. (d) assembled die.	76
Figure 31. (a) Die press (b) Induction heating setup.	76
Figure 32. Electrochemical Setup.....	77
Figure 33. (a, b) Grain and mirror polished Pb pictures. (c, d) SEM images of same. (e) AFM image of mirror polished Pb surface.	79
Figure 34. (a) DL potential window, (b)DL CV's (c) C_{dl} determination (d) Asymmetric Voltammetry potential scan rate.	80
Figure 35. (a)Raman spectra of graphitic carbon at various temperatures, (b) Shift in Raman spectra, (c) Raman Spectra before and after exfoliation, (d) 2D peak Raman map, (e) I_{2D}/I_G map.	83
Figure 36. (a, b) SEM and EDS images, (c) SEM images of graphene across Cu terraces and FIB-SEM lamella, (d, e) HRTEM images of highly oriented hexagonal graphene on Cu.....	85
Figure 37. Validation of C_{dl} using EIS and CV.	86
Figure 38. (a) Average C_{dl} , (b) C_{dl} vs temperature.	87
Figure 39. Reproducible discharge and charge scans (black) and averaged scan (red) with ... 10 mV/s scan rate at -50°C in 5 M H_2SO_4	88
Figure 40. Wait time required for temperature equilibration between electrolyte and Pb surface.	88
Figure 41. (a, b) Discharge scans, capacity at 22°C and (c) PbSO_4 thickness vs potential scan rate.....	90
Figure 42. SEM images of discharged Pb surface using various discharge scan rates.....	90
Figure 43. Same discharge under potentiostatic and galvanostatic mode.	91

Figure 44. Discharge scans at (a) 1000 mV/s (b) 0.5 mV/s.	93
Figure 45. Charge scans with 1000 mV/s at all temperatures.	93
Figure 46. (a) Peukert relationship (b) Change in Pb^{2+} solubility with temperature.	95
Figure 47. Charge vs peak current fitted to extended Peukert relationship.	96
Figure 48. 10 mV/s charge scans for Pb surface discharged with scan rates from 1000 mV/s to 0.05 mV/s.	97
Figure 49. KCA calculated using charge current (a) peak charge current (KCA_{peak}) and (b) - 1.2 V ($KCA_{@-1.2V}$) plotted against corrected $PbSO_4$ thickness.	98
Figure 50. SEM image of Pb surface discharge with 5 mV/s scan rate at 22 ⁰ C showing (a) top surface of $PbSO_4$ spider (b) Cross-section of <i>Au</i> , $PbSO_4$ and <i>Pb</i> layers.....	100
Figure 51. FIB-SEM cross-section Images of Pb discharged with 5 mV/s at (a) -20 ⁰ C, (b) -50 ⁰ C, (c) 10 ⁰ C, (d) 22 ⁰ C, (e) 40 ⁰ C, (f) 55 ⁰ C.	100
Figure 52. FIB-SEM cross-section Images of Pb discharged with 0.5 mV/s at (a) -20 ⁰ C, (b) -50 ⁰ C, (c) 10 ⁰ C, (d) 22 ⁰ C, (e) 40 ⁰ C, (f) 55 ⁰ C.	101
Figure 53. $PbSO_4$ average thickness measured in Imagej software.	101
Figure 54. Comparison between electrochemical and measured $PbSO_4$ thickness.	102
Figure 55. Height image showing $PbSO_4$ particles on discharge Pb surface at 5 mV/s.	1033
Figure 56. TUNA images of same sample area showing conductive area with pattern of crack on the surface.	1044
Figure 57. Bimodal histogram of TUNA image.	1055
Figure 58. Threshold images of conductive area (a)-20 ⁰ C, (b)10 ⁰ C, (c)22 ⁰ C, (d)40 ⁰ C, (e)55 ⁰ C, (f) Conductive area vs Temperature.	1055
Figure 59. Area between spherical particles in 'Agglomerate of Spheres' model.....	1077

Nomenclature

GWh	Gigawatt hour
PSH	Pumped Storage Hydropower
CAGR	Compound Annual Growth Rate
DOE	Department of Energy
Wh kg ⁻¹	Watt hour per Kilogram
DCA	Dynamic Charge Acceptance
KCA	Kinetic Charge Acceptance
PSoC	Partial State of Charge
PbSO ₄	Lead Sulphate
<i>PbO</i> ₂	Lead dioxide
EMF	Electromotive Force
HER	Hydrogen Evolution Reaction
OER	Oxygen Evolution Reaction
NAM	Negative Active Material
PAM	Positive Active Material
HRPSoC	High-Rate Partial State of Charge
EAC	Electrochemically active carbon
EASA	Electrochemically Active Surface Area
CVD	Chemical Vapor Deposition
EFB	Enhanced Flooded Battery
VRLA	Valve Regulated Lead Acid

HEV	Hybrid Electric Vehicles
PHEV	Plug-in Hybrid Electric Vehicles
EV	Electric Vehicles
PEV	Plug-in Electric vehicles
SLG	Single Layer Graphene
W.E.	Working Electrode
C.E	Counter Electrode
R.E.	Reference Electrode
AFM	Atomic Force Microscopy
FIB-SEM	Focused Ion Beam Scanning Electron Microscopy
SI	Supersaturation Index

CHAPTER 1

INTRODUCTION

1.1. Lead-acid battery invention, history, and market

In today's world, batteries are the key technology for efficient and easy storage of electricity, and it shows high potential for development of various future energy storage technologies for large scale energy storage for electrical grid, vehicle to grid energy system, energy storage in EVs, personalized energy storage for powering homes, etc. Our lives are becoming more and more dependable on batteries as power density, energy density and cycle life of batteries are improving at fast pace and providing power to almost all daily use devices including cell phones, laptops, cars, and even small size homes. Batteries are classified in two broad categories. First, primary batteries such as Zinc-carbon, Zinc chloride battery, alkaline Zinc-Manganese dioxide battery etc., are non-rechargeable because of irreversible electrochemical reaction hence primary batteries are single-use and disposable. Second, secondary batteries such as lead-acid, Nickel-metal hydride, metal-ion, etc. that can be recharged since electrochemical reactions responsible for energy storage are reversible. High energy and power density rechargeable batteries and cell voltage are of most interest for most of the battery application. Development of batteries has its roots in 1800's when voltaic cell and Daniel cell were invented, and electrochemical reactions were used to generate electricity (1). Lead-acid battery invented by French physicist Gaston Planté was the first and the oldest rechargeable battery chemistry and it has been in use for almost more than

160 years. He experimented with electrode materials such as aluminum, gold, tin, lead etc. and observed that electrodes made up of two lead plates immersed in 10% dilute sulfuric acid delivered high voltage and significantly large discharge current for long time. Planté assembled the first practical lead-acid battery from nine parallel connected cells and demonstrated at French Academy of Sciences on 26 March 1860 (2). Ever since it's invention, the lead-acid battery technology has been developing continuously and a variety of configurations are available depending on application requirements. Invention of lead-acid battery pioneered the use of electrical energy stored in a battery for various practical applications such as a lead-acid battery powered electric vehicle designed by Gustave Trouvé in 1881 that reached 12 km h^{-1} , an electric car by Camille Jenatzy in 1899 that held a speed record of 109 km h^{-1} , the first lead-acid battery powered submarine in 1886 and later in telecommunication applications by telephone companies in U.S.A. Nowadays, lead-acid batteries play an essential part in uninterrupted power systems (UPS), starting lightning and ignition (SLI) in gasoline, hybrid and electric vehicles, power grids and backup power for telecommunication systems including 5G, energy storage in industrial setting and many more.

Lead-acid battery technology was responsible for more than 70% of the rechargeable battery market with total production adding up to 600 GWh and a revenue of \$80 billion (3) and the lead-acid battery market worth is predicted to grow up to \$93 billion with CAGR of 5.9% (4) in future as the global demand for energy storage increases as shown in Figure 1 with projections from year 2018 to 2030 in market report from DOE. Lead is cheaper than most active materials used in

batteries and abundantly available in earth crust. It has been the mined and refined for various applications such in lead-acid batteries, lead-tin solders, ammunition, etc. Lead metal recycle technology is well established in developed countries which makes lead-acid battery a very cost-effective way to store energy.

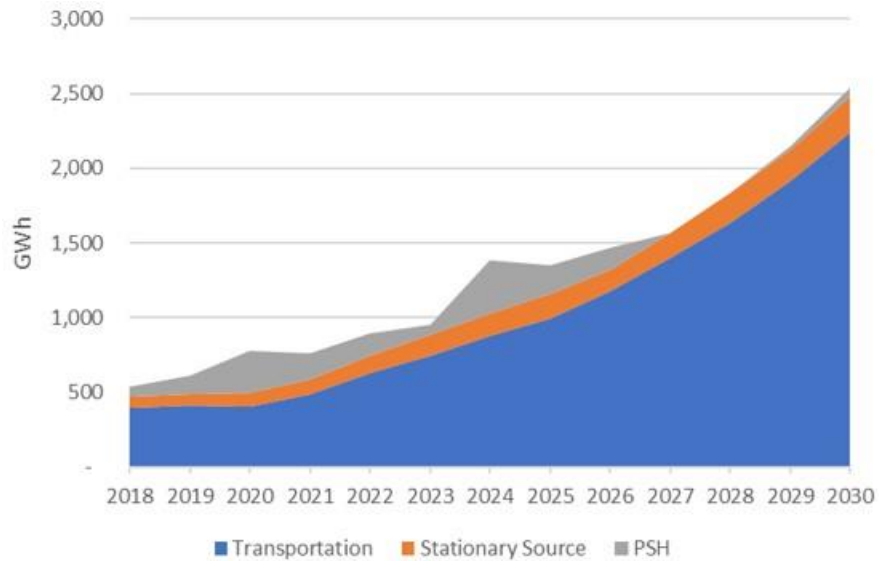


Figure 1. Global market of energy storage (5).

1.2. Purpose of lead-acid battery research

There are many existing battery technologies being used or being investigated by researchers all over the world and lead-acid battery chemistry is one of the most complex systems with wide variety of remaining technological challenges. Lead-acid batteries in use today have practical specific energy density between 30 to 50 Wh kg⁻¹ with a cell voltage of 1.9 to 2.2 V depending on battery type and battery electrode designs (6). The theoretical value of specific energy density is around 167 Wh kg⁻¹ (7). This shows that only 30 to 40% of theoretical energy density can be accessed at present with the lead-acid batteries available in

market, opening a huge opportunity to further improve lead-acid battery system. The lower practical efficiency compared to theoretical is because of the high weight to energy density ratio (8) and a fact that lead-acid batteries are complex electrochemical systems with variety of additives, electrode, and separator materials each having impact on the performance of the battery. Also, the additives such as various types of carbon, lignin expanders, fibers, stabilizers, etc. sometimes have enhancing or counteracting effect on each other within a battery and this gives rise to countless combinations of such materials to be used or tested in a battery. Each manufacturer has their own concoction of battery materials and additives resulting in wide range of battery performance and cost. Therefore, it is essential to try to maximize the efficiency since lead-acid batteries are the cheapest of all rechargeable batteries and can be even more cost effective (9) if main challenges in it can be resolved. Lead-acid batteries can be safely and reliably operated in a wide temperature range from -20° to 50°C without a possibility of catastrophic thermal event causing a fire which is a major concern for lithium-ion. Therefore lead-acid batteries would be beneficial where safety is a priority and battery weight are not of much concern.

Recyclability of spent batteries is a very important factor for keeping cost of the batteries low and reducing environmental pollution caused by them since accumulation of used batteries with low recyclability is slowly becoming an alarming issue. One of the main advantages of lead-acid batteries is almost 99% of all the components are recycled as shown by a recent study conducted on national lead recycling rate in USA (10, 11). The main sources of lead are distinguished as

primary source which is the 85 million tons of lead ore present in the form of lead minerals and the secondary source is the recycled lead from spent batteries. There are green and ecofriendly methods developed for lead recovery and as a result the secondary lead production has exceeded primary lead production in almost all developed countries (12). And there are models proposed by researchers that can be used in developing countries to monitor and recycle all the lead being used for lead-acid batteries (13), although strict government regulation and improved engineering controls are necessary for the success of such plans.

1.2.1 Motivation

Recently, DOE and Consortium for Battery Innovation (CBI) has taken an initiative to develop next generation advanced lead-acid batteries with a technical roadmap (14) to focus research towards solving challenges in lead-acid batteries and getting the cost of energy storage down to \$35/kWh. This study is a part of Lead Battery Science Research Program (LBSRP) funded by >90% of North American lead-acid battery manufacturing industries with help of research facilities at Argonne National Laboratory. The goal of program is an in-depth understanding of fundamentals of lead-acid battery technology and make improvements in DCA, cycle life, PSoC cycling and making lead-acid battery technology for more efficient for sustainable energy storage. It has been predicted that enhanced lead-acid batteries can be used in cost effective long duration energy storage systems and grid energy storage where cost is the key driving factor. The focus of this study is on negative lead electrode in lead-acid battery to understand the effect of temperature, concentration and impurities during discharge and charge. Morphology, thickness,

and size of $PbSO_4$ is related to discharging and charging of electrodes and it is important to understand morphological changes happening at the electrode surface to push the performance of lead-acid battery. This work includes morphological investigation of $PbSO_4$ layer developed after electrochemically discharging Pb electrode at different rates in potentiostatic mode. Imaging techniques such as FIB-SEM for $PbSO_4$ layer thickness measurement by cross-sectional imaging and conductive AFM for measuring conductive area of discharged Pb surface. The baseline performance established in this work can be used to quantify the effect of additives and various designs of negative Pb electrode. The understanding the evolution of electrode surface area in flat lead electrode in excess electrolyte during discharge-charge cycling can be helpful in designing experiments to explore surface area and porosity in more complex electrode structures. The changes in lead electrode morphology after 1st discharge and 1st charge are shown in Figure 2 which indicates that it is important to understand the changes in electrode during cycling.

A part of research in this thesis includes proof of concept of completely solid-state synthesis graphene layers on metallic surface which can be implemented to introduce graphene in battery electrodes since graphitic carbon has shown to improve charging process in lead-acid batteries.

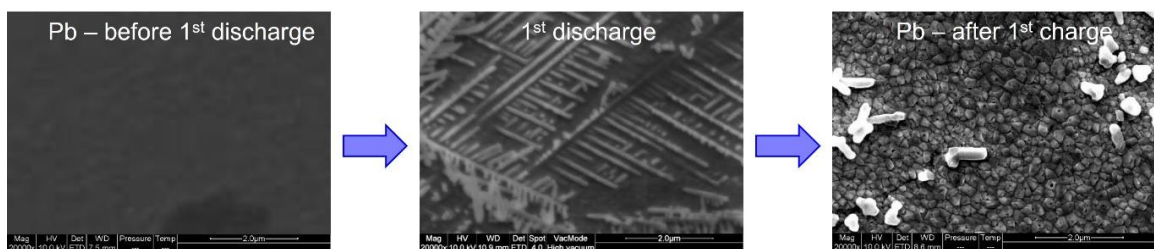


Figure 2. Lead electrode surface after 1st discharge and 1st charge.

1.3 Outline of Thesis

The thesis dissertation consists of 6 Chapters organized as:

Chapter 1 starts with an introduction and history of Lead-acid battery connecting the reader to historic importance of the battery, applications of lead-acid batteries and some market trends related to the growth of the lead-acid battery market. Later in Chapter 1 the purpose of research on lead-acid battery science is explained that shows room for development and some key advantages of lead-acid battery technology over other batteries which are beneficial for sustainability. The importance of looking at lead-acid chemistry with newly developed characterization and imaging methods would be helpful to develop an improved lead-acid battery. This chapter also mentions a graphene synthesis methods developed completely in solid state which shows potential application in battery research to introduce graphene in the electrodes.

Chapter 2 explains the electrochemical fundamentals for lead-acid battery discovered at the time of invention and fundamental understanding developed over year of research. This chapter explain equilibrium potentials of lead electrodes, EMF generated by battery, E-pH diagram of $Pb/PbSO_4$ and $PbO_2/PbSO_4$ interface explaining potential pH dependance of various reactions in $Pb/H_2SO_4/H_2O$ system. Role of H_2SO_4 dissociation in reactions proceeding in lead-acid batteries and concentration of ions at various concentrations of sulfuric acid and its effect on $PbSO_4$ solubility is also discussed. Further in the chapter, carbon additives, types of

lead-acid batteries, challenges and problems in lead-acid battery chemistry are mentioned which needs to be resolved so the performance can be boosted.

Chapter 3 includes theoretical aspects of Peukert relationship used for estimation of remaining charge in the lead-acid battery during its use. A standard DCA test is explained with reasons to improve charge acceptance of lead-acid battery. A method of using asymmetric CV to study kinetic charge acceptance of the electrode is developed and explained which is necessary for interpretation of results. Since established relationship are not perfect, a derivation of Peukert and KCA equations from combination agglomerate of sphere theory, normal distribution for $PbSO_4$ nucleation and electrochemical laws is included which can relate $PbSO_4$ particle size and thickness to Peukert relationship and KCA. The derived laws are used in chapter 6 for result analysis.

Chapter 4 explains the materials used for experiments and pre-experimental treatment of materials. It also includes characterization and imaging methods used in the experimental study. Raman mapping, SEM, HRTEM is used for graphene detection on copper therefore, the Raman spectra peak intensity criteria for graphene quality assessment are explained. And for Pb, CV waveforms used for C_{dl} and discharge-charge of Pb surface and its data analysis are explained. Later in the chapter, AFM-TUNA for conductive imaging and FIB-SEM for cross-sectional imaging is explained since the images from these techniques are included in the results.

Chapter 5 lists the experimental procedures used for the experimental setups. The setup of copper die inside induction furnace used for graphene synthesis is shown. The 3-electrode electrochemical cell for Pb electrochemical testing and samples preparation developed for imaging is explained at the end of this chapter.

Chapter 6 contains results both graphene and Pb studies. First the results of confirmation of graphene produced in solid state is discussed. Secondly, C_{dl} used as metric for electropolished Pb surface area and its variation with temperature is observed. A special effort was made to achieve highly reproducible and reliable CV data from Pb electrochemistry is shown. Data reliability is important for observing definite trends of Peukert and KCA analysis. And finally, imaging reveals variation in thickness and particle size with variation in discharge process of Pb electrode. AFM TUNA images of Pb samples discharged at all six temperatures are shown with conductive area calculated from the images. The image processing and analysis is included to extract information from images.

CHAPTER 2

BACKGROUND

2.1 Electrochemistry of Lead-acid Battery

Lead acid battery has been continuously developed over the past century, but the basic operation has not changed in last 160 years since it was invented. A typical simple lead-acid cell consists of a negative lead electrode, a positive lead oxide electrode and a separator immersed in a sulfuric acid electrolyte from which a high electromotive force is obtained. There are two solid-liquid electrochemical interfaces at play in lead-acid cell at discharged condition as shown in the Figure 3a schematic. First interface being lead and H_2SO_4 , second one of lead oxide and H_2SO_4 . During discharge, the lead electrode undergoes oxidation or dissolution reaction producing Pb^{2+} ions and $2e^-$. The Pb^{2+} ions react with SO_4^{2-} ions to precipitate $PbSO_4$ on the surface of lead electrode. And the lead oxide electrode undergoes reduction by taking $2e^-$ and forming Pb^{2+} ions at the interface which reacts with SO_4^{2-} in the electrolyte to form $PbSO_4$ (15). The $2e^-$ released at negative electrode flows to the positive electrode via external circuit. Therefore, at completely discharged state both lead and lead oxide electrodes are covered with non-conductive $PbSO_4$ passivation layer and are usually represented as $Pb/PbSO_4$ and $PbO_2/PbSO_4$ electrodes. During charging, the $PbSO_4$ formed at both electrodes undergoes chemical dissolution to produce Pb^{2+} and SO_4^{2-} ions. At negative electrode the Pb^{2+} ions are electrodeposited back on the lead electrode as *Pb* metal

and at positive Pb^{2+} ions are oxidized to Pb^{4+} which react with H_2O to form PbO_2 at positive electrode (14) as indicated in Figure 3b. The HSO_4^- ion from H_2SO_4 dissociation process is responsible for the $PbSO_4$ formation on lead-acid battery electrodes since it reacts with Pb^{2+} ions and releases H^+ ions. Further details of acid dissociation are discussed in section 2.1.4. An external current must be provided during charging so that the e^- flow is reversed, and the electrodes can be recovered. The overall reaction of discharging and charging reactions in the lead-acid cell (15) is given as

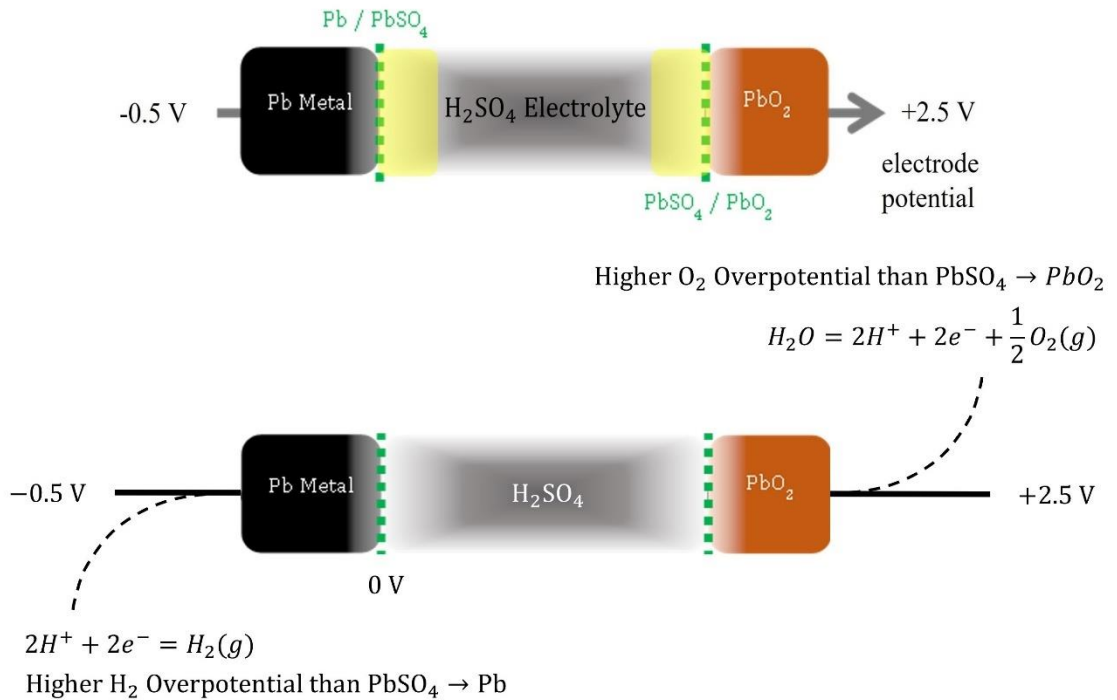
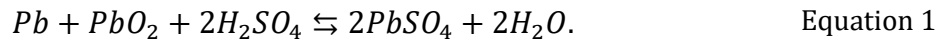


Figure 3. (a) Representation of electrochemical interfaces in lead-acid battery at discharge condition, (b) Secondary processes at lead and lead oxide electrodes during charge.

2.1.1 Equilibrium potentials of Pb/PbSO_4 and $\text{PbO}_2/\text{PbSO}_4$ electrodes

The discharge and charge electrochemical reaction occurring at negative electrode is represented as



From the electrochemical thermodynamic principles, the standard electrode potential vs S.H.E of Pb/PbSO_4 electrode, $E_{\text{Pb}/\text{PbSO}_4}^0$ can be determined from the Gibbs free energy (16) of reactants and products of reaction in Equation 3 as

$$E_{\text{Pb}/\text{PbSO}_4}^0 = \frac{\Delta G^0}{nF}, \quad \text{Equation 3}$$

where n is number of electrons involved in the reaction and F ($C \text{ mol}^{-1}$) is Faraday constant.

The ΔG^0 is negative for reduction and positive for oxidation and from combination of Equation 2 and 3, the $E_{\text{Pb}/\text{PbSO}_4}^0$ can be obtained as

$$E_{\text{Pb}/\text{PbSO}_4}^0 = \frac{-\Delta G_{\text{PbSO}_4}^0 - (\Delta G_{\text{SO}_4^{2-}}^0 + \Delta G_{\text{Pb}}^0)}{nF}. \quad \text{Equation 4}$$

After substituting values of free energies from (16) the $E_{\text{Pb}/\text{PbSO}_4}^0$ becomes,

$$E_{\text{Pb}/\text{PbSO}_4}^0 = -0.358 \text{ (V)}. \quad \text{Equation 5}$$

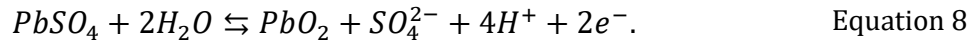
Now using Nernst equation (17), the equation for equilibrium potential of Pb/PbSO_4 electrode, $E_{\text{Pb}/\text{PbSO}_4}$ can be given as

$$E_{\text{Pb}/\text{PbSO}_4} = E_{\text{Pb}/\text{PbSO}_4}^0 + \left(\frac{RT}{nF}\right) \ln k, \quad \text{Equation 6}$$

where $k = a_{PbSO_4}/(a_{Pb} \times a_{SO_4}^{2-})$ is equilibrium constant which is the ratio of activities of reaction products, T is temperature in Kelvin (K), $R = 8.314 (J K^{-1} mol^{-1})$ which is universal gas constant and $n = 2$ in Equation 2. Then Equation 6 becomes

$$E_{Pb/PbSO_4} = -0.358 - 0.029 \times \log(a_{SO_4^{2-}}) \quad (V). \quad \text{Equation 7}$$

Similarly, the reaction at positive electrode during discharge and charge is give as



The standard electrode potential for $PbO_2/PbSO_4$ electrode, $E_{PbO_2/PbSO_4}^0 = 1.683 (V)$ can be calculated using Gibb's free energies as

$$E_{PbO_2/PbSO_4}^0 = \frac{-\Delta G_{PbO_2}^0 - \Delta G_{SO_4^{2-}}^0 - 4\Delta G_{H^+}^0 + \Delta G_{PbSO_4}^0 + 2\Delta G_{H_2O}^0}{2 \times 96500}. \quad \text{Equation 9}$$

And again, using Nernst equation the equilibrium potential of $PbO_2/PbSO_4$ electrode can be obtained as

$$E_{PbO_2/PbSO_4} = 1.683 - 0.118 \times pH - 0.059 \lg(a_{H_2O}) + 0.029 \lg(a_{SO_4^{2-}}), \quad \text{Equation 10}$$

where, activity of H_2O is 1.

2.1.2 The Electromotive force

The EMF, ΔE generated by the lead-acid cell is result of difference between high positive equilibrium potential of $PbO_2/PbSO_4$ electrode as shown in Equation 10 and high negative equilibrium potential of $Pb/PbSO_4$ electrode as shown in Equation 7 in reference to hydrogen electrode equilibrium potential (18) given as

$$\Delta E = 2.041 - 0.118 \times pH - 0.059 \times \lg a_{SO_4^{2-}} - 0.059 \lg a_{H_2O}. \quad \text{Equation 11}$$

As seen in Equation 11, the EMF of lead-acid cell depends on the SO_4^{2-} and H_2O activities. When the lead-acid battery electrodes are discharged and $PbSO_4$ is formed, the concentration of H_2SO_4 is decreased causing significant increase in pH of the electrolyte. The activity of SO_4^{2-} and H_2O changes with the H_2SO_4 concentration that causes a drop in the EMF of lead-acid cell (20). Table 1 lists the H_2SO_4 and H_2O activities with acid concentration. Figure 4a shows the calculated and experimentally observed EMF with H_2SO_4 molality. And Figure 4b shows drop in cell voltage and H_2SO_4 concentration during constant current discharge and increase in both as the cell is charged at constant current (21).

Table 1. Thermodynamically calculated activities of H_2SO_4 and H_2O (19, 20).

Concentration		γ	a_{H_2O} (against molality)	$a_{H_2SO_4}$ (against molality)	EMF (ΔE), V
mol kg ⁻¹	mol L ⁻¹				
0.5	0.49	0.144	0.9819	0.00148	1.881
0.7	0.68	0.131	0.9743	0.00307	1.900
1	0.96	0.121	0.9618	0.00716	1.922
1.5	1.42	0.117	0.9387	0.0214	1.951
2	1.86	0.118	0.9126	0.0522	1.975
2.5	2.28	0.123	0.8836	0.1158	1.996
3	2.69	0.131	0.8516	0.2440	2.016
3.5	3.08	0.143	0.8166	0.4989	2.035
4	3.46	0.157	0.7799	0.9883	2.054
4.5	3.82	0.173	0.7422	1.888	2.072
5	4.17	0.192	0.7032	3.541	2.090
5.5	4.50	0.213	0.6643	6.463	2.106
6	4.83	0.237	0.6259	11.48	2.123
6.5	5.14	0.263	0.5879	20.02	2.139
7	5.44	0.292	0.5509	34.21	2.154

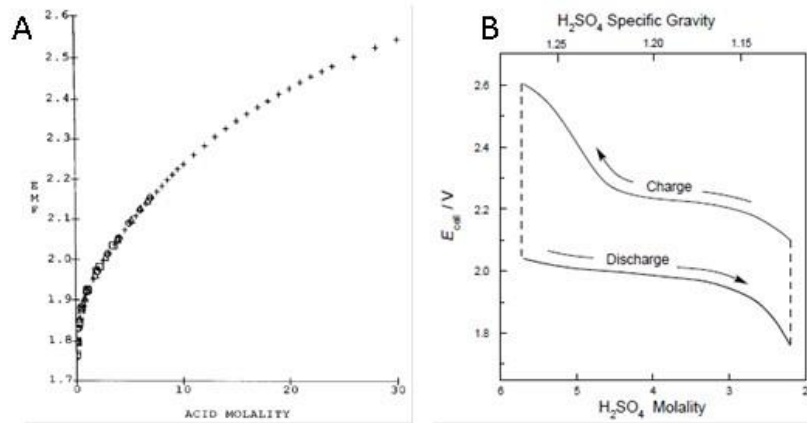


Figure 4. (a) Calculated and experimental values of Lead-acid cell EMF with H_2SO_4 concentration (19) (b) Cell voltage and H_2SO_4 concentration changes during one discharge and charge cycle (21).

2.1.3 E/pH diagram of pb/PbSO₄/H₂O system

Since EMF and most of the reactions during operation of lead-acid cell are highly influenced by electrolyte pH, an E/pH diagram of lead in dilute H_2SO_4 can give operating limits of potential and pH with valuable information about secondary reactions such as HER and OER (23).

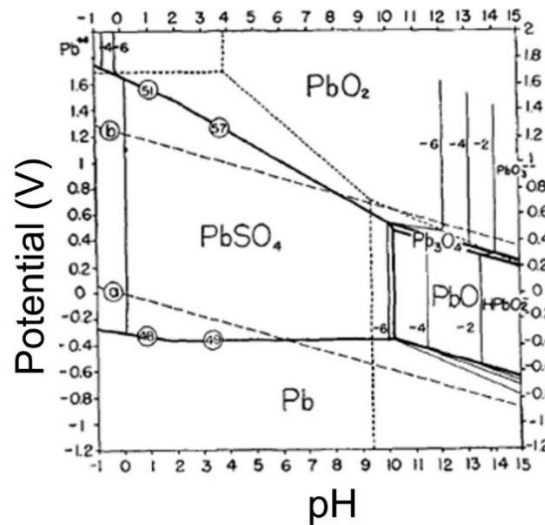


Figure 5. E/pH diagram of pb in $H_2SO_4 + H_2O$ with $a_{HSO_4^-} + a_{SO_4^{2-}} = 1$ at $25^\circ C$ (23).

The E/pH diagram in Figure 5 shows the stability region of Pb, PbSO₄ and PbO₂ represented by solid lines. The reactions with lines parallel to x-axis are independent of pH and parallel to y-axis are independent of potential and the equilibrium line with slope depends on pH and potential. The reactions and their corresponding equilibrium potential equations are used to construct the E/pH diagram (24, 25) . The Pb and PbSO₄ are in equilibrium between pH 3 and 10. The stability region from Pb/ PbSO₄ to PbO₂/ PbSO₄ equilibrium shows the EMF of the cell on potential axis. An increase in pH beyond 10 starts forming PbO or Pb(OH)₂. The dashed line in negative potential region shows the equilibrium potential of hydrogen electrode, H^+/H_2 and dashed line in positive potential region show equilibrium potential of oxygen electrode, H_2O/O_2 . The H^+/H_2 equilibrium line starts at positive potential than Pb/ PbSO₄ equilibrium suggesting hydrogen evolution takes place before $PbSO_4$ formation. The E/pH diagram of pb/PbSO₄/H₂O system shows that water splitting reactions are thermodynamically more favorable and Lead-acid system is thermodynamically unstable and should never work. But in practice the opposite happens, this is because Pb has high over potential for hydrogen evolution shown in Figure 3b at high negative potentials on a potential scale. Similarly, the H_2O/O_2 equilibrium starts before PbO₂/ PbSO₄ suggesting oxygen evolution before sulfation of PbO_2 . But PbO_2 has high overpotential for oxygen evolution as seen in Figure 3b at high positive potentials on a potential scale. Therefore E/pH diagram can predict most likely reactions lead-acid cell depending on pH and potential conditions.

2.1.4 H_2SO_4 dissociation and $PbSO_4$ solubility in H_2SO_4

The dissociation of H_2SO_4 has been studied theoretically and experimentally to determine the ionic species produced and dissociation constants (26, 27). It has been established that the dissociation of H_2SO_4 is a two-step process involving fractions of HSO_4^- , H^+ or H_3O^+ and SO_4^{2-} ions that have been detected by photoelectron and Raman spectral fingerprints (28, 29). The first degree of dissociation of H_2SO_4 gives H^+ and HSO_4^- ions as given by



And the dissociation constants for first degree of dissociation k_1 , and second degree of dissociation k_2 , are determined by the ratio of activities of products to activity of reactants in Equation 12 and Equation 14 respectively. k_1 can be expressed as

$$k_1 = \frac{a_{H^+} \times a_{HSO_4^-}}{a_{H_2SO_4}} \quad \text{Equation 13}$$

The second degree of dissociation of H_2SO_4 gives H^+ and SO_4^{2-} ions from HSO_4^- ions as given by



The k_2 for equation 13 can be expressed as

$$k_2 = \frac{a_{H^+} \times a_{SO_4^{2-}}}{a_{HSO_4^-}} \quad \text{Equation 15}$$

The values of k_1 (27, 30) and k_2 (31, 32, 33) have been calculated by various methods in several literature. The concentration of dissociated HSO_4^- and SO_4^{2-} ions vary with concentration of H_2SO_4 as shown in Figure 6. Since lead-acid battery processes involve HSO_4^- ions, the concentration of H_2SO_4 in lead-acid cell must be

chosen so that the HSO_4^- ion concentration is high. Figure 6 shows the acid concentration range in the active region. The discharge and charge process of lead-acid battery also depends on solubility of $PbSO_4$ in H_2SO_4 . The $PbSO_4$ has very low solubility in H_2SO_4 and it varies depending on concentration and temperature of H_2SO_4 . The solubility is highest in 0.5 M H_2SO_4 at 6.5 mg/l with decreasing trend as acid concentration increases to 5 M in which it is 1.8 mg/l as reported by Vinal et al. (34) and Crockford et al. (35). The lower solubility of $PbSO_4$ between 0.5 M to 5 M H_2SO_4 concentration is responsible for passivation of electrodes and probably related to reversibility of electrode reaction as the lead-acid battery is charged. It was observed by Danel et al. (34) and Vinal et al. (36) that $PbSO_4$ solubility is higher in the active region of H_2SO_4 concentration as shown in Figure 7. This is the reason for using 0.5 M to 5 M H_2SO_4 concentration range for lead-acid battery.

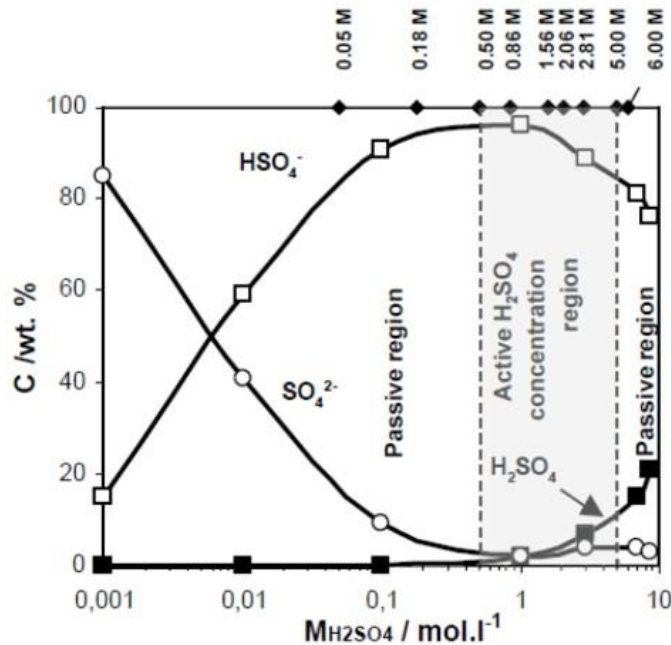


Figure 6. Active region in H_2SO_4 concentration for lead-acid battery (37).

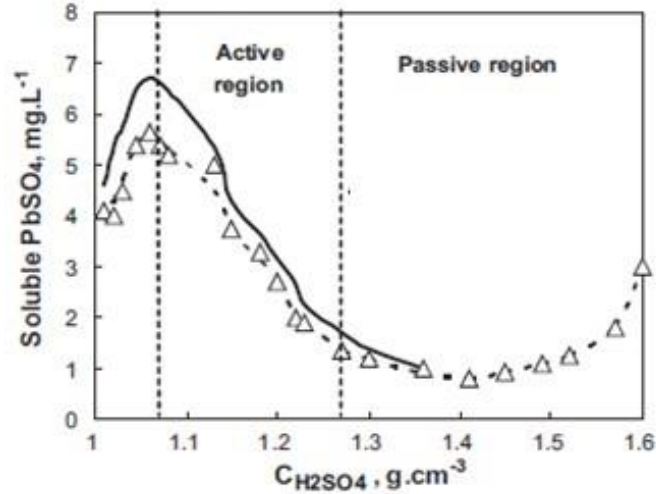


Figure 7. Solubility of $PbSO_4$ in active region (37).

2.1.5 $PbSO_4$ nucleation, growth, and particle size

Lead sulphate formation is a chemical process occurring on the Pb surface therefore, nucleation of $PbSO_4$ is a primary heterogeneous nucleation process (38, 39). Formation of crystals includes two steps, namely nucleation and growth and it occurs when the solution is saturated with ions forming the crystal (40). According to classical nucleation theory (41), crystal nucleation takes place when the nucleation barrier defined by free energy of nucleation is surpassed at saturated conditions. Therefore, nucleation depends on the supersaturation index, $SI = C_{M^+}/[C_{M^+}]$ which is a ratio of concentration of ions in bulk to solubility of ions involved in crystal formation. And a nucleation rate dependent on SI can be given as

$$Nucleation\ rate = A * (SI) \exp\left(-\frac{B}{\ln^2(SI)}\right). \quad \text{Equation 16}$$

A and B in equation 16 are constants. Higher nucleation rate results in a greater number of nuclei therefore, number of nuclei is also related to SI. The nucleated

crystals grow during crystal growth and the electrolyte saturation decreases. Assuming spherical shape of crystals, a critical nucleus size is related to supersaturation and interfacial energies from surface, crystal, and electrolyte interfaces (42) as shown in Figure 8.

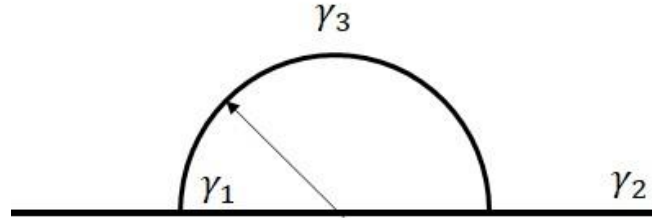


Figure 8. Crystal nucleation on a surface, γ_1 , γ_2 and γ_3 are interfacial free energies of surface-crystal, surface-electrolyte, and crystal electrolyte.

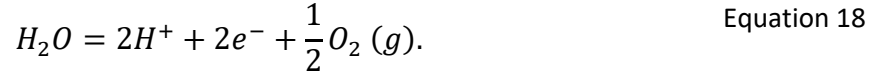
Crystal growth models proposed over the years suggest that shape of crystal is because of crystal growth along specific crystallographic facet (43). It is also observed that crystallographic orientation of Pb surface influences $PbSO_4$ crystal orientation and the dendritic growth of $PbSO_4$ is dependent on the discharge conditions (44).

2.1.6 Secondary reactions

The HER and OER are the main secondary reactions occurring at the negative and positive electrode respectively in lead acid battery and these reactions cause issues such as water loss and corrosion of Pb and PbO_2 electrodes. During charging of lead-acid battery electrodes, e^- provided from external power source starts reducing H^+ ions at pb electrode after $PbSO_4$ is reduced back to Pb and H_2 gas is evolved by reaction given as



And at PbO_2 electrode, O_2 reduction starts after $PbSO_4$ oxidation to PbO_2 is completed and O_2 is evolved by reaction given as



Therefore, water electrolysis occurs as H_2 and O_2 are evolved. The equilibrium potentials are given by Nernst equation for H^+/H_2 as

$$E_{H^+/H_2}^0 = -0.059 \times pH - 0.029 \times \log(P_{H_2}). \quad \text{Equation 19}$$

And for H_2O/O_2 reactions as

$$E_{H_2O/O_2}^0 = 1.228 - 0.059 \times pH - 0.029 \log(a_{H_2O}) + 0.015 \log(P_{O_2}). \quad \text{Equation 20}$$

During charging, the negative electrode is polarized to more negative potentials than E_{H^+/H_2}^0 then the difference in these potentials is the 'Hydrogen Overpotential' and positive electrode is polarized to more positive potentials than E_{H_2O/O_2}^0 then the difference is the 'Oxygen Overpotential'. When potential of negative and positive electrode reaches H_2 and O_2 overpotential, gassing occurs at the electrodes. Gassing of electrodes increases the concentration of acid due to water loss and shifts the concentration in passive region shown in Figure 7 which results in loss of battery capacity, cycle life and reversibility of electrodes in a battery.

Hydrogen evolution is very sensitive to purity of Pb electrode. Pb metal usually contain trace amounts of impurities such as Ag, Bi, Sn, In, Tl, As, etc. since the

traces of these elements are difficult and expensive to separate from Pb metal. Ag, Bi, Sn of these impurities are more prone to evolve H_2 owing to their higher H_2 overpotential compared to Pb while Tl, Sn, In show lower H_2 evolution than Pb. Figure 9 shows the comparison of exchange currents for H_2 evolution of these elements (45). Therefore, purity and composition of Pb alloys for electrode is important for reducing H_2 evolution.

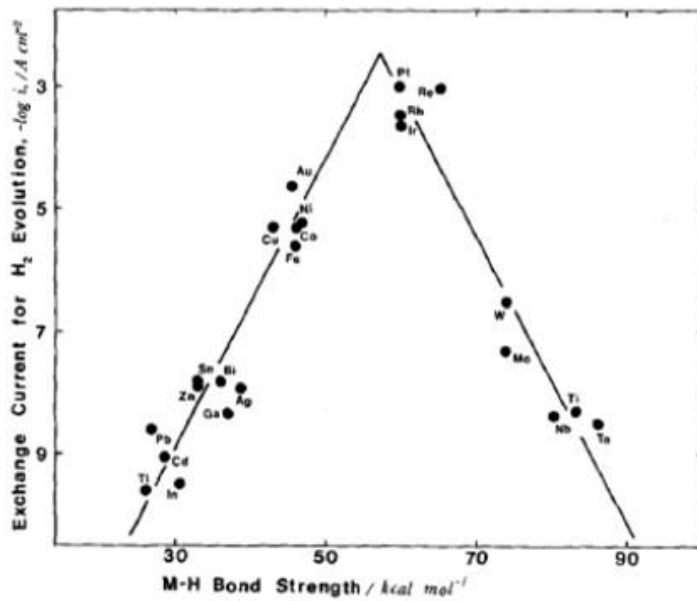


Figure 9. HER exchange current densities for various metals M-H bond strength (45).

The polarization curves of H_2 evolution reaction obtained at high overpotential, η , is related to current response by Tafel equation given as

$$\eta = a + b \times \log(j), \quad \text{Equation 21}$$

where a is constant, b is Tafel slope and j is current or current density. The slope of Tafel plot is used to compare the H_2 evolution reaction on various electrodes (46). Figure 10 shows the Tafel plot for the HER on Pb. The H_2 evolution of additive such

as carbon (47) and H_2 evolution inhibitors (40, 41) in Pb NAM have been studied and found to be useful in increasing the H_2 overpotential. Linear sweep voltammetry is also effective method to study HER at high negative potentials.

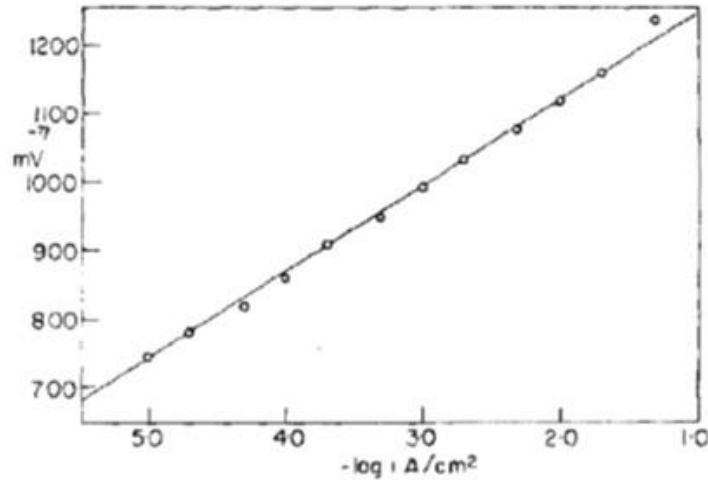


Figure 10. Tafel plot for HER on Pb surface (50).

H_2 and O_2 evolution at the electrodes are the supporting reactions for the self-discharge of NAM and PAM of lead-acid battery (18). At open circuit, a small steady state current between H_2/H^+ and $Pb/PbSO_4$ electrode passes that reduces O_2 and evolves small amount of H_2 causes $PbSO_4$ formation on Pb electrode and small current evolve O_2 and forms $PbSO_4$ at PbO_2 electrode. This causes loss of active materials and capacity of the lead-acid battery. Since H_2 and O_2 overpotentials are very high at Pb and PbO_2 electrode, the self-discharge of lead-acid battery is very slow but becomes significant during long storage time.

2.2 Carbon additives in Lead Electrodes

Carbon in its various forms had shown to be useful in lead-acid battery performance. Amorphous carbons such as activated carbon (51), carbon black (52), and crystalline carbon such as graphite, graphene nano-sheets (45, 46), nanofibers (52), graphene oxide etc. have been investigated for its effect on both positive and negative electrodes of a lead-acid battery (53). Low dynamic charge acceptance is one the limitation that makes lead-acid battery unfavorable to use in EVs and where the battery is operated under High-Rate Partial State of Charge (HRPSoC) (54). Both graphitic carbon and amorphous carbon additives has been shown to improve charge acceptance, specific capacity (55) and cycle life of lead-acid battery operated under HRPSoC condition (56). Carbon type, particle size, porosity, conductivity shows high influence on battery cycle life (49). There exist several hypotheses with experimental evidence for improved performance of lead-acid battery after addition of carbon.

2.2.1 Role of Carbon in Discharge and Charge Processes

Shiomi and Nakamura et al. proposed that carbon forms a conductive network in lead electrodes during cycling which aids $PbSO_4$ reduction to Pb and reduces formation of irreversible $PbSO_4$ formation also known as sulfation of negative electrode in valve regulated lead-acid battery (52, 53). It has also been suggested that carbon provides steric hindrance to $PbSO_4$ crystallization and limits $PbSO_4$ particle growth results in small and easy to dissolve $PbSO_4$ crystal particles. Surface area of carbon is electrochemically active because of its conductive nature. High

surface area of porous carbon particles in micrometer size range is also believed to be beneficial for charging of lead electrode by providing more Electrochemically Active Carbon (EAC) sites for lead deposition as suggested by Pavlov et al (59). They also put forward a parallel mechanism for charging of Pb electrodes when Pb^{2+} is electrodeposited on Pb+C electrode, it is deposited on both Pb, and C surface simultaneously as shown in Figure 11.

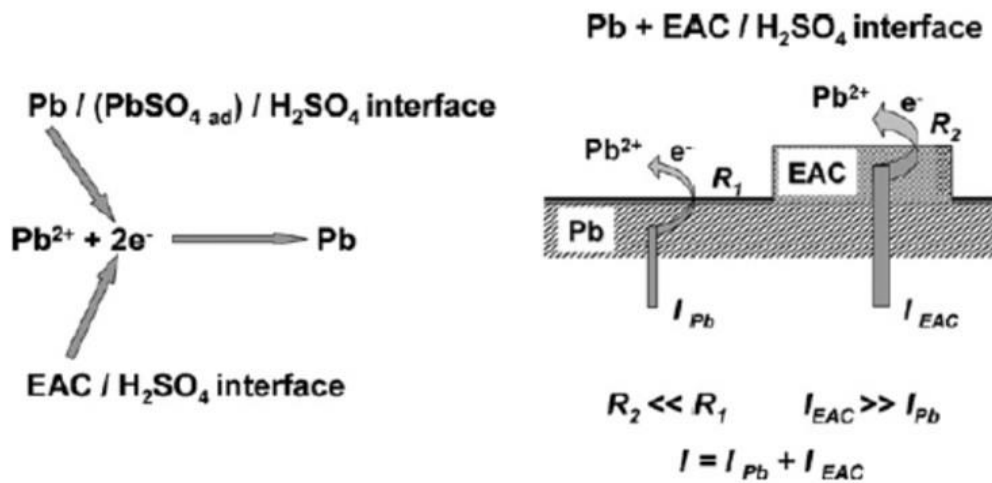


Figure 11. Pb electrochemical reduction on Pb and C surfaces during charge (59).

The surface at which electrochemical reaction occurs is known as Electrochemically Active Surface Area (EASA). The increase in EASA due to addition of EAC reduces charge current density and polarization of Pb electrode since Pb^{2+} reduction on C has lower resistance. Carbon surfaces tested in electrochemical systems usually show higher capacitive currents mostly due to very high surface area and has enhancing effect on double layer capacitance of NAM. Graphene based carbon additives with high specific capacitance are very effective in lead-acid

battery electrodes at HRPSoC. Therefore, the super capacitive effect of EAC and graphitic carbons (60) has shown significant improvement in charge acceptance and discharge power (61). Both capacitive and faradaic contributions are responsible for charge acceptance. Although carbon additives are beneficial for lead-acid battery electrodes, the hydrogen overpotential of carbon is lower than Pb. Addition of carbon increases H_2 evolution at negative Pb electrode therefore, the amount and purity of carbon additives are important to keep H_2 evolution to the minimum to avoid water loss. Since graphitic carbons such as nanosheets, nanofibers, graphite has shown improvements in Pb electrode performance, in this work, a simple, low-cost method for graphene synthesis on transition metals is developed which can be used to introduce graphitic carbon in battery electrodes.

2.2.2 Graphene in Lead-acid battery electrodes

Variety of graphene including doped graphene, graphene oxide (GO), graphene nanotubes have proved to be useful in processes occurring at battery electrodes. Lead-acid battery is also benefited from addition of graphene in the electrodes. Graphene is usually prepared using CVD or reduction of GO and the methods for introducing graphene in electrodes of lead-acid battery vary depending on the type of electrodes.

For lead plate electrodes, generally 2 wt.% graphene additives in the form of powder are mixed with molten lead metal at around 750°C in presence of alkali chloride or fluoride. The mixture is cooled and solidified and the salts are

washed away, and a lead-graphene composite is obtained which is used as battery electrode (62).

Paste electrodes used in lead-acid batteries are made from a negative active material in the form of powders and 0-25 wt.% graphene additives are added to the mix. The mixture is then subjected to high energy ball milling to disperse graphene evenly in the composite mixture. Sulphuric acid and water are added to convert composite mixture from powder to paste form. And the paste electrodes then undergo heating and curing procedure for mechanical rigidity prior to using them in the battery (63–65).

2.3 Types of Lead-acid batteries

Over last century, many variations of lead-acid battery have been developed as per the need for various applications. The performance of lead-acid battery depends on battery type, design, working, and materials used. The main type of batteries in use and newly developed advanced Lead-acid batteries are listed below with details about how they work, difference between their performance and their applications.

2.3.1 Flooded Lead-Acid Batteries:

Flooded lead-acid batteries are also known as vented batteries since H_2SO_4 is present in excess and *Pb* and *PbO₂* electrodes in the form of plates are immersed in it. The positive and negative plates are stacked alternatively and separated by porous separator made from plastic materials to electrically isolate positive and negative electrode (66). A standard 12 V commercial flooded lead-acid battery

design is shown in Figure 12. Flooded battery is equipped with a vent to let out gases produce in stoichiometric ratios from secondary reaction in the battery as discussed in section 2.1.5. This is the reason flooded batteries must be mounted upright to avoid electrolyte leakage. These batteries have the lowest cost per kWh cycle and are long-lasting batteries at their performance level. These batteries are used in automobiles for starting, lighting and ignition purposes. They are also good for deep cycling and are used for energy storage in solar systems for same reason. The common reasons for failure of flooded batteries include water loss, acid stratification, low DCA, lower specific capacity and positive plate expansion and negative plate corrosion (67). These batteries require regular maintenance of water addition due to high gassing rates and regular inspection maintain proper functioning of the battery.

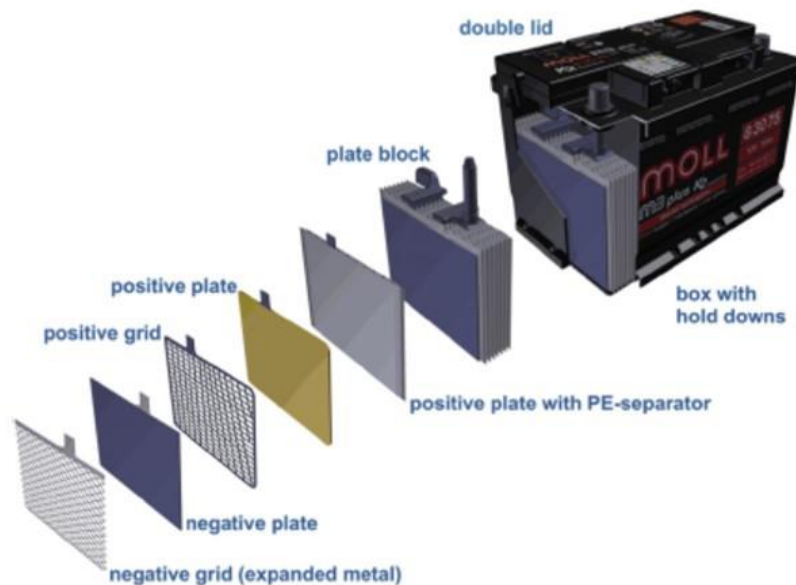


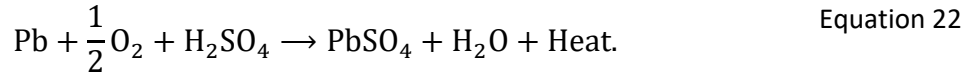
Figure 12. Standard construction of flooded lead-acid battery (66).

Modification applied to the design and materials of flooded battery to mitigate the shortcomings have resulted in 'Enhanced Flooded Battery' (EFB). These batteries use modifications such as pasted electrodes, reinforcement material in positive electrode to reduce active mass shedding, carbon additive to negative electrode, improved plate designs, mechanical equipment for maintaining same acid concentration in battery (15). EFBs have shown better deep cycling, DCA, longer cycle life performance (68) compared to conventional flooded lead-acid batteries at about 20% to 40% increase in cost.

2.3.2 Valve Regulated Battery

Valve regulated batteries are sealed batteries that are made from similar electrode but the H_2SO_4 solution immobilized in the cell. This is done by either gelling the acid solution (69) or by using absorptive glass mat. A fine silicon powder is mixed with acid to form a gel like consistency that is used as electrolyte between positive and negative electrodes along with a separator. Second type of VRLA battery is made using AGM (70) made of highly absorptive glass fibers between the electrodes. H_2SO_4 is injected into AGM to be absorbed. Plate spacing in AGM type is important and must be enough for optimal absorption and to hold required amount of H_2SO_4 (71). There is no need of a separator in AGM batteries since AGM itself acts as a separator and acid reservoir. During charging or overcharging of VRLA battery, O_2 produced at positive electrode transfers to negative electrode through pockets in gel electrolyte and spaces between glass mat fibers for gel and AGM type batteries respectively as shown in Figure 13. The transferred O_2 undergoes recombination

reaction to produce water. This phenomenon is named as ‘internal oxygen recombination cycle’ (72) as shown below



This recombination reaction reduces H_2 evolution at negative Pb electrode by shifting its potential in positive direction. Therefore, gassing in VRLA battery is extremely low if proper charging protocol is used which make sealing VRLA possible and there is no need of maintenance during lifespan of the battery. An empty space is left at the top of VRLA battery to accommodate the small quantity of gases released during battery operation. VRLA battery always contains a one-way release valve to regulate the pressure created by gases over cycling (70).

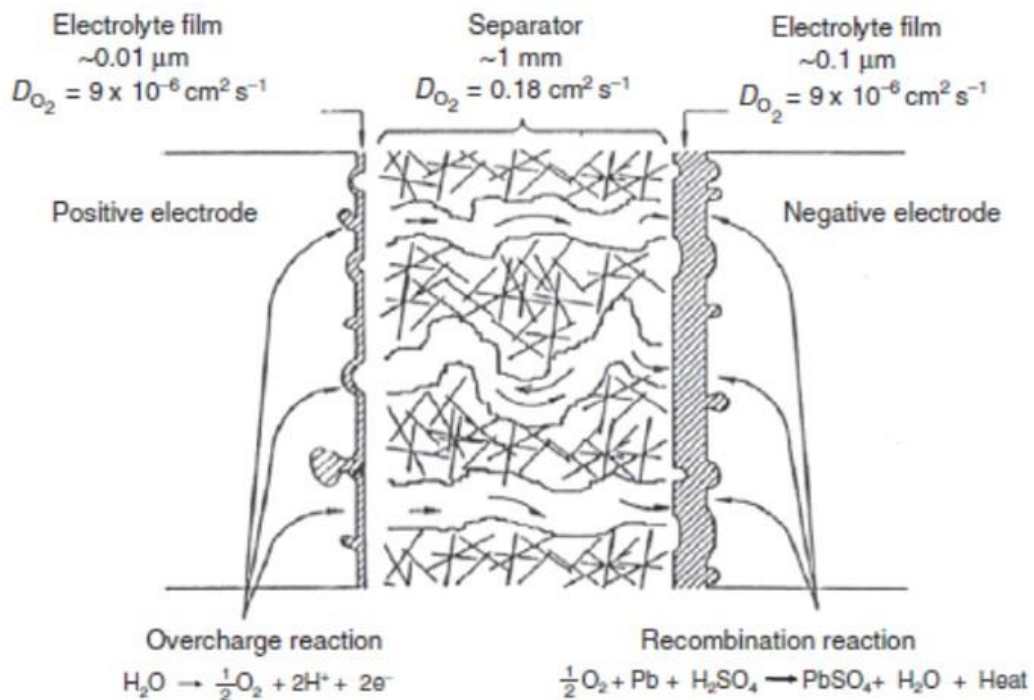


Figure 13. Internal oxygen recombination cycle in VRLA battery (72).

Both gelled and AGM VRLA batteries show significant improvement in water loss and acid stratification with much better performance compared to conventional lead-acid battery (53). AGM batteries are more suited for high power applications, HRPSoC operation than flooded or gelled batteries and are used in back power systems, commercial vehicles, cold cranking application etc. VRLA batteries with carbon additives especially show better HRPSoC performance (64, 65). Whereas gelled batteries have lower power capabilities but longer cycle life. So, they are used in deep cycle applications.

2.3.3 Ultra Battery

Irreversible sulfation on negative Pb electrode is serious limiting factor for charge acceptance and cycle life of lead-acid battery. It is observed in flooded, gel and AGM type batteries with large variation but is one of the main reasons for failure. As mentioned earlier, carbon and graphite additives inhibit sulfation of negative electrode. This quality of carbon in addition to its supercapacitance was indicated to help resolve the sulfation on negative plates. A new configuration of supercapacitor connected in parallel with lead electrodes named as UltraBattery™ (75) was invented by Commonwealth Scientific and Industrial Research Organization based in Australia. This battery used a carbon electrode acting as a supercapacitor that acts as a current sharing buffer with Pb electrode forming an asymmetric supercapacitor in a VRLA type battery as shown in Figure 14. PbO_2 electrode is used as positive electrode against both carbon and Pb as negative electrode. The double layer capacitance of carbon plays a crucial role in working mechanism of UltraBattery. Capacitive current from carbon with faradaic current of

Pb electrode contributes to charging and discharging of negative electrode. Testing of UltraBattery has shown huge improvement in DCA, HRPSoC (76) cycling and power capability (77) compared to AGM technology. A higher cycle life without a voltage drop is also achieved in addition to reduction in mass and weight of the battery since less amount of lead is used.

Variations in UltraBattery with activated porous carbon coated on top of pasted negative and sometimes on positive electrode have also shown similar results. These improved batteries extend working life, help in better utilization of power, increase operating temperature, and reduces internal resistance of battery due to lower internal resistance of asymmetric supercapacitor. Another advantage of these supercapacitor lead batteries is extremely effective suppression of acid stratification even at high cycles (78).

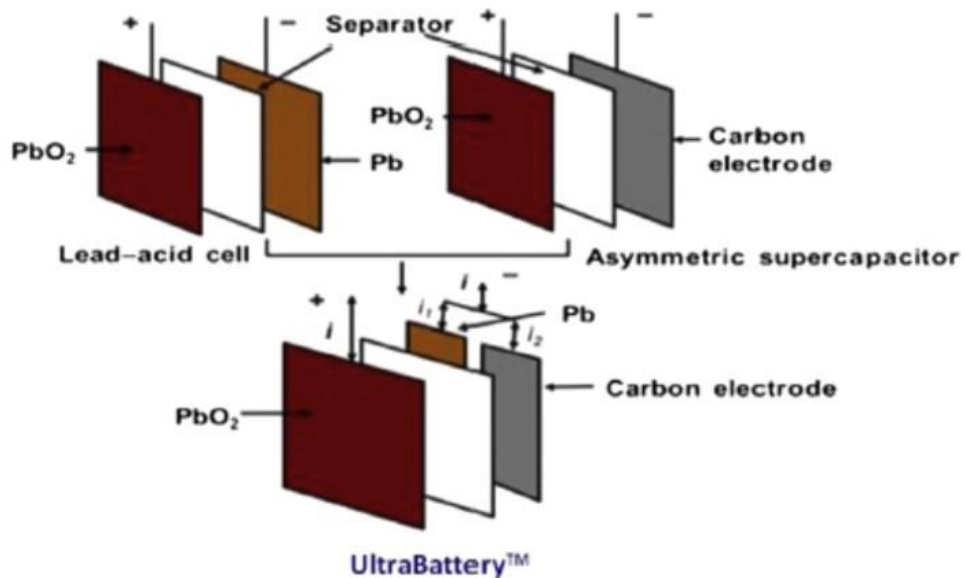


Figure 14. Electrode arrangement in UltraBattery (79).

Application of UltraBattery include mild and micro hybrid vehicles (68, 71) because of better charging during regenerative braking, power tools, remote area power supply, industrial vehicles, etc. Even with all these improvements, UltraBattery has lower specific capacity than AGM VRLA batteries. A betterment of UltraBattery is an ongoing by leading lead-acid battery manufacturers including Furukawa Battery Co., Ltd. in Japan, and East Penn Manufacturing in the United States.

2.3.4 Arc Active Battery

Arc Active technology uses a carbon fibers/fabric or porous carbon material activated using electric arc to fabricate negative electrode with excellent electrical connectivity of Arc Active lead-acid battery. A fine paste slurry of PbO_2 is inserted in the electrochemically active porous or fibric carbon followed by electrode formation that reduces PbO_2 to highly spongy metallic Pb made of nanosized particles with extremely high surface area. This battery also provides similar benefits as other carbon-based batteries with even higher performance specifically allowing fast charging, higher DCA (53) and inhibit negative electrode sulfation. Another variant of this technique is developed in which a composite foam material is used to fabricate the electrodes. Arc Active technology shows high potential for developing demands of energy storage and power consumption in future.

2.4 Challenges in Lead-acid battery chemistry

Lead-acid battery being a complex aqueous system and involvement of variety of additives, impurities, charge discharge condition give rise to number of

limitations that present challenges to achieve desired performance from battery. Different types of batteries present different limitations and challenges with varying intensity. Challenges faced by lead-acid battery to compete with other battery technologies and rising energy demands are summarized in this section with ways to manage them if not possible to avoid them.

In recent years, transportation started gradually moving toward using electric power stored in batteries to reduce greenhouse gas emissions. Batteries required for HEV, EV, PHEV, PEV vehicles need to have high energy and power density which is yet to be achieved by lead-acid technology. For any electric vehicles, DCA is important to recover charge in a battery using regenerative braking. DCA, high-rate discharge and charge of lead-acid battery is low due compared to newer Li-ion technology. Batteries for EVs can be operated to 100% DoD and charge back to 100% DOC on contrary discharging most lead-acid batteries to 100% DoD causes severe damage and recharging capability is greatly reduced. Weight of battery in EVs is another important factor for total milage in single charge, lead-acid batteries are heavy with exception of some recently developed battery types, but they struggle in specific capacity to be used for EVs. Portability and size to energy density ratio is also an obstacle for lead-acid batteries to be used in portable tool and devices because of the same reasons mentioned above. Although there are many challenges, new designs and materials being used for improvement of lead-acid battery show promises of tending to future need of energy storage.

Current limitations in lead-acid battery are well known and have been investigated in past. Remedies to these limitations are proposed in various literatures with varying effectiveness. It is important to point out that not all types of lead-acid batteries suffer through all the limitations mentioned here. The extent of limitation is highly dependent on type of battery, materials used and manufacturer specification for charging and discharging conditions (75). Some of the main limitations in lead-acid batteries not considering any specific type of lead-acid battery are summarized in this section and a particular type of lead-acid battery prone to specific limitation is pointed out. Since remedies that completely get rid of most of these limitations are being developed continuously, it is crucial to understand them in detail.

2.4.1 Acid Stratification

Lead-acid battery electrodes are covered with a passivating layer of $PbSO_4$ after discharge and the sulfuric acid is diluted. During charging $PbSO_4$ dissolves and acid concentration in the cell increases (15). The movement of ions are affected by gravity and the acid tends to settle at the bottom of the cell creating a concentration gradient in lead-acid cell (81). This problem is more intense in flooded and enhanced flooded batteries compared to VLRA batteries (82) since acid is immobilized as described in section 2.4.2. Higher concentration of acid at the bottom leads to irreversible sulfation of electrodes, corrosion, loss of cycle life and service life of battery. As a result of this, active material reduces, and the battery performance does down considerably.

Acid stratification can be minimized by mixing acid in the battery to achieve relatively uniform concentration throughout the length of battery (15). Various agitation equipment can be installed in flooded batteries such as pumps or mechanical assembly to mix the acid solution upon movement of battery (83). Mixing of acid is also achieved by overcharging the battery to vigorously liberate H_2 and O_2 gases at negative and positive electrode although it results in water loss since these gases are released out of the battery through a vent.

2.4.2 Water Loss and Dry Out

H_2 and O_2 gases produced at negative and positive electrodes because of overcharging, corrosion, or self-discharge results in water loss (84). Gassing rates are higher in flooded type batteries than gelled or AGM batteries. In flooded battery, water loss causes increase in acid concentration beyond 5 M that reduces solubility of $PbSO_4$. In Gelled or AGM batteries, water loss causes drying of the gel or AGM separator holding acid solution (75). Drying out results in loss of electrolyte contact with active mass. Therefore, in both cases battery loses its capacity.

This problem is easier to resolve in flooded battery since water is added during regular maintenance. But since VRLA batteries are sealed once the electrolyte is dried out, the battery replacement is necessary.

2.4.3 Electrode sulfation

The term 'Sulfation' in lead-acid battery is used to define irreversible $PbSO_4$ formed at negative electrode (15). Formation of such $PbSO_4$ crystals that can not be converted to Pb during charge happens because of HRPSoC operation, acid

stratification and deep cycling of battery (85). The active Pb mass of the electrode is covered by sulfation crystal, thus it can no longer contribute to charge-discharge cycling. Size and thickness of $PbSO_4$ crystal is especially important in converting $PbSO_4$ back to Pb. It has been observed that smaller crystals are easily dissolved giving out Pb^{2+} ions which then are redeposited on negative electrode. Bigger sulphate crystals are harder to dissolve and become insoluble as they grow further during cycling as shown in Figure 15. Sulfation of negative electrode reduces NAM area and its contact with electrolyte resulting in inability to accept charge by electrode (86). Eventually, entire electrode undergoes permanent sulfation resulting in failure of the battery.

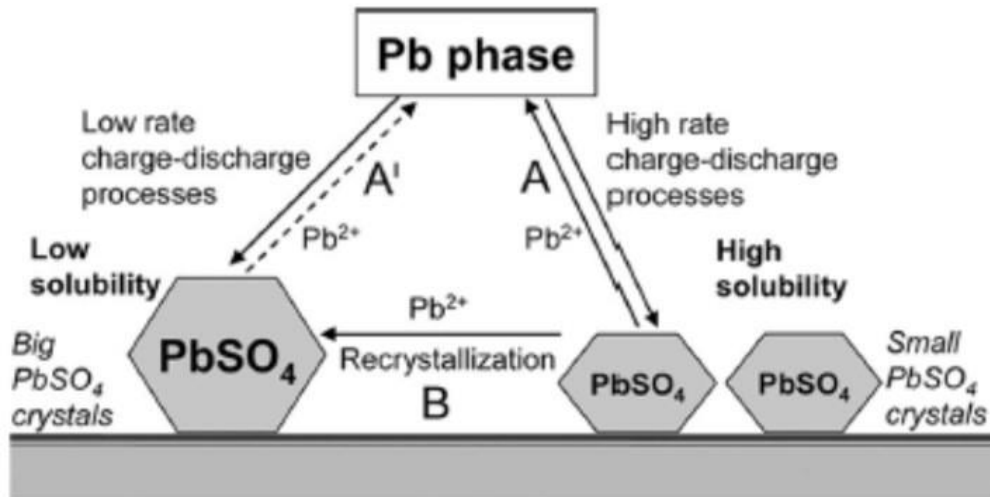


Figure 15. Schematic of $PbSO_4$ crystal size and their solubility (84).

Carbon and graphitic additives in negative electrode minimizes sulfation because of steric hinderance to $PbSO_4$ formation and condutive carbon network (86). Smaller $PbSO_4$ crystals are formed that are easier to dissolve when carbon

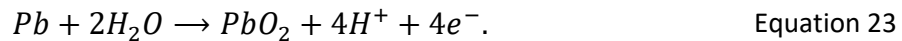
additives are incorporated in the electrode. Ultrabattery and ArcActive battery variation of lead-acid battery are strongly effective against sulfation.

2.4.4 Electrode Volume Expansion

$PbSO_4$ formed during discharge on both electrodes has different volume than Pb and PbO_2 at charged state. Positive PbO_2 electrode experiences roughly 90 – 92% volume expansion (15). The volume expansion of negative Pb electrode is much smaller and of less concern for the failure of battery. Expansion of electrode may happen in either parallel or perpendicular direction of the electrode. A pronounced effect of volume expansion is active mass electrical disconnection from electrode which causes inability to recharge since electrically isolated $PbSO_4$ cannot be converted back to PbO_2 . Mechanical integrity of electrode deteriorates over time and during cycling as the expanded material starts shedding and falling off from electrode surface. Formation and growth of dendritic structures of $PbSO_4$ and PbO_2 also contribute towards volume expansion and may cause internal shorts that causes failure. The electrode plates, current collector grid and separator in the battery are assembled in a compact structure (87) to minimize expansion. Sufficient space for accommodation of expanded volume is accounted for in a lead-acid battery to avoid swelling and failure of structural integrity causing leaks. Leakage is a serious concern because of serious health effects of lead from leaking of concentrated H_2SO_4 containing dissolved lead in the spaces where batteries are stored.

2.4.5 Corrosion of Grid

Current collector grids in lead-acid battery are made from Pb and Pb-Ca alloys. Grid next to positive electrode is susceptible to corrosion at high charging potentials during charging and overcharging (75). Corrosion of positive grid converts Pb to PbO_2 and supporting reaction of H_2 evolution form mixed potentials at the grid. The corrosion reaction of Pb is given as



Grid corrosion is a slow process because corrosion product, PbO_2 forms a non-conductive passive film on positive grid and further corrosion proceeds through cracks in $PbSO_4$ film. Composition and structure of grid, temperature and electrolyte concentration are the most affecting parameter for grid corrosion (16). Corrosion rate increases with acid dilution. As mentioned in earlier chapter, acid concentration decreases after discharge which means damage from corrosion is higher if discharged lead-acid battery is stored. Corrosion products causes growth of the grid which leads to shorting of electrodes, grid collapse due to creeping, and loss of contact with active mass. Corrosion can be reduced by using Pb alloys with higher corrosion resistance and high H_2 evolution overpotential. Positive grid corrosion can be reduced by not operating the Lead-acid battery at top charge or over charge frequently.

2.4.6 Shorting of electrodes

Shorting is when products formed from dissolution and redeposition process happening at electrodes change the morphology of electrode such that a physical

contact occurs between negative and positive electrode. Electrodes lose ability to carry out charge-discharge processes if they are shorted. Shorting may occur from expansion of electrodes or corrosion products penetrating through the separator (75) that acts as spacer between electrodes while allowing ionic transfer. Formation of dendritic structures on electrodes after high cycling may also cause shorts in a battery. Shorting can promote thermal runaway during charging and elevate temperature of battery. Shorting is not reversible and ends service life of lead-acid battery. Shorting risk can be minimized by using proper designs of separators with high resistance to acidic conditions, temperature, and mechanical damage so that the separator deterioration can be avoided. Electrodes completely covered with separator material and addition of sulphate salts is very effective against short-circuits (88).

2.4.7 Gassing

Gassing in lead-acid batteries include H_2 and O_2 gases during overcharging, corrosion, and self-discharge. Extent of gassing varies with type of lead-acid battery and amount of electrolyte present in it. It is responsible for water evaporation in flooded batteries and drying out in VRLA batteries. Impurities in Pb, carbon additives with lower H_2 and O_2 evolution overpotential promote gassing of electrodes. Flooded and EFBs are more prone to gassing and higher water loss than VRLA and supercapacitor lead-acid batteries.

2.4.8 Thermal runaway

Thermal runaway is heating effect in lead-acid battery observed during charging and overcharging that elevates temperature unevenly and uncontrollably. It increases the current drawn by battery during charging and a drop in voltage is observed with higher thermal runaway (78). Some of the problems associated with lead-acid batteries discussed above such as shorting of electrodes, drying out of separator, sulfation of negative electrode may increase possibility of thermal runaway (16). Applying proper charging regime and remedies for the problems discussed above can reduce chances of thermal runaway. In rare cases, it may cause battery failure, explosion, or fire, although it is least likely to happen in lead-acid batteries compared to Li-ion and other batteries.

Temperature is a significant factor affecting the performance of lead-acid battery. Although lead-acid battery can be operated in wide variation of temperature, variation in performance emerges from variation in State of Charge (SoC), cycle life, kinetics of reactions at negative and positive electrodes with temperature. Some factors like solubility of $PbSO_4$ in electrolyte, morphology of $PbSO_4$ formed during discharge, and morphology of redeposited Pb are also affected by operating temperature of the battery. Temperature intensifies some of the challenges such as water loss, electrode volume expansion, changes in acid concentration, self-discharge etc., Charging the battery also causes increase in temperature presenting same issues mentioned above. Therefore, it is important to study the electrochemical response, morphological changes of the electrodes,

charge-current relationship, and charge acceptance at different temperatures to get better fundamental understanding of lead-acid battery technology.

2.5 Graphene Synthesis techniques

Graphene and graphitic carbon materials have been found extremely useful in broad range of applications including rechargeable battery electrodes because of graphene's electrical, catalytic, and electrochemical properties. Graphene can be synthesized by variety of methods such as micromechanical exfoliation, chemical exfoliation, reduction of graphene oxides, mechanical milling etc. But the highest quality of graphene is produced using CVD (80, 81). Transition metal surfaces are the most favorable materials as a substrate to produce graphene which is confirmed using Raman spectroscopy (94) and TEM (95). Graphene synthesis via CVD involves various gases like methane, hexane, ethyne as a carbon source and hydrogen, argon during CVD steps. Pressure and flow rate of these gases must be critically controlled for high quality large area graphene production. Temperature used is usually in the range of 800°C to 1000°C . The mechanism of graphene production involves precipitation of carbon from carbon precursor gases and dissolution of carbon on the metal surface at higher temperatures and resurfacing of carbon in the form of graphene during substrate cooling down. Carbon is soluble in all transition metals with variation in solubility amount (96). Copper is the most widely used transition metal (97) for graphene synthesis and carbon has solubility in Cu of about 0.02% as shown in Figure 16. Various CVD methods that use lower temperature and shorter growth time such as low-pressure CVD, plasma enhanced CVD etc. have been

developed. But CVD is still low throughput and complicated method for graphene production.

The method used for graphene production on transition metal in this work is completely in solid state except for Ar gas environment to protect transition metal surface from oxidation at high temperature. The graphene synthesis is done using carbon black milled using high energy ball mill for 2 hr (98) and a heat-treated copper surface pressed together in a copper or niobium die at 7 Mpa followed by induction heating in Ar environment to 950°C for 30 min then 600°C for 10 min and cooled down to R.T. The quality of graphene produced is assessed by Raman spectroscopy mapping and HRTEM.

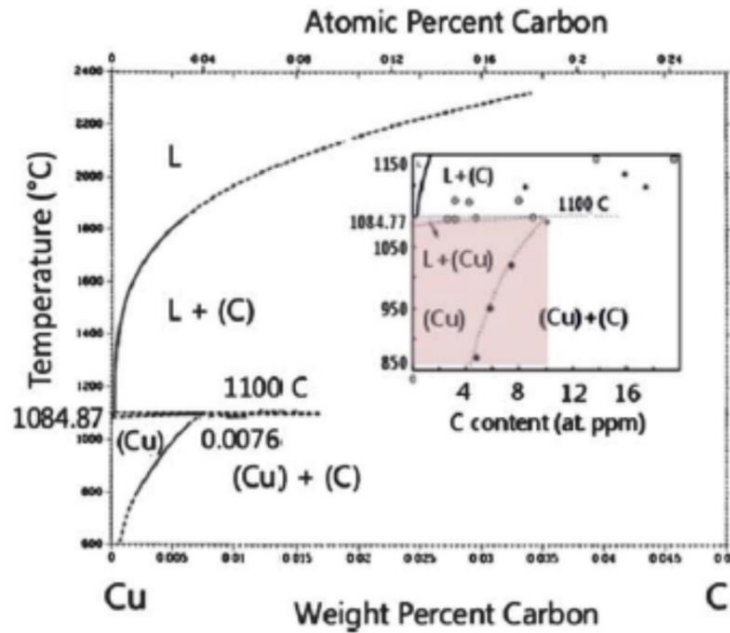


Figure 16. Carbon and Copper binary phase diagram (99).

Chapter 3

Charge-Discharge Evaluation of Lead-acid battery

3.1 Charge-Discharge Relationship

Lead-acid battery was the first rechargeable battery technology used in practical applications and a relationship of current drawn from the battery for known amount of time to remaining capacity of the battery was proposed by Wilhelm Peukert. This empirical current charge relationship is used for capacity estimation of Lead-acid (100–102), Li-ion (103–105), Ni-Cd batteries, and supercapacitors (106). Higher discharge current causes higher intrinsic losses because of increased internal resistance of cells in the battery. Peukert coefficient is affected by the intrinsic losses, and it varies with type of battery. Peukert coefficient closer to 1 is ideal and desired for high battery capacity, as it is possible in AGM VRLA batteries with its value ranging from 1.05 to 1.15. For gelled batteries, it is between 1.1 to 1.25 and for flooded batteries, it is between 1.2 to 1.5 (107).

3.1.1 Peukert Law

The Peukert relationship for a battery is expressed as

$$Q^0 = j_d^k t_d, \quad \text{Equation 24}$$

where, Q^0 is intrinsic discharge capacity (Ah), j_d is discharge current (A), t_d is discharge time (hr) and k is Peukert coefficient. This form of equation is for constant current discharge i.e., for galvanostatic discharge. Peukert law is most accurate when the discharge is done at constant current and limited temperature

variations. In practice, batteries are discharged at wide range of discharge currents and operating temperatures and the simplistic model in Equation 24 fails in predicting remaining capacity in these conditions. Many modifications of Peukert relationship that account for the current and temperature contribution are developed.

In this work, we introduce another version of Peukert law given in Equation 25 which can be used to for discharge-charge performed in potentiostatic mode using CV as given by

$$Q^0 = (j_d^1 t_d)j^{0.5} = Q j_d^{0.5}. \quad \text{Equation 25}$$

The Peukert coefficient changes to $k' = -0.5$ for potentiostatic mode after Equation 25 is rearranged to get

$$Q = Q^0 j_d^{-0.5}, \quad \text{Equation 26}$$

where, Q is discharge capacity calculated by integrating area under anodic peak of CV and Q^0 is intrinsic discharge capacity. It is usually plotted in Log form since it is linear with a slope of $k' = -0.5$ and exponent of y-axis-intercept gives Q^0 . In this work, a Peukert law derivation is presented that is related to Pb^{2+} and HSO_4^- ion concentration gradient, $PbSO_4$ nucleation and growth kinetics and Pb^{2+} solubility. Changes in Peukert coefficient and intrinsic discharge capacity are studied for 6 different temperatures of $-20^\circ C, -5^\circ C, 10^\circ C, 25^\circ C, 40^\circ C$ and $55^\circ C$ during Pb electrode discharge.

3.1.2 Peukert Law for Pb^{2+} Ion Gradient

The 'Kugelhaufen' model also known as 'Agglomerate of Spheres' (AOS) model with nucleation and growth principles are used to derive the first principles Peukert relationship. AOS model assumes that $PbSO_4$ crystals formed on Pb surface are closely packed spheres with diameter, d , as shown in the schematic of Figure 17.

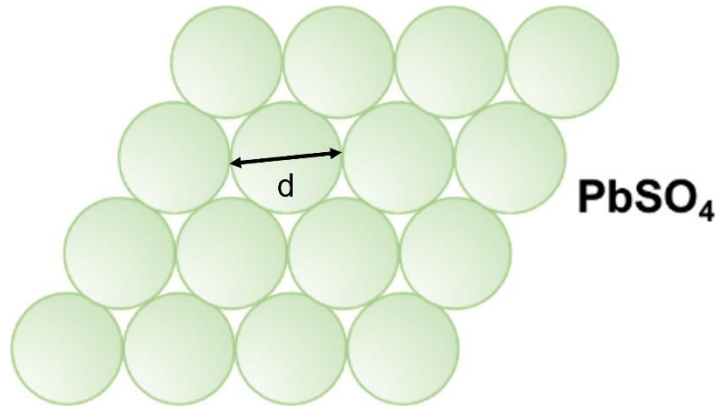


Figure 17. Schematic of Agglomerate of Sphere model.

For a 100% DoD Pb sample, the $PbSO_4$ particle size can be approximated by normal distribution with center at mean particle size, d^0 and total number of particles, N_0 as

$$N(d) = \frac{N^0}{\sigma\sqrt{2\pi}} \exp\left[-\frac{1}{2}\left(\frac{d-d_0}{\sigma}\right)^2\right], \quad \text{Equation 27}$$

where, σ is the standard deviation. Since we have defined mean particle size, d^0 , we can apply the same normal distribution to establish total area covered by $PbSO_4$ spheres would be the area projected by spheres on Pb underneath as

$$\begin{aligned} A_{total} &= \sum[N(d)A_{projected}] \quad \text{Equation 28} \\ &= N^0 \left(\frac{\pi}{4\sigma\sqrt{2\pi}}\right) \int d^2 \exp\left[-\frac{1}{2}\left(\frac{d-d_0}{\sigma}\right)^2\right] \partial d. \end{aligned}$$

In this equation, the projected area by individual sphere is given as

$$A_{projected} = \frac{\pi}{4} d_0^2. \quad \text{Equation 29}$$

Similarly, total mass of $PbSO_4$ by particle mass distribution is given as

$$\begin{aligned} m_{total} &= \sum [N(d) m_{sphere}] \quad \text{Equation 30} \\ &= N^0 \left(\frac{\pi \rho}{6\sigma\sqrt{2\pi}} \right) \int d^3 \exp \left[-\frac{1}{2} \left(\frac{d - d_0}{\sigma} \right)^2 \right] \partial d. \end{aligned}$$

and mass of individual sphere is given by

$$m_{sphere} = \frac{\pi \rho}{6} d_0^3, \quad \text{Equation 31}$$

where, ρ is the density of $PbSO_4$.

Now the maximum charge obtained after 100% DoD can be expressed as a function of total mass of $PbSO_4$ using Faraday' first law given as

$$Q_{max} = \frac{nF}{M_{PbSO_4}} m_{total}, \quad \text{Equation 32}$$

where, M_{PbSO_4} is molecular weight of $PbSO_4$.

Now multiplying and dividing by A_{total} and substituting Equation 28 and 30 in Equation 32 and assuming narrow distribution, $\frac{d_0}{\sigma} \gg 1$ as a boundary condition for normal distribution gives Q_{max} as a function of A_{total} and d_0 of $PbSO_4$ given as

$$Q_{max} = \frac{2nF\rho}{3M_{PbSO_4}} A_{total} \left(\frac{\langle N(d)|d^4 \rangle}{\langle N(d)|d^3 \rangle} \right). \quad \text{Equation 33}$$

Therefore, final expression for maximum charge extracted after 100% DoD is

$$Q_{max} = \rho_p \frac{nF\rho}{M_{PbSO_4}} A_{total} d_0, \quad \text{Equation 34}$$

where, ρ_p is the packing density of $PbSO_4$ unit cell. For single layer of spheres on Pb surface, $\rho_p = \frac{2}{3}$ and for dense layer it is $\rho_p = 1$. Equation 34 relates the discharge capacity of Pb electrode with $PbSO_4$ total area and particle size. The number of particles assumed here by normal distribution depends on number of $PbSO_4$ nuclei nucleating on Pb surface. Nucleation rate of $PbSO_4$ nuclei increase with Pb^{2+} ion concentration near Pb electrode increases and it is highest when electrolyte becomes supersaturated. So, nucleation is proportional to supersaturation in index, SI , defined as a ratio of Pb^{2+} concentration at the surface to its concentration at saturation i.e., equilibrium solubility of Pb^{2+} ions. SI is given as

$$SI = \frac{C_{Pb^{2+}}}{[Pb^{2+}]}, \quad \text{Equation 35}$$

where, $[Pb^{2+}]$ is solubility of Pb^{2+} ions, $C_{Pb^{2+}}$ is concentration of Pb^{2+} in electrolyte near interface. And according to Fick's first law of diffusion, the flux of moles Pb^{2+} ions per unit area per unit time from higher to lower concentration is proportional to concentration gradient and is expressed as

$$J_{Pb^{2+}} = -D_{Pb^{2+}} \left(\frac{\partial C_{Pb^{2+}}}{\partial x} \right), \quad \text{Equation 36}$$

where, J is flux of moles ($mol\ cm^{-2}\ s^{-1}$), D is Diffusion coefficient ($cm^2\ s^{-1}$) and $\frac{\partial C_{Pb^{2+}}}{\partial x}$ is concentration gradient in direction x .

The current density limited by diffusion is given as

$$j = nFD \left(\frac{C_{Pb^{2+}}}{\delta_{dif}} \right), \quad \text{Equation 37}$$

where, j is diffusion limited current density ($A\ cm^{-2}$) and δ_{dif} is diffusion layer thickness. Since nucleation is related to saturation of Pb^{2+} ions, density of nuclei is proportional to SI and can be given as

$$\frac{N}{\delta_{diff} A_{total}} = k_{precp} \frac{C_{Pb^{2+}}}{[Pb^{2+}]}, \quad \text{Equation 38}$$

where, k_{precp} is precipitation constant. Substituting $C_{Pb^{2+}}$ from Equation 37 in Equation 38, we get

$$N = \frac{j \delta_{dif}^2 k_{precp} A_{total}}{nFD_{Pb^{2+}} [Pb^{2+}]}. \quad \text{Equation 39}$$

The mean particle size from rearranging $A_{total} = \frac{\pi N d_0^2}{4}$ is obtained as

$$d_0 = \left(\frac{4 A_{total}}{\pi N} \right)^{\frac{1}{2}}. \quad \text{Equation 40}$$

Now using N from Equation 39 in Equation 40 and resulting d_0 in Q_{max} in Equation 34, we get a charge-current relationship related to Pb^{2+} ion gradient and nucleation and growth of $PbSO_4$ layer given as

$$Q = \frac{\delta_p 4F\rho}{M_{PbSO_4}} \left(\frac{(2F D_{Pb^{2+}})}{\pi \delta_{dif}^2} \right)^{\frac{1}{2}} \left(\frac{[Pb^{2+}]}{k_{precp}} \right)^{\frac{1}{2}} j^{-\frac{1}{2}}. \quad \text{Equation 41}$$

Above equation in simplified form can be stated as

$$Q = Q^{0'} \left(\frac{[Pb^{2+}]}{k_{precp}} \right)^{\frac{1}{2}} j^{-\frac{1}{2}}. \quad \text{Equation 42}$$

Pb^{2+} solubility and thereby the saturation index would be affected by temperature. So, the solubility of Pb^{2+} has been measured using ICP-MS at all the temperatures mentioned in the experimental procedure and it changes significantly with temperature. Changes in supersaturation index with temperature would most likely be the reason for morphological changes observed in $PbSO_4$ using AFM and FIB SEM. It is discussed further in results in Chapter 6.

3.1.3 Peukert Law - Pb^{2+} and HSO_4^- Ion Gradient

Pb^{2+} solubility also depends on concentration of H_2SO_4 and as shown from the ICP-MS data in Figure 18, the concentration of H_2SO_4 changes during charging and discharging process. Therefore, an acid gradient which is given by Fick's first law as

$$C_{H_2SO_4}^s = C_{H_2SO_4}^0 - \frac{j\delta_{dif}}{nFD_{HSO_4^-}}. \quad \text{Equation 43}$$

Here, $C_{H_2SO_4}^s$ and $C_{H_2SO_4}^0$ are H_2SO_4 concentrations in solution and at $x = 0$. Pb^{2+} solubility changes with acid gradient at the interface so Pb^{2+} solubility according to Fick's law of diffusion can be stated as

$$[Pb^{2+}] = [Pb^{2+}]^0 + \frac{\tau\delta_{dif}}{2FD_{HSO_4^-}} j. \quad \text{Equation 44}$$

Substituting $[Pb^{2+}]$ from Equation 44 in single gradient Peukert relationship shown by Equation 42, the extended current-charge relationship includes both Pb^{2+} and HSO_4^- gradients given by

$$Q = \frac{\delta_p 4F\rho}{M_{PbSO_4}} \left(\frac{(2F D_{Pb^{2+}})}{\pi \delta_{dif} k_{precp}} \right)^{\frac{1}{2}} j^{-\frac{1}{2}} \left([Pb^{2+}]^0 + \frac{\tau \delta_{dif}}{2F D_{HSO_4^-}} j \right)^{\frac{1}{2}} \quad \text{Equation 45}$$

Above equation can be written in simplified form as

$$Q = Q^{0'} (\alpha + \beta j)^{\frac{1}{2}} j^{-\frac{1}{2}}. \quad \text{Equation 46}$$

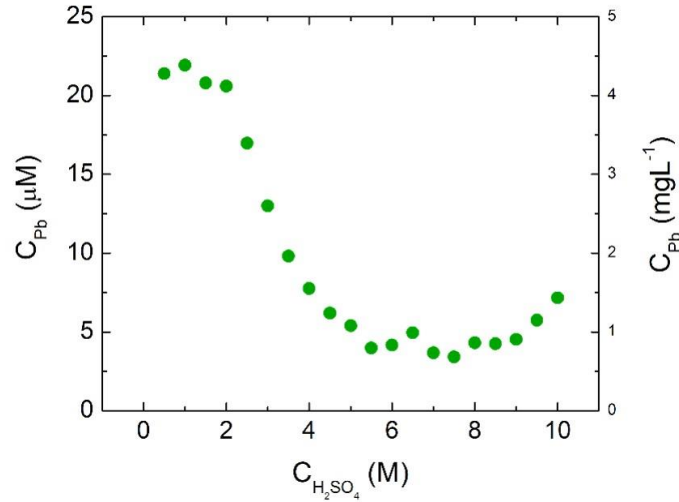


Figure 18. Pb^{2+} solubility vs concentration of H_2SO_4 .

3.2 Charge Acceptance

Charge acceptance of all types of rechargeable batteries used in any applications is attracting interest all over the world since higher charge acceptance means higher charging efficiency and faster recharging of battery. It is especially important in HEV, PHEV and EVs because energy generated by braking or deceleration is used to charge the battery of vehicles and as a result, battery undergoes microcycling at HRPSoC conditions. The current generated by braking is known as recuperation current, $I_{recuperation}$ which is generated in pulses that are

provided for recharging the battery. The current pulses up to 30 times 1-hr rate (30 C) are generated during regenerative braking.

3.2.1 Dynamic Charge Acceptance

Charge acceptance from high current pulses during HRPSoC cycling is commonly known as Dynamic Charge Acceptance. Figure 19 shows a profile of standard microcycle test established by 'European Standard DCA test A3 specification (108, 109). One microcycle consists of 10 s charge pulse (A-B) then 30 s rest (B-C) after which a discharge pulse (C-D) followed by second 30 s rest time (D-E). A maximum voltage limit is set during charging since current pulses increases terminal voltage of the battery. Charging current pulse is decreased if maximum voltage of about 2.47 V for one lead-acid cell is reached. $I_{recuperation}$ and its duration in seconds is used for DCA calculation normalized by battery capacity in Ampere-hrs. (108, 109).

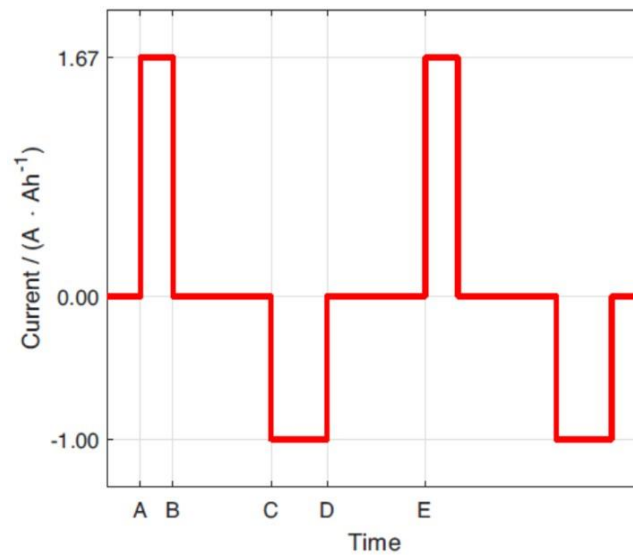


Figure 19. Standard DCA test, (A-B) charge pulse, (B-C) rest period, (C-D) discharge pulse and (D-E) is another rest period (109).

The DCA ($A \cdot Ah^{-1}$) for a battery is calculated as

$$I_{recuperation} = \frac{(A \cdot h_{recuperation}) \times 3600}{C \times t}, \quad \text{Equation 47}$$

where, $A \cdot h_{recuperation}$ is charge (Ah) from current pulse, C is the rated nominal capacity (Ah) of the battery and t (s) is the time of current pulse. Equation 47 uses galvanostatic charging current since battery is charged using current pulse.

As mentioned in chapter 4, cyclic voltammetry is used in this work for electrochemical investigation of Pb electrode since it has advantages such as controlling electrode polarization potentials and faster or slower potential scan rate can discharge or charge the electrode faster or slower respectively. Equation 48 can be used to represents charge acceptance like in Equation 47 but in potentiostatic mode instead of galvanostatic mode. Charge acceptance is studied with respect to kinetics of electrochemical reactions at Pb electrode and it is labelled as Kinetic Charge Acceptance. KCA using CV is give as

$$KCA = \frac{J_{charge} @E(V)}{Q_d}, \quad \text{Equation 48}$$

where, J_{charge} is current density ($A \text{ cm}^{-2}$) at chosen negative potential and Q_d is total discharge capacity ($Ah \text{ cm}^{-2}$) calculated by integrating discharge peak in the CV as mentioned in section 4.4.4.

3.2.2 Potential Selection for J_{charge} in KCA

KCA protocol in this work is used to quantify the dissolution of $PbSO_4$ as a function of lead sulphate layer thickness estimated from electrochemical

experimental data and its correlation to actual thickness and particle size observed using FIB-SEM and AFM. The asymmetric CV protocol mentioned in section 5.2.2 for KCA uses current at fixed potential during charge scan to calculate KCA defined in Equation 48. The negative potential chosen for $J_{charge} @E(V)$ is such that it mostly includes $PbSO_4$ dissolution than Pb^{2+} redeposition and avoids HER. Choosing high negative potential will be less sensitive in providing $PbSO_4$ dissolution information. Therefore, two sets of potentials, first at peak charge current and second at -1.2 V are chosen for KCA calculations as shown by dashed black drop lines in Figure 20 for a 10 mV/s charge curve after 5 mV/s discharge curve. The $KCA^{corrected}$ using charge scan current at chosen potential then becomes

$$KCA^{corrected} = \frac{J_{charge} @E(V)}{Q_d - Q_c^{@E(V)}}, \quad \text{Equation 49}$$

where, $Q_c^{@-E(V)}$ is charge capacity calculated using charge scan from -1.0 V to -1.2V or peak current potential. The effect of charging process on remaining $PbSO_4$ thickness, $l_{PbSO_4}^{corrected}$ is calculated by using electrochemical thickness data and Faraday's law. $l_{PbSO_4}^{corrected}$ after charge scan up to chosen termination potential is calculated as

$$l_{PbSO_4}^{corrected} = \frac{(Q_d - Q_c^{@E(V)})M_{PbSO_4}}{2F\rho_{PbSO_4}}. \quad \text{Equation 50}$$

The KCA of Pb electrode with $l_{PbSO_4}^{corrected}$ is discussed in results in Chapter 6.

KCA: 10 mV/s Charge at 25 °C in 5 M H₂SO₄

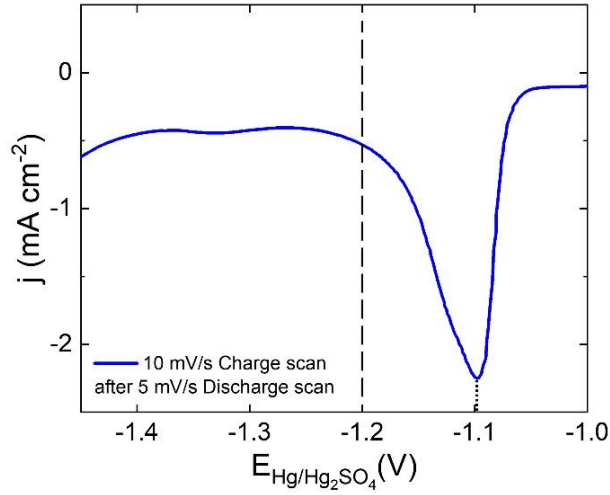


Figure 20. Choice of potential for $J_{charge} @E(V)$.

3.2.3 Correlation between KCA and Lead Sulphate Dissolution Kinetics

Charging of Pb electrode consists of two competing reactions, first is chemical dissolution of $PbSO_4$ and second, electrochemical redeposition of Pb, shown in Equation 52 and 51 as



and



The total charge current has an electrochemical contribution from Pb redeposition and chemical contribution from chemical dissolution of $PbSO_4$. Total charge current per square cm is represented by

$$\frac{1}{j_{charge}} = \frac{1}{j_{chem}} + \frac{1}{j_{diss-chem}}. \quad \text{Equation 53}$$

At high charging current in galvanostatic mode and high negative potentials in potentiostatic mode, the electrochemical step for Pb redeposition is fast. Therefore, charging process becomes limited by chemical dissolution of $PbSO_4$. The j_{chem} of charge transfer reaction of Pb electrochemical deposition is given by Butler-Volmer kinetics as

$$j_{chem} = nFA_{Pb}k^0C_{Pb^{2+}}e^{\frac{nF(1-\alpha)(E-E^0)}{RT}}\theta_{Pb}, \quad \text{Equation 54}$$

where, n is number e^- involved in reaction, F is Faraday constant, A_{Pb} is area of Pb electrode, k^0 is rate constant, $C_{Pb^{2+}}$ is concentration of Pb^{2+} ions, α is charge transfer coefficient, E^0 is equilibrium potential of Pb^{2+}/Pb , E is applied potential and θ_{Pb} is exposed Pb coverage. The $j_{diss-chem}$ of chemical dissolution reaction is given as

$$j_{diss-chem} = k_{diss}(d^0, (hkl), temp) A_{PbSO_4}(d^0, E, t), \quad \text{Equation 55}$$

where, k_{diss} is dissolution constant that depends on $PbSO_4$ particle size d^0 , crystal orientation (hkl) and temperature during dissolution, A_{PbSO_4} is area covered by $PbSO_4$ that depends on d^0 and discharge scan rate. Combining Equation 49 and 55, and using charge term derived from AOS model and normal distribution for $PbSO_4$ particles, KCA is expressed as a function of $PbSO_4$ thickness by

$$KCA^{corrected} = \frac{k_{diss}A_{PbSO_4}}{m_{PbSO_4}} \Big|_v \cong k_{diss} \left(\frac{\lambda}{l_{PbSO_4}^{corrected}} \right), \quad \text{Equation 56}$$

where, λ contains constants.

Chapter 4

Materials and Characterization Techniques

The first part of this chapter contains materials and techniques used for graphene synthesis and characterization on transition metal surface completely in solid state without using any toxic gases or solutions as used in CVD method for graphene production. This proof-of-concept process of solid-state graphene synthesis can be used to introduce graphene or achieving graphene coverage in battery electrodes either containing traces of transition materials or by transferring graphene produced on transition metal surface to battery electrode. The second part of this chapter materials and characterization methods used for studying negative lead electrode current-charge relationship and kinetic charge acceptance at temperatures ranging from -20°C to 55°C . In this chapter, the materials required for both the studies are discussed with reasoning behind choice of materials. Sample surface is of particular importance in both graphene synthesis and electrochemical testing of Pb for fundamental exploration of its behavior in lead-acid battery. Therefore, surface preparation and treatments carried out on samples before the beginning of experiments are explained in this chapter as well. Along with materials, the characterization techniques such as Raman spectroscopy and mapping, voltammetry, AFM-TUNA and FIB-SEM imaging used during and after experiments are discussed.

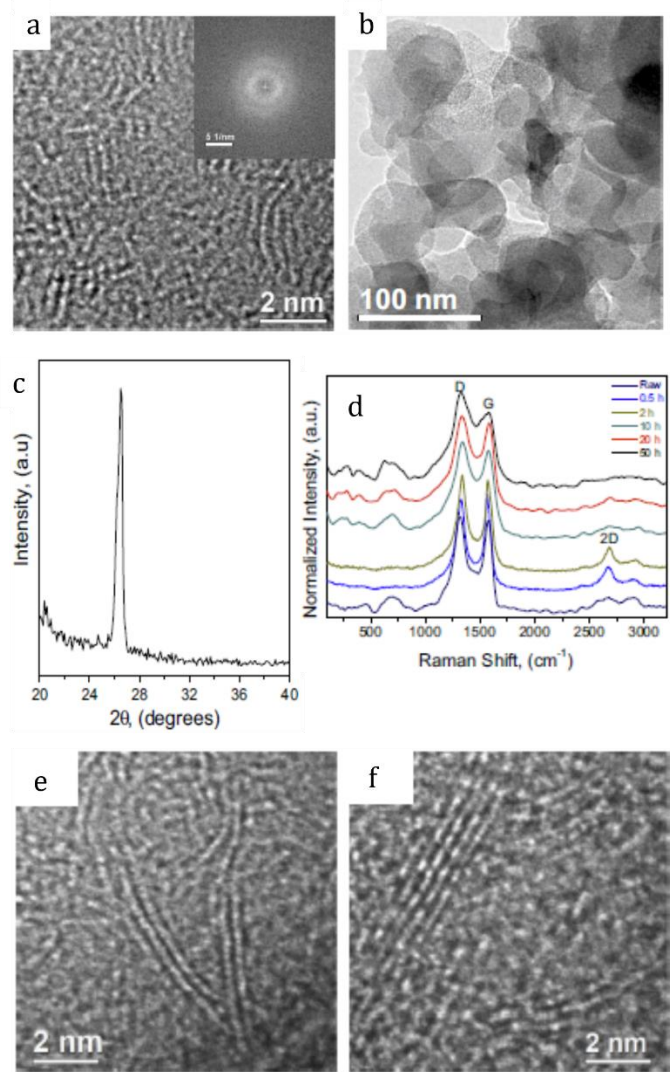


Figure 21. (a)HRTEM image, (b) bright field image, (c) XRD peak of raw carbon black, (d) Raman spectra vs milling time, (e) HRTEM of 0.5 hr and (f) HRTEM of 2 hr milled carbon black (110).

4.1 Materials for graphene synthesis

A Carbon black powder used for graphene synthesis on copper substrate is commercially produced as a byproduct of Krätschmer method for fullerene soot production. Carbon black powder contains nanosized amorphous particles seen in HRTEM and bright field images in Figure 21a, b with 2θ XRD peak at 26.7° as shown

in Figure 21c and Scherrer particle size of 0.69 nm (110). Copper is used in foil and polycrystalline slug of thicknesses 0.1 mm and 3 mm.

4.1.1 Morphed Graphene

The previous work of F. C. Robles-Hernandez et al. on carbon black mentioned above shows increase in crystalline sp^2 morphed graphitic carbon structures using high energy ball milling (111). Different milling times between 0.5 hr to 50 hr produce different graphitic layers detected by Raman spectra shown in Figure 21d. 2 hr ball milling creates 4 to 5 graphitic layers as seen by increase in 2D peak intensity. These graphitic structures after 0.5 and 2 hr ball milling can be seen in HRTEM images shown in Figure 21e, f. The 2 hr milled carbon black is chosen as graphene precursor or seed for graphene synthesis on copper.

4.1.2 Copper surface treatment

Copper surfaces of foil and slug are mechanically polished starting from rougher 800 grit up to 2500 grit fine polish paper and sonicated in DI water. Then polished on TexMet C polishing cloth using alumina powders from 5 μm to 50 nm followed by sonication in DI water to create a smooth scratch free flat surface. The polished Cu surface is cleaned with 20% H_2SO_4 solution to get rid of surface impurities then rinsed with DI water and dried with Ar jet before annealing. Annealing is done for 8 hr at 1000⁰C in Ar atmosphere before using the substrate for graphene synthesis. Annealing develops terraces in Cu grains as shown in Figure 22a, b along [100] crystallographic direction.

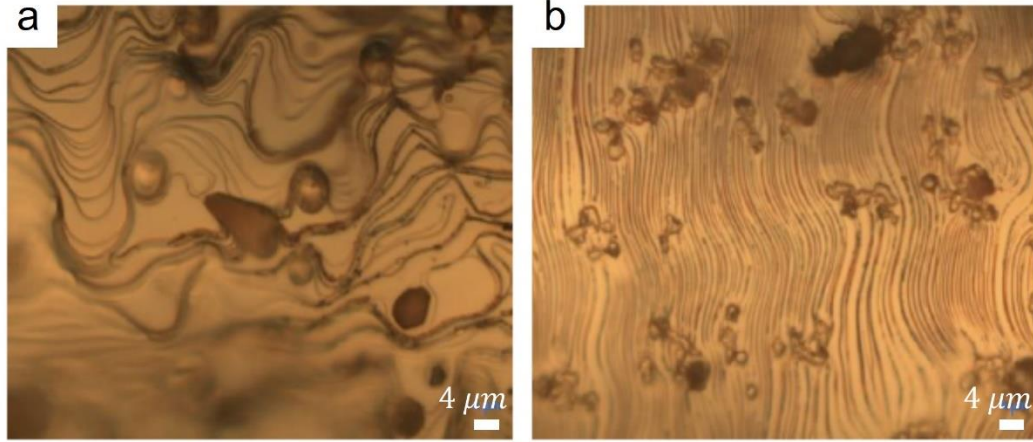


Figure 22. (a) 8 hr annealed, (b) 10 hr annealed Cu sample.

4.2 Graphene Characterization using Raman spectroscopy

Raman spectra of various forms of carbon have been studied extensively and it is used to identify and analyze amorphous and crystalline carbon structures. Raman spectroscopy has proved to be a great technique for quantitative and qualitative assessment of graphene. There are 3 main peaks or bands namely D, G and 2D and their intensity ratios from Raman spectra of graphene (112) are used for quality assessment of graphene shown in Figure 23a, b. Intensity of peaks is related to on Raman scattering intensity (I_R) which depends on laser power and wavelength, polarizability of samples and quantity of sample and it is given by

$$I_R \propto \nu^4 I_0 N \left(\frac{\delta\alpha}{\delta Q} \right)^2, \quad \text{Equation 57}$$

where, ν laser frequency, I_0 is incident laser intensity, N is number of scattering molecules, α is molecule polarizability and Q is vibrational amplitude (113). Therefore, all parameter affecting Raman scattering intensity are kept same during

Raman spectroscopy of different samples so the spectra can be compared for graphene assessment.

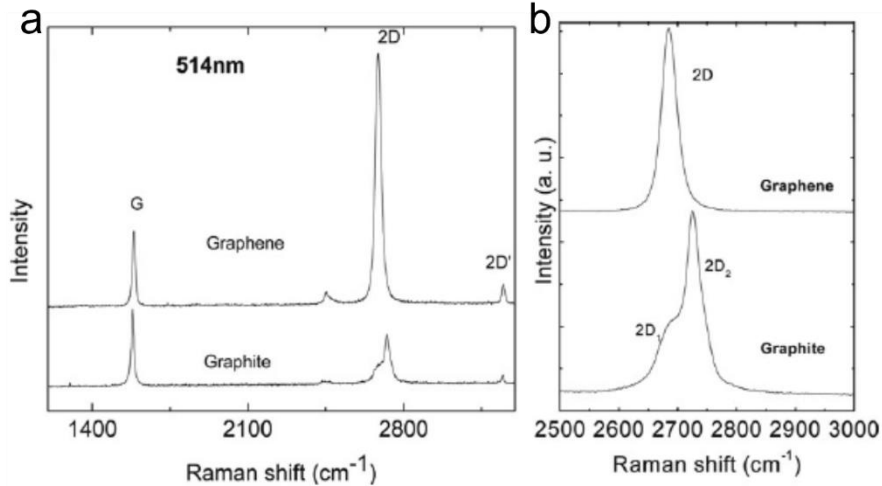


Figure 23. (a) graphite and graphene Raman spectra, (c) width variation of 2D peak for graphite and graphene (112).

4.2.1 Graphene Quality Assessment

The D band at $\sim 1350\text{ cm}^{-1}$ in Raman spectra represents breathing modes of sp^2 bonded carbon. High D band indicates defects, edges, or folds in graphene. G band next to D band at $\sim 1582\text{ cm}^{-2}$ represents stretching of sp^2 bonded C-C bond. The 2D band further down at $\sim 2700\text{ cm}^{-2}$ with FWHM of $\sim 25\text{ cm}^2$ is indicative of graphitic carbon structures. The intensity of 2D band depends on the number of graphene layers stacked on top of each other (114). Low intensity 2D band is seen for graphite which is usually considered as ≥ 5 graphene layer stacking. For single layer graphene, 2D band intensity is higher than G band. Intensity ratio of 2D to D band ($\frac{I_{2D}}{I_D}$) defines number of graphene layers and ratio of D to G band ($\frac{I_D}{I_G}$) defines

defects or quality of graphene (115). Therefore, the intensity ratio ($\frac{I_{2D}}{I_G}$) around 2 is for single layer graphene (116) and about 0.5 or less represent graphite with 5 or more number of layers for 532 nm laser wavelength. The ratio ($\frac{I_{2D}}{I_G}$) changes with wavelength of laser used for Raman spectroscopy as shown in Table 2. Quality of graphene is indicated by intensity ratio of D band to G band ($\frac{I_D}{I_G}$) (117). Smaller ratio of ($\frac{I_D}{I_G}$) close to zero means graphene sheet has low defects or folds. Therefore, for ideal high quality SLG high ($\frac{I_{2D}}{I_G}$) (116) and low ($\frac{I_D}{I_G}$) ratios are desired.

Table 2. No. of graphene layers for I_{2D}/I_G ratio at 488 nm and 325 nm laser wavelength.

No. of layers, n	1	2	3	4	5
VIS ($\lambda = 488 \text{ nm}$)	4.17	1.35	0.88	0.67	0.48
UV ($\lambda = 325 \text{ nm}$)	0.11	0.44	0.40	0.44	0.28

4.2.2 Raman Mapping for Graphene Detection

Raman spectra was obtained from laser spot of 1 μm diameter focused on sample therefore two consecutive laser spots cannot be separated by distance less than 1 μm . Characterization using Raman mapping can cover area in sq. mm which can be selected via Labspec6 software controlling Horiba Scientific Xplore One instrument that is used for this work. Raman mapping can create a localized spatial map where graphene is present on the selected area (116). A 20 μm^2 area of Cu sample with graphene synthesized on its surface is chosen for Raman mapping with Raman spectrum obtained at every 1 μm step. Sample mounted on a motorized

stage with X, Y and Z direction movement capability autofocuses laser spot on each point during acquisition of Raman spectra for selected area. A CCD detector with pixelated array detects Raman scattered light and constructs a map representing all the peaks in the spectra. A grating of 600 (*grooves/mm*) is used for resolution of Raman map. A schematic representation of mapping process is shown in left part of Figure 24. The right part shows Raman imaging which forms an image from scattered Raman intensities from the sample.

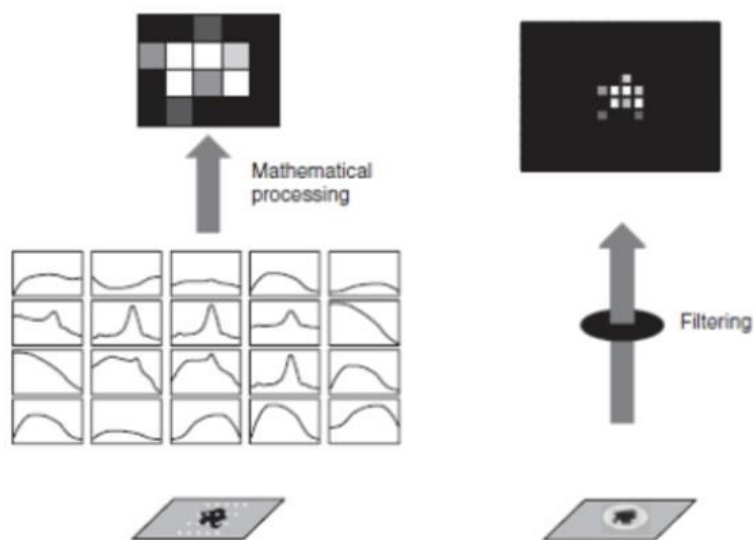


Figure 24. Schematic representation of Raman mapping (113).

4.3 Materials and for Lead-acid electrochemistry

The focus of this work is on understanding negative electrode behavior in lead-acid acid battery and to establish baseline performance, purity of Pb used as working electrode and H_2SO_4 for electrochemical experiments is important to avoid contributions of other elements and additive in discharge and charge process. An ultra-pure zone refined Pb rod with purity of 99.9999% from Alfa Aesar is used to

make Pb samples. A 98% stock sulfuric acid of OmniTrace Ultra grade from MilliporeSigma is diluted using 18.2 $M\Omega$ DI water to make 5 M H_2SO_4 concentration and deaerated by bubbling ultra-pure Ar gas for 30 min before experiments.

4.3.1 Lead Disk Preparation

A Pb disk of 6 mm diameter and roughly 4 mm height is punched from oversized Pb rod shown in Figure 25a, b. Since Pb is soft metal and mechanical polishing would introduce impurities to Pb surface, the Pb disk is pressed in hydraulic press at 50 psi pressure against a flat mirror polished stainless steel surface to obtain flat Pb surface while maintaining same diameter of 6 mm as shown in Figure 25c. The flat Pb surface is then electropolished with procedure explained in section 4.3.2.

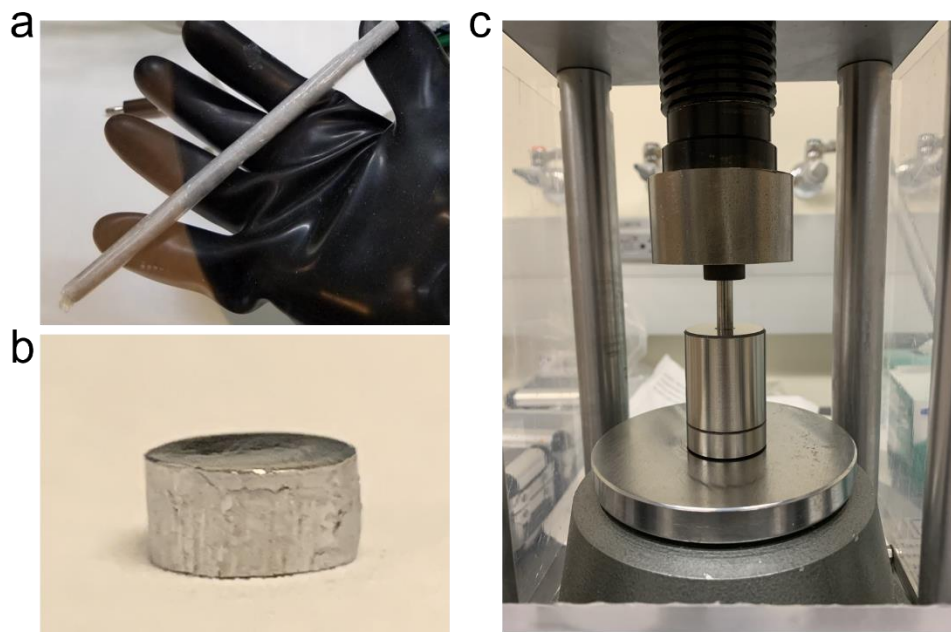


Figure 25. (a) Lead rod (b) punched Pb disk (c) hydraulic press with Pb disk against polished steel surface.

4.3.2 Lead Electropolishing Solution

Electropolishing solution is prepared by adding 28.5 g of anhydrous Sodium Acetate in 38.1 ml DI water followed by shaking well then adding 150 ml Acetic acid and sonicating in water bath for 1 hr and set aside for 12 hr for Sodium Acetate to dissolve completely. 0.5 g of Lead Acetate is added in about 30 to 40 ml of above solution. It is observed that electropolishing results are better if some amount of dissolved Pb is present in electropolishing solution. The solution is replaced after about 2 months of regular use to maintain electropolishing consistency.

4.4 Cyclic Voltammetry

In this work, electrochemical testing is done using Autolab Potentiostat model PGSTAT302N for all experiments. Two types of potential sweep waveforms are used, namely 'staircase' and 'linear' cyclic voltammetry. Staircase cyclic voltammetry is used for faradaic discharge-charge processes of Pb electrode and linear cyclic voltammetry are used for C_{dl} measurement.

4.4.1 Staircase cyclic voltammetry

In CV, potential is scanned either from negative to positive potentials or vice-versa with very small potential step after specific time interval added or subtracted for positive or negative scan direction respectively. Potential sweep and its current response of typical CV for discharge and charge of Pb with 3 reproducible scans at 5 mV/s showing oxidation peak in positive potential region and reduction peak in negative potential region is shown in Figure 26a, b. The potential scan rate, (ν) can be increased or decreased which results in faster or slower voltametric cycling. For

faradaic processes, the linear variation peak current with square root of scan rate is given by Randles-Sevcik equation

$$i_p = 0.446nFAC^0 \left(\frac{nNvD^0}{RT} \right)^{1/2}, \quad \text{Equation 58}$$

where, i_p is peak current (A), C^0 is bulk concentration of electroactive species (mol cm^{-3}), D^0 is diffusion coefficient of electroactive species ($\text{cm}^2 \text{s}^{-1}$), R is universal gas constant ($\text{J K}^{-1} \text{mol}^{-1}$), T is temperature (K).

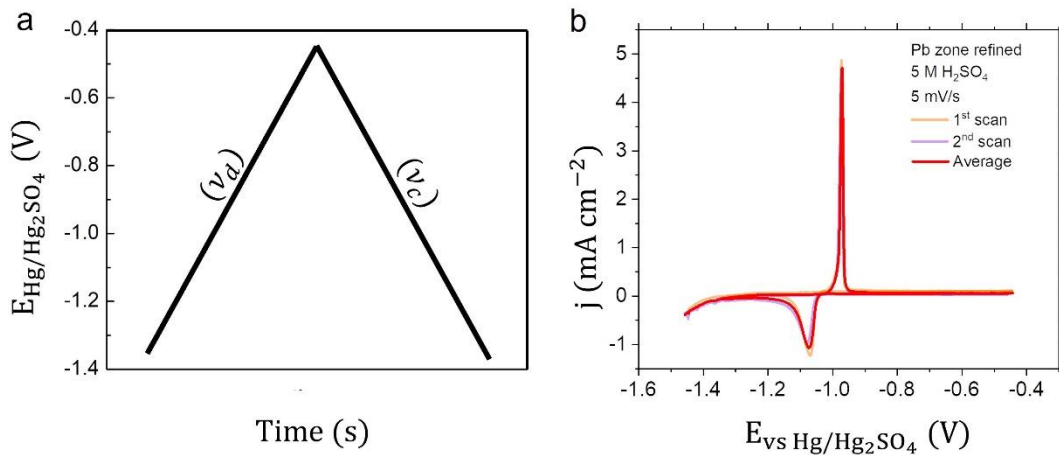


Figure 26. (a) Cyclic potential scan. (b) current response of CV.

Staircase CV is used for faradaic processes such as oxidation and reduction since capacitive current is not recorded. The current measurement can be done at various moments in duration of potential step which is given by α . For staircase waveform, the current transient is seen at each potential step and current is usually measured at $\alpha = 0.5$ i.e., at half or at $\alpha = 1$ i.e., at the end of total duration of potential step as shown in Figure 27b. Signal to noise ratio is much better when current is recorded at $\alpha = 1$ because of longer duration of potential step.

4.4.2 Linear cyclic voltammetry

As mentioned in section 2.3, a double layer capacitance measured in 5M H_2SO_4 is used as a metric for surface area after electropolishing of Pb so that surface area is consistent for all experiments with acceptable standard deviation of 5% in C_{dl} values. In linear sweep waveform procedure, current measurement is taken throughout the potential sweep as shown in Figure 27b. It is ideal for measuring capacitive current contributions of electrode. Scan rate influences double layer formation at electrode-electrolyte interface. Fast scan rate creates smaller double layer region resulting in high current response and opposite behavior is seen for slow scan rates. Therefore, in this work linear CV is used to collect current vs potential plot response which is then used to calculate C_{dl} . The difference in current vs time plots of both staircase and linear CV are shown in Figure 27a, b.

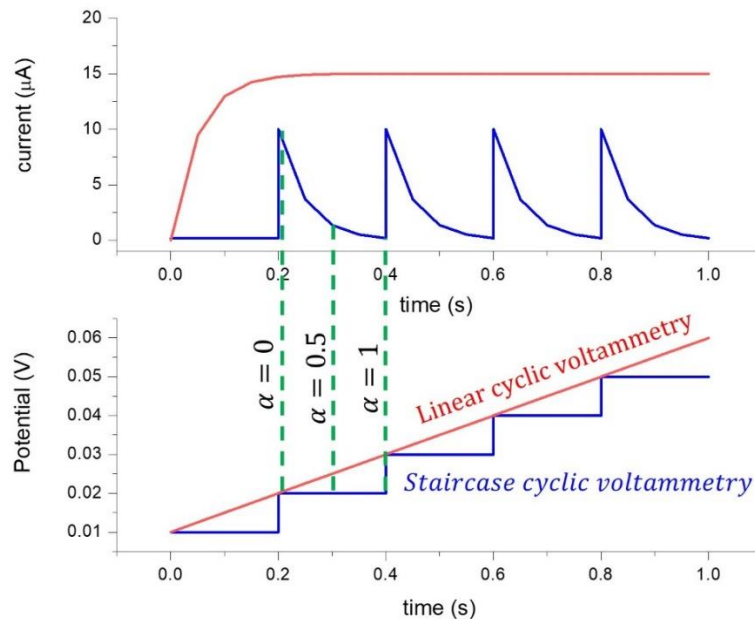


Figure 27. (a) Current vs time response (not to scale) (b) potential step duration for current measurement for linear (red) and staircase CV (blue).

4.4.3 Theory of Double Layer Capacitance

Solid-liquid interface of electrochemical reactions is of utmost importance since almost all electrochemical reactions happen at the interface. Non-faradaic processes at electrode-solution interface results in double layer formation because of opposite ionic charges on electrode and solution sides. The interface can be firstly considered as a parallel plate capacitor with capacitance give as

$$C = \frac{q}{E}, \quad \text{Equation 59}$$

where, C is capacitance (Coulombs), q is stored charge in capacitor and E is potential across capacitor plates. Helmholtz proposed the parallel plate capacitor model and prosed that capacitance depends on the distance between the two plates (118). In Helmholtz model this distance depends on ionic radius of the ions adsorbed at the electrode surface. The capacitance per unit area according to this model is known as Helmholtz capacitance (C_H) is given by

$$C_H = \frac{\varepsilon \varepsilon_0}{d}, \quad \text{Equation 60}$$

where, ε is the dielectric constant of electrolyte, ε_0 is the permittivity of free space and d is the separation distance between capacitor plates. The capacitance according to Helmholtz model is constant for the double layer. Although, variation in C_{dl} is seen experimentally with changing electrolyte concentration. Therefore, Helmholtz model is insufficient to describe effect of concentration in C_{dl} and it is true for concentrated electrolyte system. In Gouy-Chapman theory, the ionic concentration accumulated near charged electrode surface in dilute solutions considers Boltzmann's distribution and suggests that C_{dl} results from ionic charges

in the electrolyte at a distance from electrode and not only from charges near surface. Therefore, double layer extends further from electrode surface due to diffused layer of charges in dilute solution. The Gouy-Chapman capacitance as a function of potential drop in diffused layer is given as

$$C_{GC} = \frac{\varepsilon \varepsilon_0}{4\pi L_D} \cosh\left(\frac{zF\phi_M}{RT}\right), \quad \text{Equation 61}$$

where, L_D is Debye length, z is charge of ion, F is Faraday constant, ϕ_M is metal electrode potential. Debye length gives the thickness of double layer and is given by

$$L_D = \left(\frac{\varepsilon \varepsilon_0 RT}{2(zF)^2 C_0}\right)^{1/2}, \quad \text{Equation 62}$$

where, C_0 is the bulk concentration of the solution. In Practical systems, C_{dl} has contributions from simultaneous existence of Helmholtz and Gouy-Chapman models and C_{GC} as proposed by Stern (96, 97) and the total C_{dl} is given as

$$\frac{1}{C_{dl}} = \frac{1}{C_H} + \frac{1}{C_{GC}}. \quad \text{Equation 63}$$

In $\text{Pb}/\text{H}_2\text{SO}_4$ system as well the experimental C_{dl} varies with H_2SO_4 concentration. The double layer region thickness depends on temperature of the electrode-solution system (98, 99). A seven-step method for obtaining reliable and accurate double layer scans for experimental determination of C_{dl} using cyclic voltammetry is implemented for accuracy of C_{dl} values (122). Experimental C_{dl} of $\text{Pb}/\text{H}_2\text{SO}_4$ interface at temperatures from -20°C to 55°C is observed in this work as shown in result in chapter 6.

4.4.4 Discharge and Charge Capacity using I-V curves

The I-V curve recorded by Potentiostat of Pb discharge and charge peaks can be used to calculate the discharge and charge capacity by integrating area under the curve and dividing it by potentials scan rate used for discharge-charge CV scan. The equation for capacity can be given as

$$Q = \frac{\int J \cdot dE}{\nu}, \quad \text{Equation 64}$$

where, Q represent discharge or charge capacity ($mC\ cm^{-2}$), J is current density ($A\ cm^{-2}$) calculated by dividing current by $0.283\ cm^2$ area of Pb surface of 6 mm diameter, dE is change in potential (V) and ν is potential scan rate ($V\ s^{-1}$). The calculated discharge capacities are used to study current-discharge capacity relationship for Peukert analysis and kinetic charge acceptance at temperatures from $-20^{\circ} C$ to $55^{\circ} C$.

4.4.5 Electrochemical Thickness of $PbSO_4$ layer

Faraday's law of electrolysis gives mass of Pb dissolved proportional to charge obtained from discharge peak. Dissolved Pb^{2+} ions then react with HSO_4^- ions and precipitate as $PbSO_4$ on Pb surface. Therefore, electrochemical thickness of $PbSO_4$ layer can be calculated from discharge capacity as

$$l_{PbSO_4} = \frac{M_{PbSO_4} \times Q_d}{n \times \rho_{PbSO_4} \times F'} \quad \text{Equation 65}$$

where, l_{PbSO_4} is electrochemical thickness of $PbSO_4$ layer, M_{PbSO_4} is the molar mass of $PbSO_4$, Q_d is discharge capacity and ρ_{PbSO_4} is the density of $PbSO_4$. Here number of electrons are taken as $n = 2$ because of Pb to $PbSO_4$ reaction shown in Equation

2. $PbSO_4$ thickness calculated from electrochemical data and average thickness verified by FIB-SEM are compared in chapter 6 at all chosen temperatures to study the effect of temperature on $PbSO_4$ thickness.

4.5 Imaging Techniques

Temperature is one of the key parameters in performance of all types of batteries and Lead-acid battery is no exception. Lead-acid loose capacity at extreme low or high temperatures due to sluggish kinetics at low temperature or high gassing and water loss at high temperature. Pb and PbO_2 electrodes discharge and charge kinetics is significantly influenced by temperature. In this work, $PbSO_4$ morphology is observed on Lead samples discharge in 5 M H_2SO_4 at 6 different temperatures ranging from $-20^{\circ}C$ to $55^{\circ}C$ by conductive AFM-TUNA and SEM. Actual $PbSO_4$ thickness is measured from a cross section of discharge Pb disk using FIB-SEM.

4.5.1 Atomic Force Microscopy

Pb sample with 100% DoD is imaged using PeakForce TUNA AFM mode in Dimension Icon AFM instrument from Bruker. TUNA stands for tunneling current between sample surface and conductive AFM tip. The PFTUNA tip used for this mode is silicon nitride tip coated with conductive coating scans the sample surface in PeakForce tapping mode while measuring the tunneling current between samples and tip (123). A large resistance $100\text{ M}\Omega$ is connected to sample holder so that low tunneling current in the range of fA to μA can be detected. A PFTUNA module with high current sensitivity and low noise current amplification is used for TUNA

current image. The sample and the tip are electrically connected with an external voltage source which is used to apply a DC voltage bias between tip and sample to control tunneling current. The schematic of AFM TUNA operation is shown in Figure 28. The PeakForce setpoint, amplitude and frequency of scanning is used to control the force exerted by tip while scanning the surface. The sulphate layer covering Pb surface contains cracks and grain boundaries through which electrons tunnel to the tip. A height image of sample topography and TUNA image of the same area is captured. TUNA image clearly shows the conductive areas in the passivated Pb surface which is important for charging process of the electrode. TUNA images with height image shows changes in $PbSO_4$ layer electron conductive area and morphology development when Pb is discharged at various temperature.

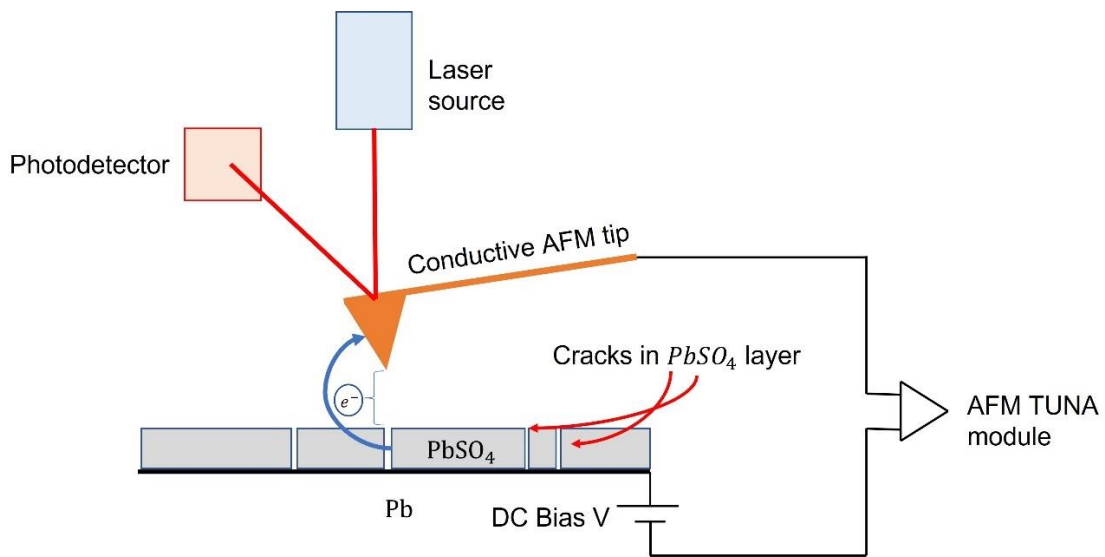


Figure 28. AFM TUNA Schematic.

4.5.2 AFM Image Processing

The AFM images captured are processed in an open-source software Gwyddion. The AFM images may be tilted because the sample surface may have a tilt. Therefore, the AFM images is tilt correlated then a background removal is done using a polynomial function of degree 2. A row alignment is performed to clear up the horizontal lines in the image that may be crated when tip scans the sample surface. Then a scan removal is done to get rid of scars in the image created due to noise or scanning elevated areas on sample surface.

4.5.3 Focused Ion Beam Scanning Electron Microscopy (FIB-SEM)

A Zeiss 1540XB FIB-SEM dual beam system with FIB gun using Gallium ions for milling and an electron gun for imaging is used. The FIB and scanning electron guns are at an angle of 54° . At the beginning, sample is perpendicular to scanning electron gun. It is then tilted 54° so that it is perpendicular to FIB gun and at 36° to SEM gun. A fine trapezium shape is chosen for ion beam milling with $15\ \mu\text{m}$ side showing cross-section area and 30° slope milled area joining the other side of trapezium. The milling is done in two steps, first is coarse milling at higher current of 1.5 nA used for milling the trapezium and second, fine milling at lower current of 400 pA for smoothening the cross-section area so that thickness of PbSO_4 can be clearly seen. The SEM image of the cross section must be tilt corrected for 30° since SEM gun is at 36° angle. The arrangement of both beam gun and sample is shown in the schematic in Figure 29.

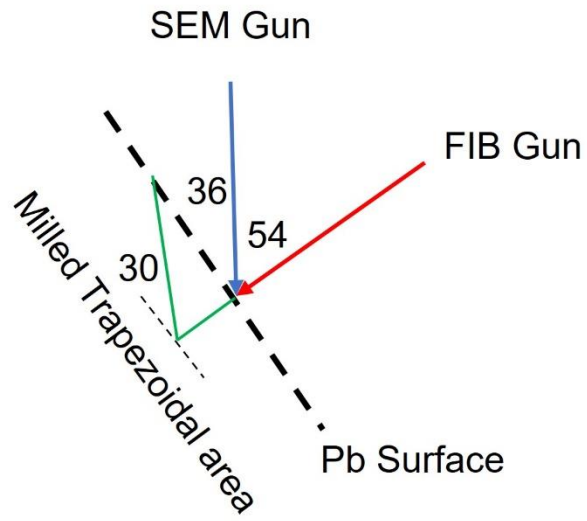


Figure 29. FIB-SEM and Pb sample alignment.

Chapter 5

Experimental Setups and Procedures

The induction heating experimental setup and procedures for graphene synthesis are explained in first section of chapter 5. The later section of this chapter focuses on electrochemical setup for Pb electrode study and experimental procedure followed for Pb electropolishing and electrochemical testing using NOVA 1.8 software compatible with Autolab Potentiostat. Sample preparation and storage for AFM and FIB-SEM is also included in this chapter.

5.1. Experimental Setup for Graphene Synthesis

A surface treated and annealed 99.9% pure Cu samples as substrate and carbon black powder milled for 2 hr in a high energy ball mill is used for the experiments. A Cu die of 10 mm diameter consisting of two Cu punch blocks and a sleeve is fabricated as shown in Figure 30. The die is packed with Cu substrate at the bottom and carbon powder poured on top. The packed die is then pressed at ~ 7 Mpa pressure in a Die press for 1 min as shown in Figure 31a. The pressed die is then placed in a quartz assembly purged with Ar gas to avoid oxidation of Cu substrate. The setup is then placed in the coils of induction heating furnace with a thermocouple introduced in the die close to Cu substrate to closely monitor temperature inside the die as shown in Figure 31b.

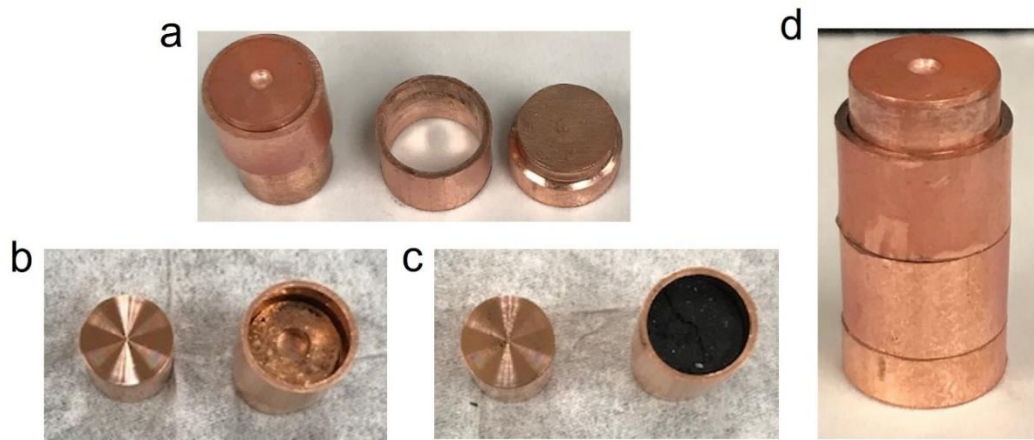


Figure 30. (a) Parts of Cu die. (b, c) Cu substrate and carbon in the die. (d) assembled die.

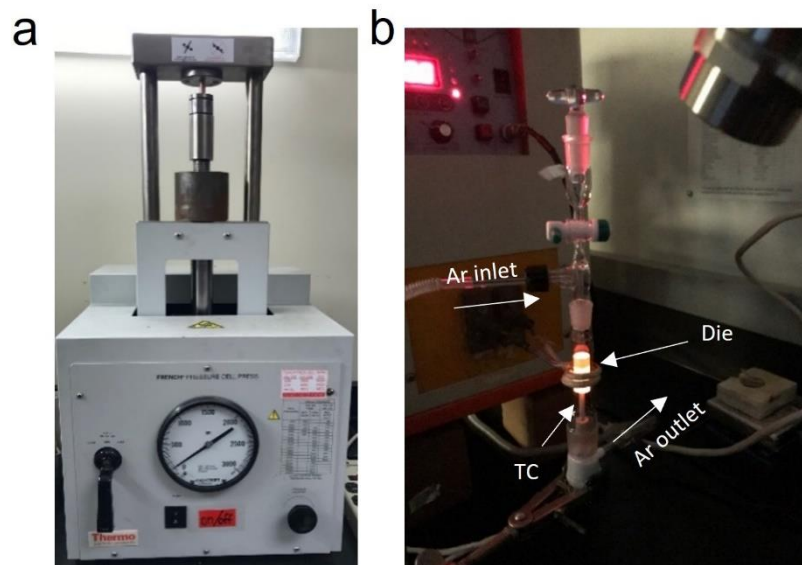


Figure 31. (a) Die press (b) Induction heating setup.

5.1.1 Experimental Procedure

Cu die is heated for 30 min with 1 min temperature ramp from R.T to desired higher temperature. An IR temperature sensor controlled with PID controller is used to maintain the temperature precisely. Carbon is diffused in Cu surface at elevated temperatures. The experiment is conducted at 3 different temperatures of

600°C, 800°C and 950°C. The best results of graphene synthesized on Cu are obtained at temperature regime of 950°C for 30 min and 600°C for 10 min followed by cooling down to R.T in Ar atmosphere. After cooling down for 30 min, the Cu substrate is taken out and cleaned of with Ar jet. Graphene synthesized on Cu is detected using Raman spectroscopy and mapping. A scotch tape exfoliation is performed on graphene covered Cu for lifting the synthesized graphene from Cu substrate. The results of the experiments are discussed in Chapter 6.

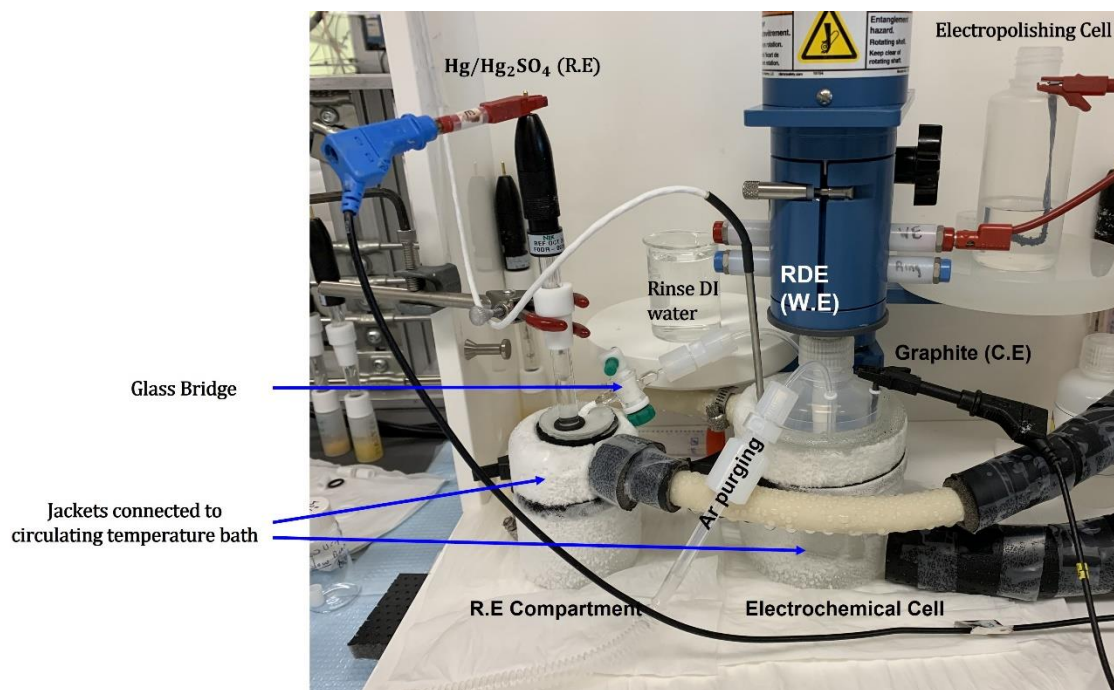


Figure 32. Electrochemical Setup.

5.2 Experimental setup of Lead electrode in H_2SO_4

5.2.1 Electrochemical cell

A three-electrode electrochemical cell made from fluoropolymer plastic with 6 mm Pb disk as attached to a rotating discs electrode from Pine research as

working electrode (W.E), highly porous graphite rod as counter electrode (C.E) and Hg/Hg_2SO_4 reference electrode (R.E) filled with saturated K_2SO_4 solution immersed in separate 5 M H_2SO_4 container which connected to the cell via glass bridge is used for electrochemical experiments. Separate compartment for R.E helps to avoid cross contamination of solution in electrochemical cell. The electrochemical cell setup is shown in Figure 32. H_2SO_4 solution is deaerated for 30 min by purging ultra-pure Ar for 30 min before experiments.

5.2.2 Experimental Procedure

Experimental procedure consists of 2 steps. First, is electrochemical polishing of Pb surface in galvanostatic mode followed by second step of cyclic voltammetry on Pb electrode in potentiostatic mode.

i. Electrochemical Polishing

Lead disk is cleaned by putting it in 0.1 M $HClO_4$ for ~5 min then taken out and rinsed thoroughly with DI water and extra water is absorbed by dabbing side of Pb disk on dry paper wipe. The disk is placed upside down on clean PE sheet and a U-cap is pushed on the disk after which a Teflon collet is pushed on the U-cap containing Pb disk. The collet is screwed on to RDE shaft with exposed Pb surface down. A 2 electrode electropolishing cell with Pb RDE as W.E and 5 mm wide 99.9999% Pb strip as C.E. Pb surface is first grain polished at 30 mA for 300 sec at 1000 rpm then the current is changed to 150 mA for 20 sec at 1000 rpm to obtain mirror polished Pb surface. Pb surface is rinsed in DI water and dried with strong Ar jet. Pictures and

SEM images of high-quality grain and mirror polished Pb surface with AFM images mirror polished Pb surface with scale bar of 20 nm is shown in Figure 33.

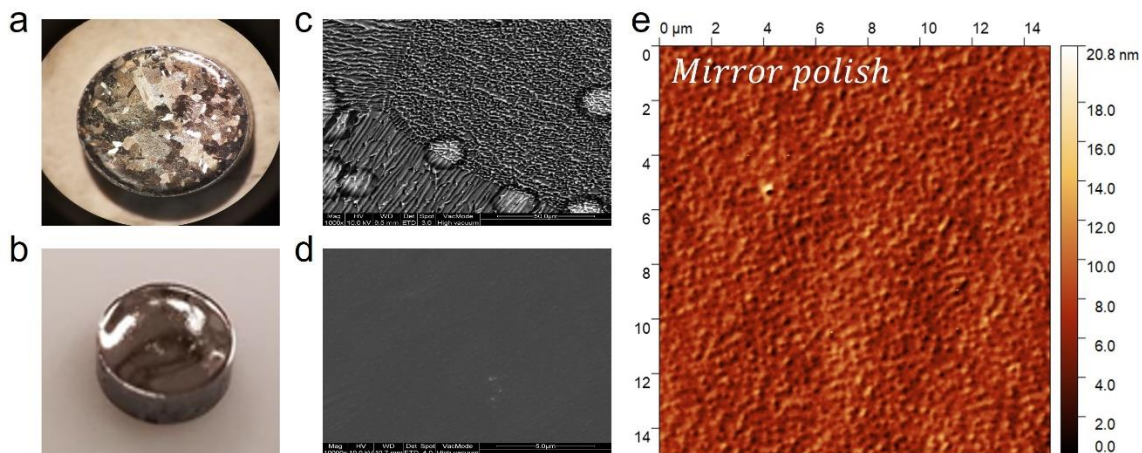


Figure 33. (a, b) Grain and mirror polished Pb pictures. (c, d) SEM images of same. (e) AFM image of mirror polished Pb surface.

ii. Cyclic Voltammetry on Pb surface

Pb electrode is polarized at -1.35 V after electropolishing, rinsing and drying and before introducing in 5 M H_2SO_4 to avoid sulfation before stating the CV. First, linear waveform CV between -1.25 V and -1.15 V with scan rates of 0.01, 0.02, 0.05, 0.1, 0.2, 0.5 and 1 V/s are performed for C_{dl} determination as shown in Figure 34b, c. The potential window for DL scans should be 100 to 200 mV long and must be before faradaic discharge potentials in CV as shown in Figure 34a. An asymmetric CV with discharge scan rates of 1000, 500, 100, 50, 10, 5, 1 and 0.5 mV/s from -1.35 V to -0.45 V back to -1.0 V and charge scan rate of 10 mV/s from -1.0 V to -1.45 V are used as shown in red and blue regions respectively in Figure 34d. Experiments are conducted at 6 different temperatures of $-20^{\circ}C$, $-5^{\circ}C$, $10^{\circ}C$, $25^{\circ}C$, $44^{\circ}C$ and $55^{\circ}C$. The temperature of electrochemical cell is controlled by liquid circulating jackets

maintained at desired temperature using PolyScience temperature control system. Cell is surrounded by 80% ethylene glycol and 20% water solution for low temperature experiments and with water at higher temperatures for uniform cooling and heating which is monitored using a temperature probe between cell and circulating jacket. The cell is sealed to reduce water evaporation at higher temperature and limit water condensation from atmosphere at colder temperatures as much as possible. Pb electrode introduced in 5 M H_2SO_4 is held polarized at -1.35 V for 10 min for attaining temperature equilibrium before starting CV procedure.

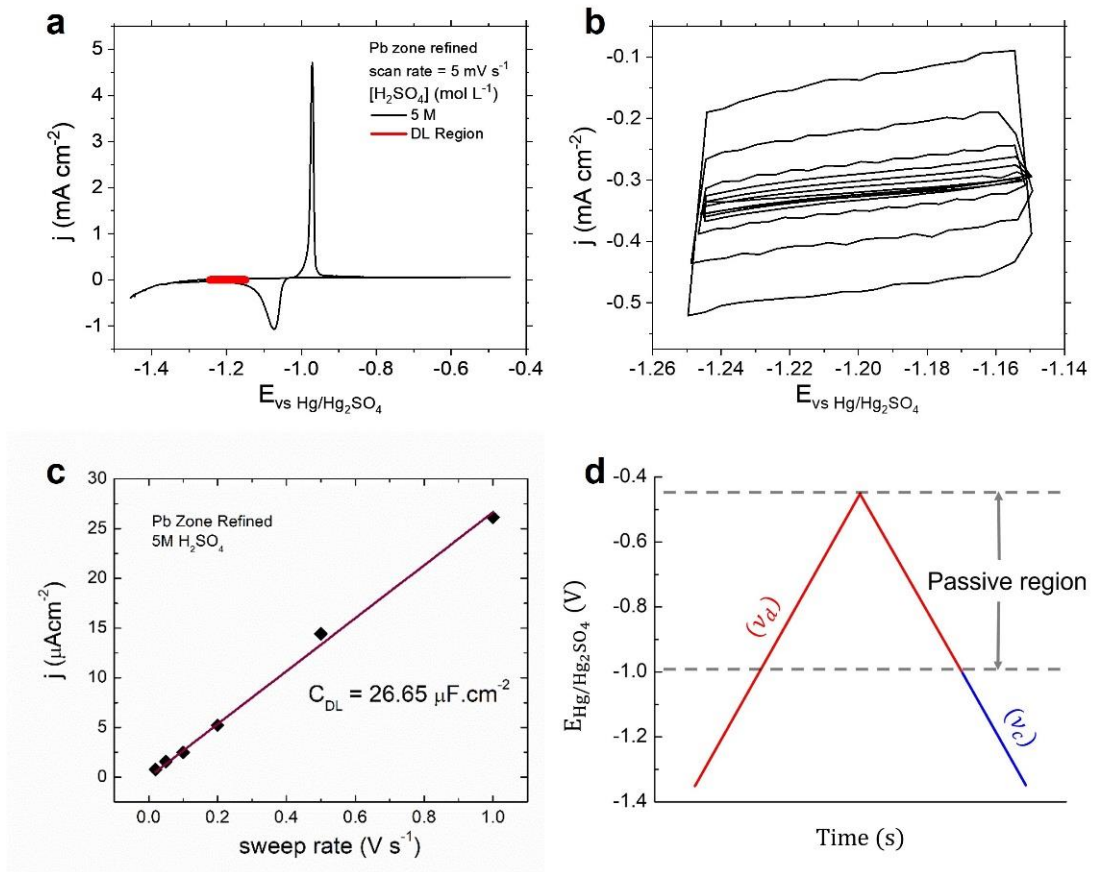


Figure 34. (a) DL potential window, (b)DL CV's (c) C_{dl} determination (d) Asymmetric Voltammetry potential scan rate.

5.2.3 Sample Preparation for Imaging

Pb samples discharged after only positive linear sweep is taken out of the cell and the H_2SO_4 on Pb surface is dried with Argonne jet. The sample is then taken out of RDE collet and stored in glass vial purged with Ar. Vial is stored in vacuum before AFM and FIB-SEM. This method is chosen to avoid dipping the discharged sample in water or alcohol which may dissolve $PbSO_4$ and change its morphology. The discharge Pb samples stored in vacuum are quickly transferred to sputter coating system loading chamber for ~ 200 nm Au coating before FIB-SEM. Au coating is essential for protection of $PbSO_4$ layer morphology and thickness from focused ion beam during ion milling.

Chapter 6

Results And Discussion

This chapter contains the results of graphene synthesis on copper surface in the first section with Raman spectra of graphene formed at 600°C , 800°C and 900°C for 30 min and temperature reduced to 600°C for 10 minutes after 900°C . Raman maps of Cu surface after graphene formation on top show presence of high intensity 2D peak which confirms graphene synthesized using proposed solid-state method. The later parts include results from electrochemical investigation of Pb electrode in 5 M H_2SO_4 , Peukert relationship, KCA analysis. PbSO_4 morphological changes are studied using FIB-SEM and AFM include thickness and conductive area of PbSO_4 on Pb.

6.1 Characterization of Synthesized Graphene

Copper surface treatment mentioned in experimental methods has seen to be effective in growing bilayer graphene. Graphene nucleation is related to crystallographic changes in Cu annealed for 1 hr and 10 hr at 1000°C . Most of Cu surface is covered with graphene when 10hr annealed Cu surface is used as it develops terraces in (100) crystallographic direction in Cu grains which are responsible for graphene formation. Variation in temperature used for carbon black in contact with Cu for diffusion and resurfacing of carbon as graphene show variation in resulting quality and quantity of graphene.

6.1.1 Raman Spectroscopy and Mapping of Graphene on Copper

Figure 35a shows Raman spectra of graphitic carbon produced at 600°C , 800°C and 950°C for 30 minutes and Figure 35b shows shift in 2D peak with temperature. Lower 2D peak and higher D and G peak intensities for lower synthesis temperature of 600°C suggest that graphitic carbon formed on Cu surface has higher defects and its Raman spectra is same as 2 hr milled carbon black. Therefore, at 600°C diffusion of carbon is not sufficient and graphitic structures on Cu are mostly because of carbon-Cu surface interactions. As the synthesis temperature is increased, the D and G peaks become smaller and 2D peak increases in intensity proving graphene formation on Cu with lower defects.

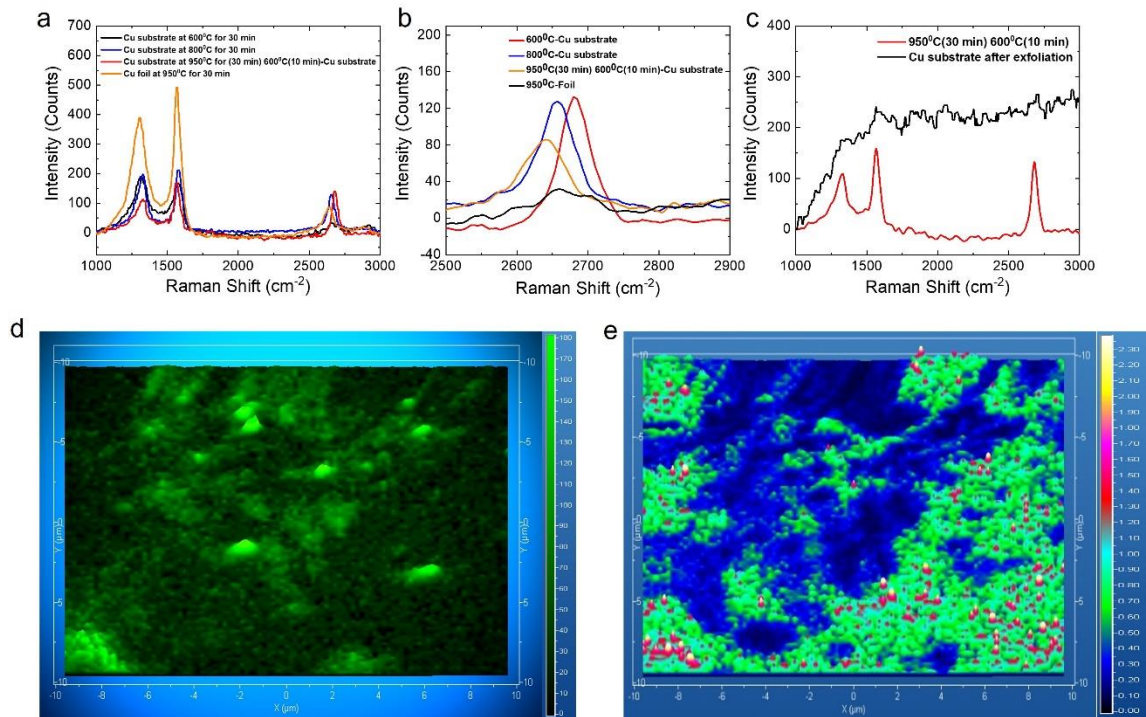


Figure 35. (a) Raman spectra of graphitic carbon at various temperatures, (b) Shift in Raman spectra, (c) Raman Spectra before and after exfoliation, (d) 2D peak Raman map, (e) I_{2D}/I_G map.

The highest 2D peak and lowest D peak intensities are obtained at 950⁰ C for 30 min followed by 600⁰C for 10 min as shown by red spectrum in Figure 35a with I_{2D}/I_G ratio close to 0.9 that indicates bilayer graphene. Temperature of 950⁰C promotes carbon diffusion and 600⁰C in later step promotes carbon resurfacing. The Raman map focused on 2D peak in Figure 35d shows graphene coverage on Cu and map created by taking ratio of 2D peak map and G peak map in Figure 35e indicates number of graphene layers on Cu. The Cu surface with graphene on top was subjected to scotch tape exfoliation and graphene was successfully lifted from Cu surface as seen by absence of Raman peaks in spectrum in Figure 35c from same Cu surface.

6.1.2 SEM, EDX and HRTEM Imaging of Graphene on Copper

The graphene synthesized by the method described in the experimental section was further analyzed by SEM combined with Energy Dispersive X-ray Spectroscopy (EDS) and HRTEM imaging techniques. Figure 36a shows the SEM image and EDS map of graphene (pink) on copper (blue). Graphene is detected along the terraces of copper surface. Further imaging of various spots show similar results in Figure 36b and c with graphene indicated by arrows in the SEM images. Last image in Figure 36c shows a thin lamella taken out of the copper substrate for TEM imaging. From HRTEM images, highly oriented graphene was observed on copper grains and absence of graphene along grain boundaries as shown in Figure 36d. The grain boundary is indicated by dashed yellow line. This supports the notion that graphene preferentially produced at copper terraces. The HRTEM

images in Figure 36e shows the hexagonal structure of carbon atoms in synthesized graphene along (111) copper planes.

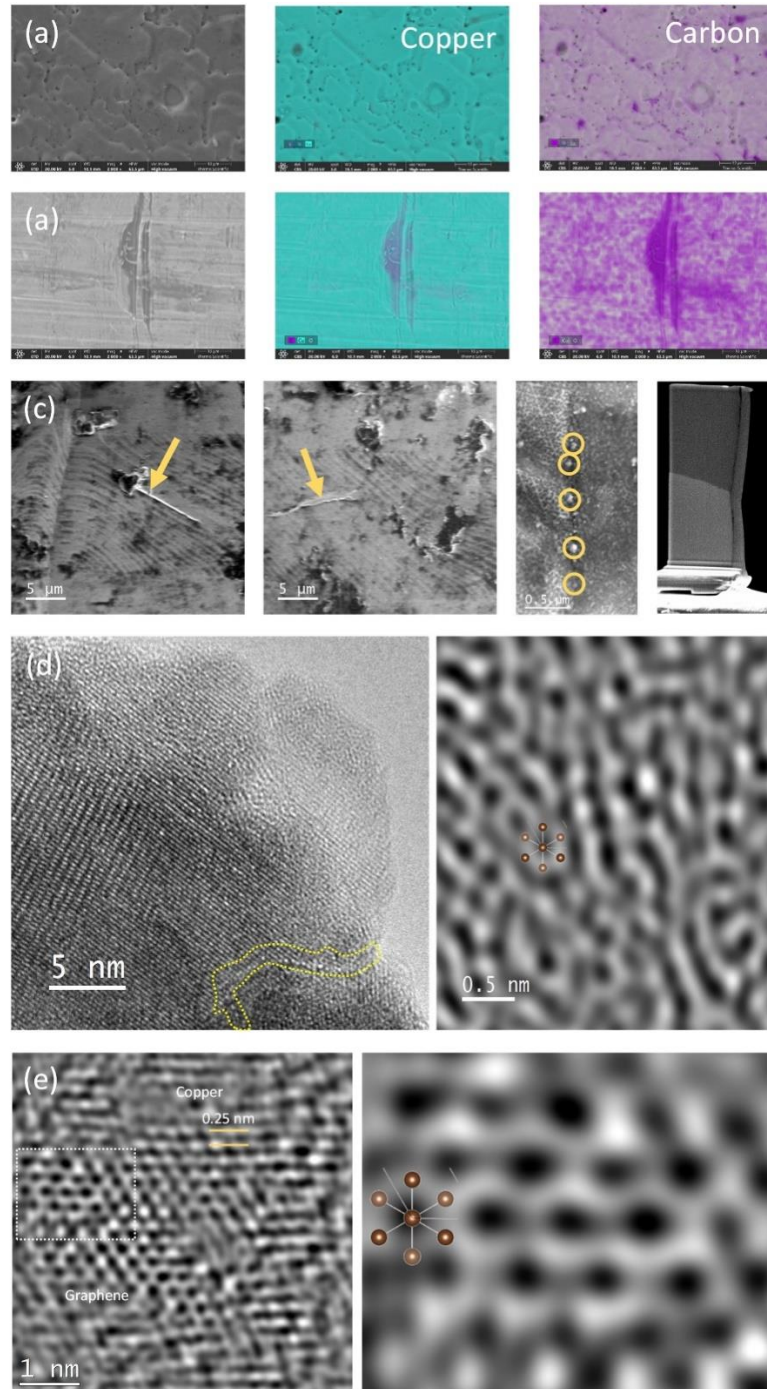


Figure 36. (a, b) SEM and EDS images, (c) SEM images of graphene across Cu terraces and FIB-SEM lamella, (d, e) HRTEM images of highly oriented hexagonal graphene on Cu.

6.2 Double Layer Capacitance of Pb Surface

Capacitive current from non-faradaic processes at Pb and H_2SO_4 interface from linear CV at negative potentials before discharge peak is used for C_{dl} determination. Since capacitive current results from double layer acting as parallel plate capacitor due to charge separation at the electrode-solution interface, capacitance is used for monitoring electropolished Pb surface before conducting electrochemical experiments at chosen temperatures. C_{dl} from linear CV procedure is validated by experimental determination C_{dl} using EIS and C_{dl} from both methods for electropolished Pb in 5 M H_2SO_4 are in excellent agreement as shown in Figure 37. The C_{dl} reveals influence of temperature as the capacitive charge and diffused double layer structure changes with temperature. C_{dl} is calculated by taking mean of C_{dl} values of multiple Pb samples after electropolishing for each temperature as shown in Figure 38a. The average C_{dl} is plotted vs temperature and an increase in C_{dl} with temperature is observed due to higher kinetics and increased capacitive current as shown in Figure 38b with an exception at $55^{\circ}C$.

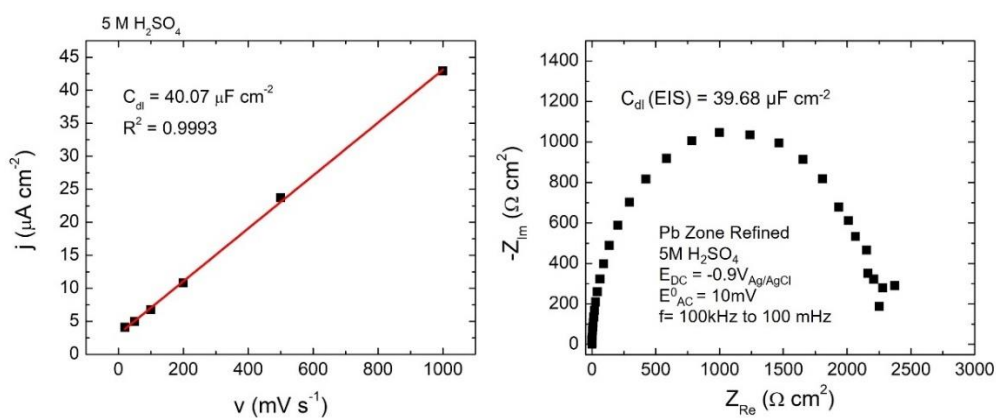


Figure 37. Validation of C_{dl} using EIS and CV.

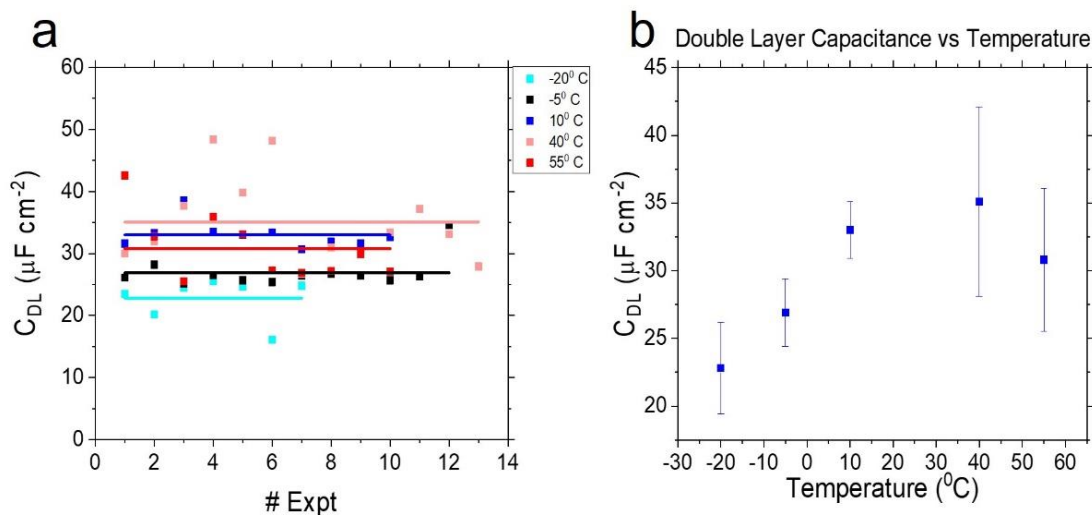


Figure 38. (a) Average C_{dl} , (b) C_{dl} vs temperature.

6.3 Cyclic Voltammetry Reproducibility

The discharge and charge CV scans performed in 5 M H_2SO_4 at all 6 temperatures are average of at least 3 scans for each scan rate using freshly prepared and electropolished Pb disk. This is done to ensure reproducibility of CV data with standard deviation of about 5% for multiple CV scans. Good reproducibility of CV scans is achieved by careful monitoring electropolished surface area using C_{dl} , two individual discharge and charge scans with 5 mV/s scan rate at -5°C with their average curves is shown in Figure 39. The discharge and charge capacities used in Peukert and KCA analysis are calculated from averaged CV scans. CV with standard deviation of about 5% is considered as data with good reproducibility. Abnormalities in discharge and charge peak may arise from lose U-cap, bad contact at electrode, etc. Freshly electropolished Pb surface polarized at -1.35 V in 5 M H_2SO_4 maintained at specific temperature must be allowed time for attaining thermal equilibrium between Pb surface and electrolyte. It was observed

that CVs performed right after introducing Pb in 5 M H_2SO_4 were inconsistent and closer to room temperature CVs. The effect of 5 min wait time added before starting CV procedure is evident in Figure 40 showing 1000 mV/s scans for 10°C and 55°C. The red scans are without wait time which show peak resemblance to R.T. peaks indicated by dashed green line. Faster scan rates are severely affected since CV is completed before Pb surface achieves same temperature as that of electrolyte.

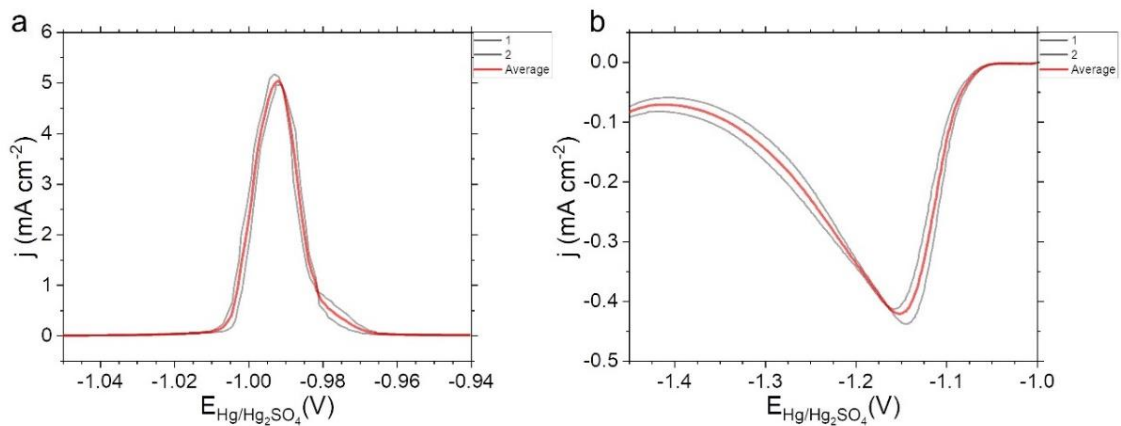


Figure 39. Reproducible discharge and charge scans (black) and averaged scan (red) with 10 mV/s scan rate at $-5^{\circ}C$ in 5 M H_2SO_4 .

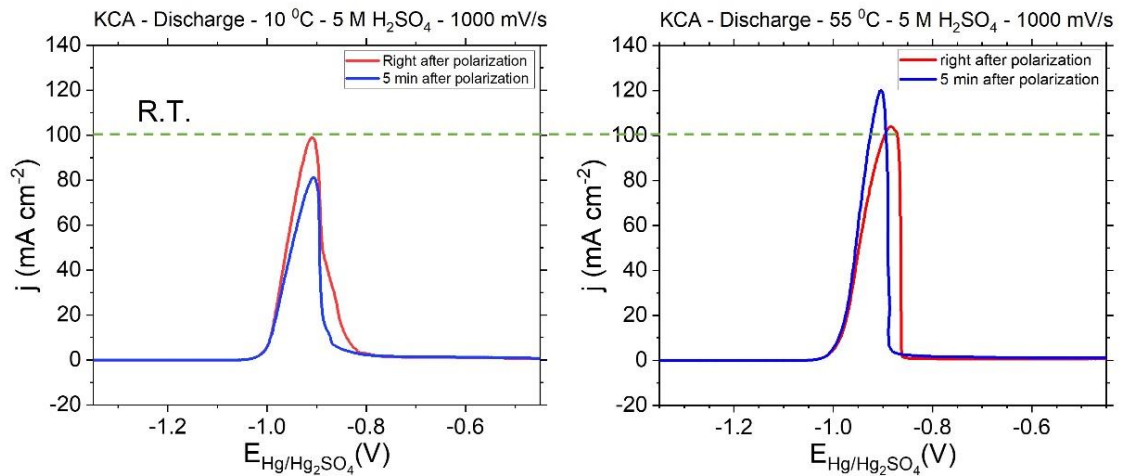


Figure 40. Wait time required for temperature equilibration between electrolyte and Pb surface.

6.4 Effect of Potential Scan Rate

Electropolished Pb surface subjected to cyclic voltammetry with variation in potential scan rate can discharge or charge the Pb faster or slower and the resulting morphological changes in $PbSO_4$ can be studied. Scan rate affects the capacity extracted from the electrode and it has been established that at faster scan rate, the discharge capacity is lower than slow Pb discharged with slow scan rates. The focus of this work is on understanding $PbSO_4$ layer thickness and particle size with variation in discharge rates and its relation to charge-current relationship given by Peukert law and kinetic charge acceptance. Therefore, it is crucial to understand the changes in $PbSO_4$ morphology with discharge scan rate. The increase in discharge capacity and $PbSO_4$ thickness calculated using Faraday's law from experimental data with decreasing potential scan rate is shown in Figure 41c. SEM imaging on Pb surface discharge at 100% DoD using various potential scan rates shows that the $PbSO_4$ particle size is also dependent on discharge rate. The SEM images in Figure 42 of Pb surface discharged at scan rates from 500 mV/s to 0.05 mV/s show smaller $PbSO_4$ particle size at faster discharge and bigger particles at slower discharge rates.

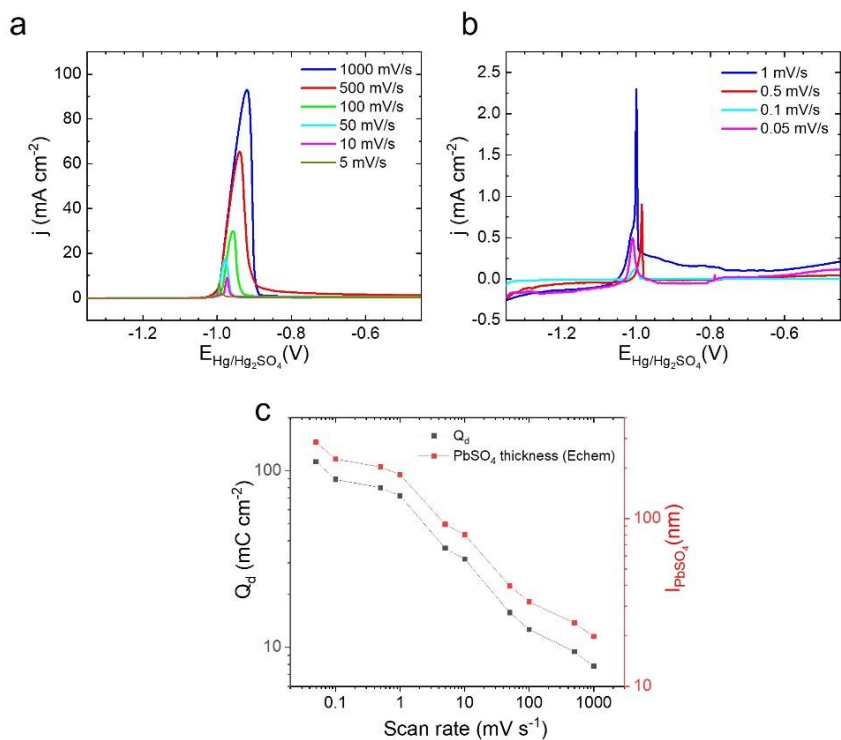


Figure 41. (a, b) Discharge scans, capacity at 22^oC and (c) $PbSO_4$ thickness vs potential scan rate.

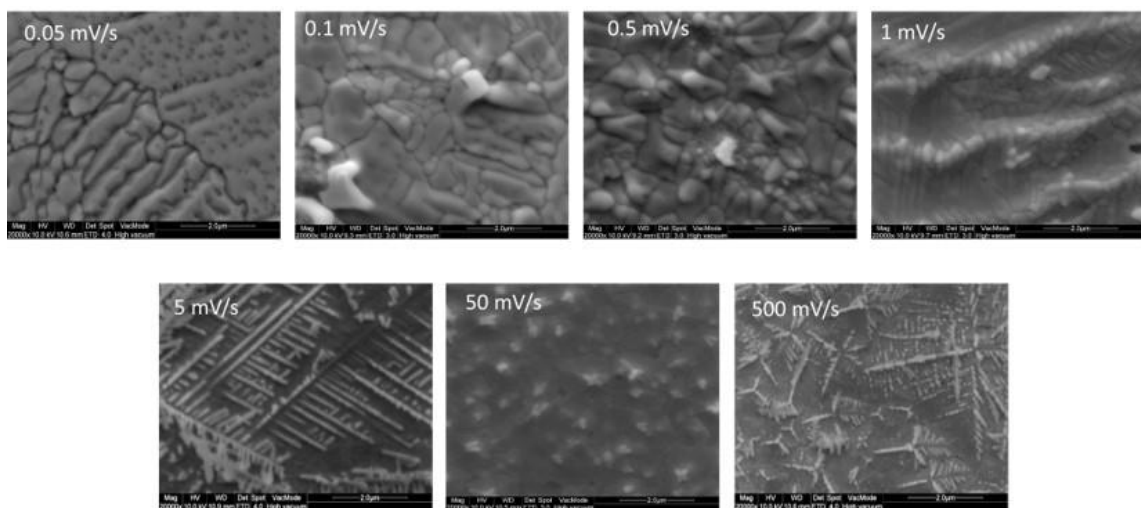


Figure 42. SEM images of discharged Pb surface using various discharge scan rates.

6.5 Effect of Temperature on Peukert Relationship

6.5.1 Correlation of Peukert Relationship for Discharge under Galvanostatic and Potentiostatic conditions

Peukert law is most often used for defining current-charge relation of batteries in galvanostatic mode as mentioned section 3.1.1. Since a potentiostatic mode is used to study discharge and charge processes in this work, it is important to cross check and validate the Peukert analysis of experimental data from both modes. Therefore, the intrinsic discharge capacity calculated from CV data and Peukert relation for potentiostatic mode given by equation 26 using peak current potential in CV for capacity integration. Peak currents from CV peaks and time calculated accordingly is used for constant current discharge for potentiostatic and galvanostatic data comparison. The intrinsic discharge predicted from CV in potentiostatic mode and capacity from constant current discharge experimental data show excellent agreement.

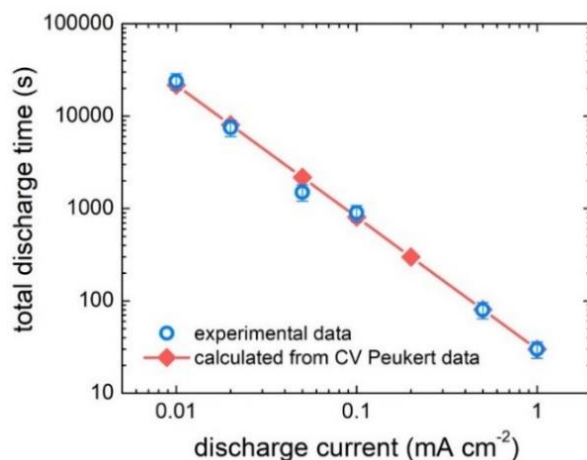


Figure 43. Same discharge under potentiostatic and galvanostatic mode.

Figure 43 shows the discharge capacity agreement of potentiostatic and galvanostatic discharge conditions. Experiments for the comparing discharge under potential where intrinsic discharge capacity is $30 \text{ (mC cm}^{-2}\text{)}$ and under current control where cutoff voltage of -0.9 V was chosen and $5 \text{ M H}_2\text{SO}_4$ as electrolyte was used. Therefore, it can be said that the Peukert relationship holds true for discharge process executed under either potential or current control methods. This correlation is extremely useful to correlate data from laboratory testing conditions to battery operated in practical application conditions.

6.5.2 Variation in Discharge and Charge Capacities with Temperature

The reactions happening at Pb electrode are influenced by changes in temperature as with almost all reactions. Arrhenius pointed out a relationship between reaction rate and temperature given by

$$k = A e^{-\frac{E_A}{RT}}, \quad \text{Equation 66}$$

where, k is reaction rate, A is frequency factor, E_A is activation energy. Increase in temperature increases kinetics of reactions and it is generally said that for every 10^0 C the rate of reaction is doubled.

For the experiments carried out for studying discharge and charge processes of Pb electrode with temperature, the electrochemical cell is maintained at desired temperature before introducing Pb electrode and asymmetric CV procedure is used. The discharge process evaluated by discharge peaks in Figure 44 during positive potential scan show increased peak current with increase in temperature from

–20° C to 55° C at faster discharge of 1000 mV/s than in slower discharge of 0.5 mV/s. Although the electrochemical cell was sealed, the water loss at 40° C is high and even worse at 55° C. Therefore, increase in concentration is a significant factor lowering discharge at elevated temperatures especially at slower discharge rates. $PbSO_4$ morphology is expected to change with temperature and discharge scan rate and particle size and thickness of passivation layer is related to discharge capacity. $PbSO_4$ morphology is investigated using AFM and FIB-SEM in next section.

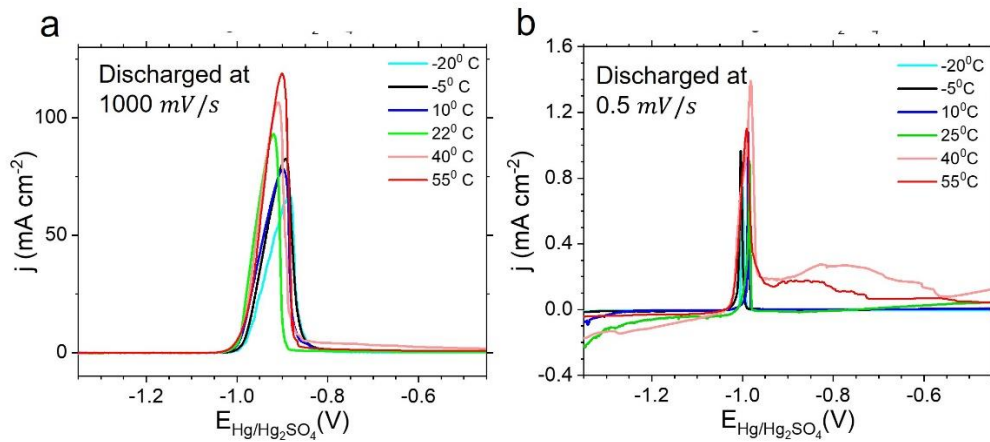


Figure 44. Discharge scans at (a) 1000 mV/s (b) 0.5 mV/s.

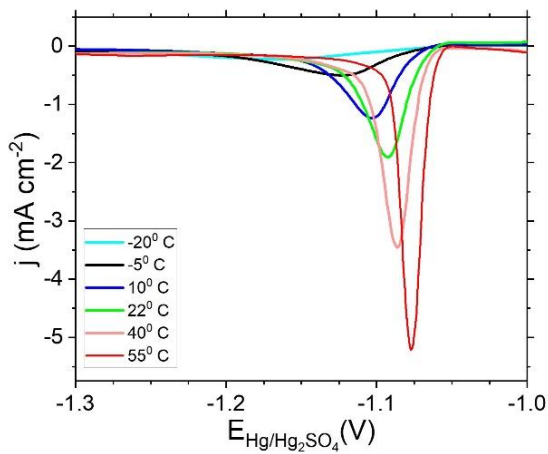


Figure 45. Charge scans with 1000 mV/s at all temperatures.

The effect of temperature on discharge is relatively smaller than compared to its effect on charge process. For 1000 mV/s charge scans, the peak current shows 5-fold increase with increase in temperature from $-20^{\circ}C$ to $55^{\circ}C$. Figure 45 shows charge scans at all 6 temperatures.

6.5.3 Variation in Peukert Coefficient with Temperature

Peukert analysis of discharge process with all scan rates mentioned in experimental procedure at these 6 temperatures shows that the Peukert coefficient, $\langle n \rangle$ is sensitive to temperature lower than room temperature as shown in Table 3 below. It decreases significantly from 1.38 for R.T to 1.087 for $-20^{\circ}C$. On the other hand, Peukert coefficient at higher temperatures show very little change, at $40^{\circ}C$ it slightly increases to 1.39 and falls to 1.34 at $55^{\circ}C$. This change in Peukert relationship with temperature is shown in Figure 46a. The intrinsic discharge capacity calculated from Peukert analysis also follows the same trends as $\langle n \rangle$ showing almost 4 times increase from $-20^{\circ}C$ to $55^{\circ}C$. This effect is seen in current vs charge plots shown in Figure 47. $\langle n \rangle$ is given by the slope of line fit in Figure 46a for potentiostatic mode but the values in Table 3 are converted to galvanostatic format since it is commonly used.

Solubility of Pb^{2+} ions also change with temperature of 5 M H_2SO_4 electrolyte which affects discharge capacity as shown in derivation of Peukert law in section 3.1.2. Figure 46b shows Pb^{2+} solubility is measured using ICP-MS at all temperatures used in this work. Higher Pb^{2+} ion solubility is seen with higher temperatures as expected. But the limited increase in discharge capacity at higher

temperatures may occur due to increased $PbSO_4$ precipitation kinetics balancing the increased Pb^{2+} ion solubility. The extended Peukert relationship derived in chapter 3 is used to fit the data. The β/α ratio represents influence of sulphate ion concentration gradient which is smaller at high temperatures showing Peukert coefficient is closer to 1.5. Higher Peukert coefficient at higher temperature indicates higher internal resistance that also contributes to loss in discharge performance of Pb electrode.

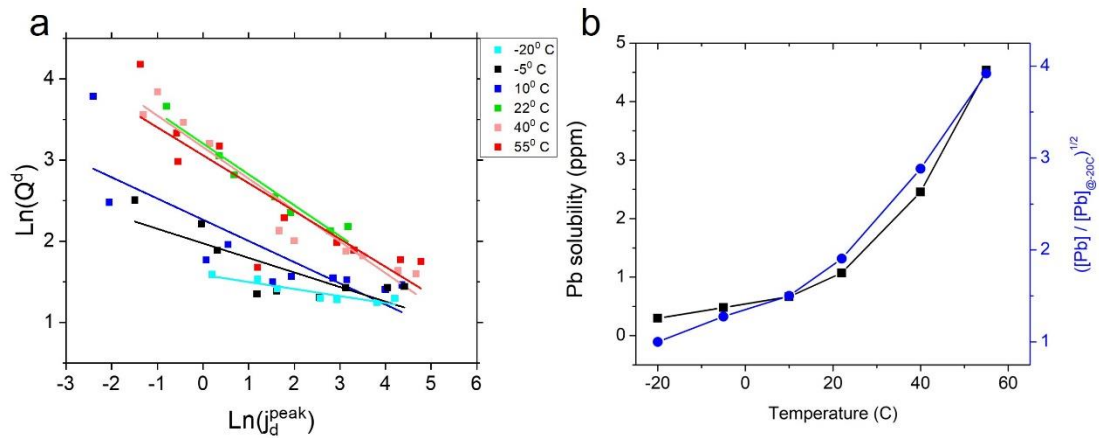


Figure 46. (a) Peukert relationship (b) Change in Pb^{2+} solubility with temperature.

Table 3. Peukert Coefficient and Intrinsic Discharge Capacity with Temperature.

Temperature	β/α	Peukert Coefficient	Q^0
$-20^{\circ} C$	0.66	1.087	4.9 ± 1.05
$-5^{\circ} C$	0.64	1.18	7.21 ± 1.13
$10^{\circ} C$	0.13	1.26	9.6 ± 1.2
$22^{\circ} C$	0.05	1.38	24.7 ± 1.1
$40^{\circ} C$	0.01	1.40	53.6 ± 1.2
$55^{\circ} C$	0.06	1.34	33.1 ± 1.1

6.6 Kinetic Charge Acceptance Analysis

The KCA procedure designed is mentioned in section 5.2.2 (ii) and the resulting discharge curves are shown in Figure 41a, b. Same charge scan rate of 10 mV/s is used for charging after discharging Pb surfaces at different scan rates. This type of asymmetric discharge and charge regime shows charging current comparison for Pb electrode discharged by extracting different discharge capacities. Charging current profiles for Pb discharged at 22°C from 1000 mV/s to 0.05 mV/s scan rates is shown in Figure 48. Charging profile of discharged Pb surface at fast scan rates show a sharp charging peak. The charging peak starts becoming broader for Pb discharged with slow scan rates and ultimately charge current plateaus for Pb discharged at 0.1 and 0.05 mV/s. This change in charge current indicates that charging the Pb electrode discharged with very slow scan rates takes longer than Pb discharged with fast scan rates.

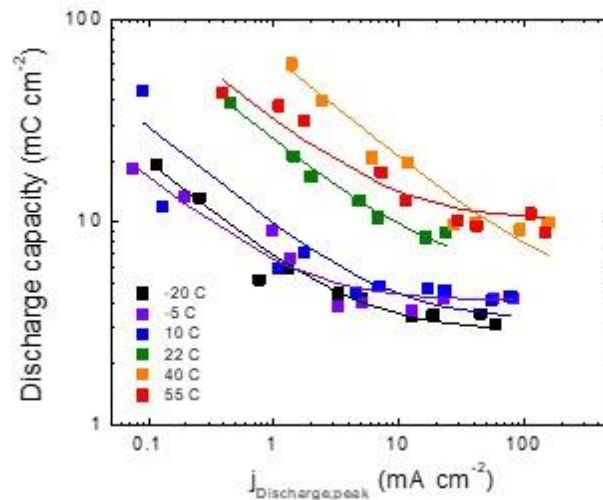


Figure 47. Charge vs peak current fitted to extended Peukert relationship.

It has been established that large $PbSO_4$ particles with higher thickness are formed when Pb is discharged with very slow scan rates and therefore it is difficult to recharge. This supports the assumption for deriving KCA dependence on $PbSO_4$ morphology that KCA is limited by dissolution of sulfate layer. Small lead sulphate particles are quick to dissolve which results in higher charge acceptance. Therefore, KCA is calculated using peak charge current and current at -1.2 V shown by dotted and dashed lines in Figure 48 such that mostly lead sulphate dissolution is considered, and HER potentials region is avoided. Since $PbSO_4$ dissolution is influenced by temperature of the system, we studied how KCA varies at various temperatures.

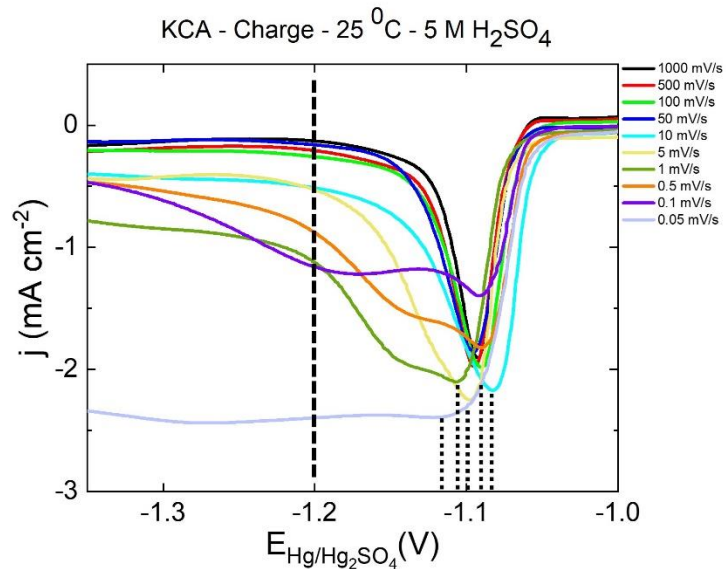


Figure 48. 10 mV/s charge scans for Pb surface discharged with scan rates from 1000 mV/s to 0.05 mV/s .

The corrected KCA_{Peak} calculated as in Equation 49 with charge current at peak is plotted against corrected thickness which is calculated using Equation 50.

Comparison of KCA plots for all temperature are shown in Figure 49a and b. Highest rate transient charge acceptance of Pb is studied by choosing charge current at peak for KCA_{Peak} analysis. KCA_{Peak} is greatly improved with increase in temperature if KCA_{Peak} for same thickness on x-axis in Figure 49a is compared. This improvement in KCA is because of the accelerated dissolution of $PbSO_4$ at higher temperature since KCA is proportional to k_{diss} and has inverse proportionality with d_0 .

In Figure 49b, charge current at -1.2 V is used for $KCA_{@ -1.2V}$ calculation and plotted against corrected thickness calculated according to Equation 49. By pushing potential limit to more negative value of -1.2 V, the sulfate dissolution and charge acceptance at steady state is evaluated. $KCA_{@ -1.2V}$ shows increasing trend with temperature but only at highest sulfate thickness. As the sulfate thickness goes down, highest $KCA_{@ -1.2V}$ reveals a critical sulphate thickness of approximately 10 nm where the KCA is at all temperatures is approximately same and beyond critical thickness KCA is not improved with temperature. Charge acceptance in $KCA_{@ -1.2V}$ becomes slower at higher $PbSO_4$ thickness with worse performance seen at $-20^{\circ}C$.

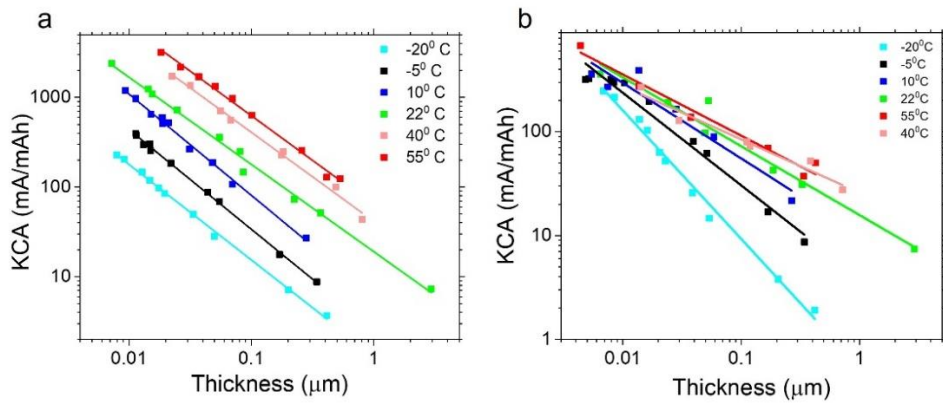


Figure 49. KCA calculated using charge current (a) peak charge current (KCA_{Peak}) and (b) -1.2 V ($KCA_{@ -1.2V}$) plotted against corrected $PbSO_4$ thickness.

A noticeable difference between high-rate charge acceptance from KCA_{Peak} and steady state charge acceptance from $KCA_{@-1.2V}$ is at $40^{\circ}C$ and $55^{\circ}C$ with higher KCA_{Peak} values than $KCA_{@-1.2V}$ at same $PbSO_4$ thickness. This indicates $PbSO_4$ dissolution kinetics is higher at peak current and slows down after the peak. Steady state charge acceptance shows little improvement at temperatures of $22^{\circ}C$, $40^{\circ}C$ and $55^{\circ}C$.

6.7 $PbSO_4$ Layer Thickness

Freshly electropolished Pb samples discharged to 100% DOD at 5 mV/s and 0.5 mV/s are chosen for $PbSO_4$ layer thickness observation by taking a cross-section using FIB-SEM. From SEM and AFM images of discharged Pb surfaces, it has been observed that $PbSO_4$ particles grow with distinct shape here addressed as $PbSO_4$ ‘spiders’ pointed out in SEM image of Pb samples discharged with 5 mV/s at $22^{\circ}C$ shown in Figure 50a. Cross-sections are taken at the center of $PbSO_4$ particle shown by green dashed line in the SEM image. At least 3 different spots are chosen for cross-sectional imaging of each sample.

The cross-section revealed three layers with different contrast, the top layer approximately 200 nm thickness of sputtered Au, a second layer of $PbSO_4$ sandwiched between top Au layer and bottom Pb metal surface shown in Figure 50b. Cross-section SEM images are tilt corrected such that the viewing angle is perpendicular to the cross-section to avoid errors in $PbSO_4$ layer measurement. Pb samples discharged with both sets of scan rates show increase in $PbSO_4$ thickness

with increase in temperature during discharge when images of same discharge scan rates are compared. Figure 51 and 52 shows Pb sample discharged with 5 mV/s and 0.5 mV/s discharge scan rate for all 6 temperatures.

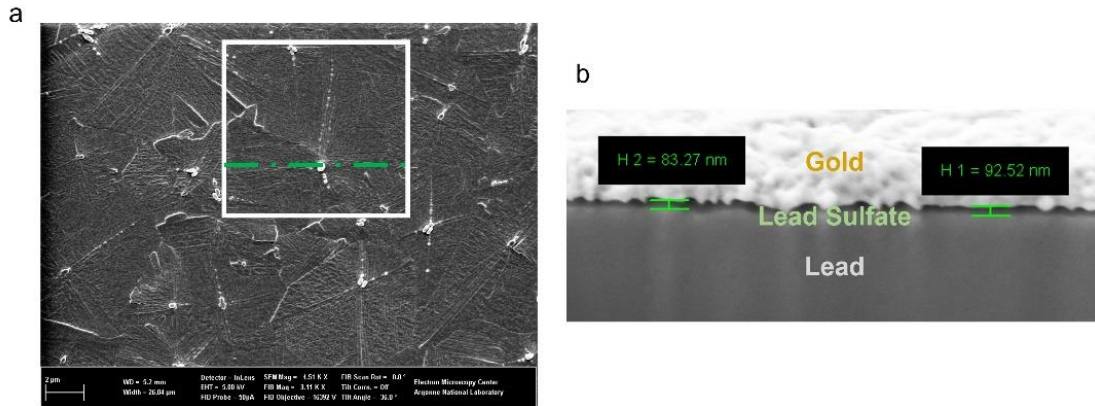


Figure 50. SEM image of Pb surface discharge with 5 mV/s scan rate at 22°C showing (a) top surface of $PbSO_4$ spider (b) Cross-section of Au, $PbSO_4$ and Pb layers.

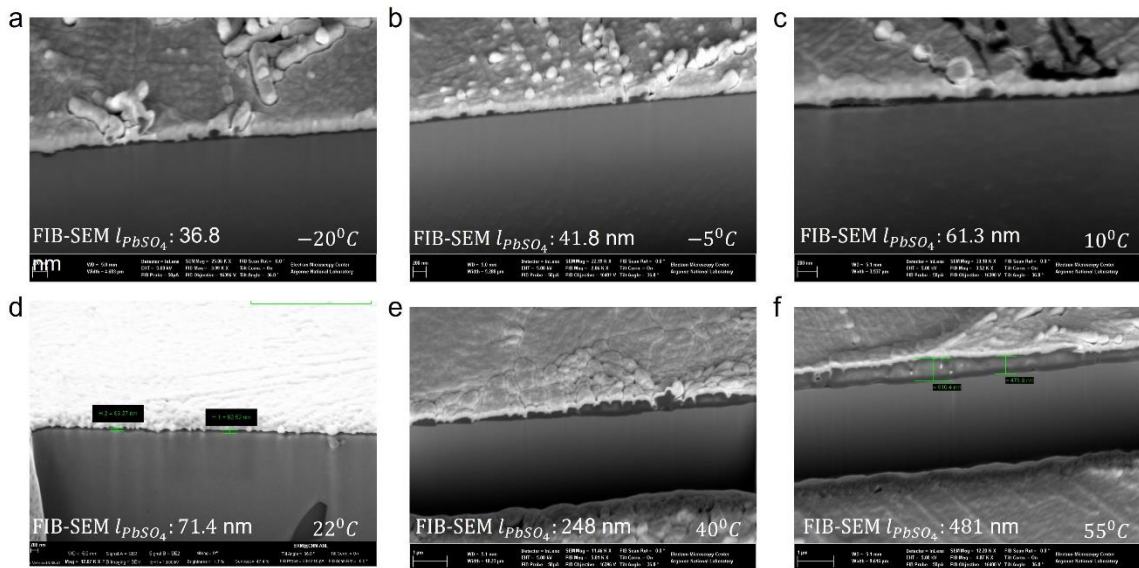


Figure 51. FIB-SEM cross-section Images of Pb discharged with 5 mV/s at (a) $-20^{\circ}C$, (b) $-5^{\circ}C$, (c) $10^{\circ}C$, (d) $22^{\circ}C$, (e) $40^{\circ}C$, (f) $55^{\circ}C$.

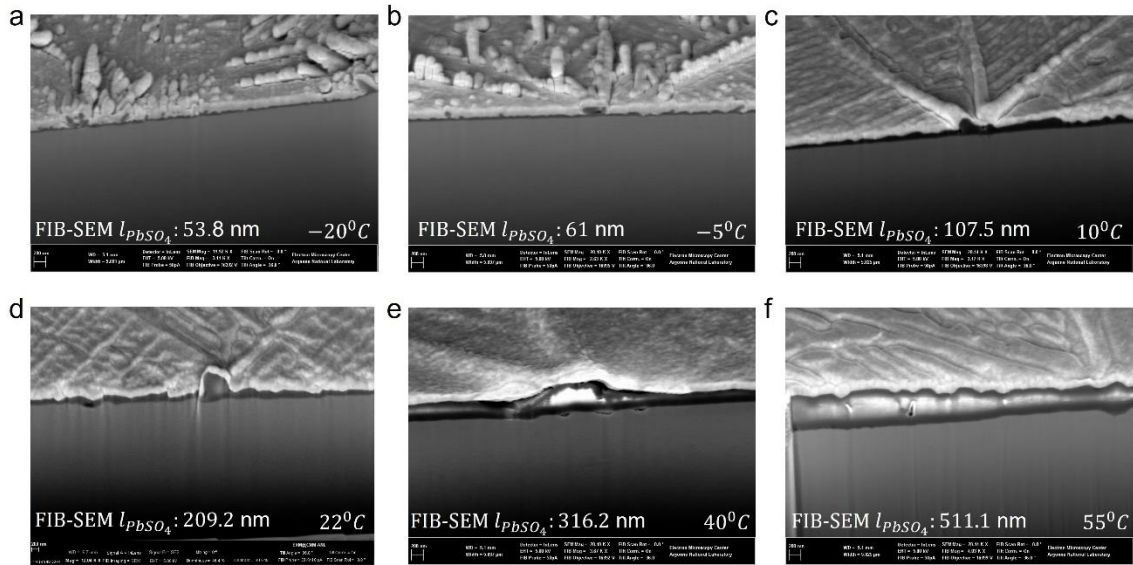


Figure 52. FIB-SEM cross-section Images of Pb discharged with 0.5 mV/s at (a) -20°C , (b) -5°C , (c) 10°C , (d) 22°C , (e) 40°C , (f) 55°C .



Figure 53. PbSO_4 average thickness measured in Imagej software.

Thickness measurements are done using two methods, first in the SEM software with digital measuring scale and second using ‘Imagej’ open-source software. Cross-section SEM image is loaded in the software and scale is defined in software using the scale bar in SEM image. The image of PbSO_4 layer is then divided into 1024 parts as the image contains 1024 pixels in horizontal direction.

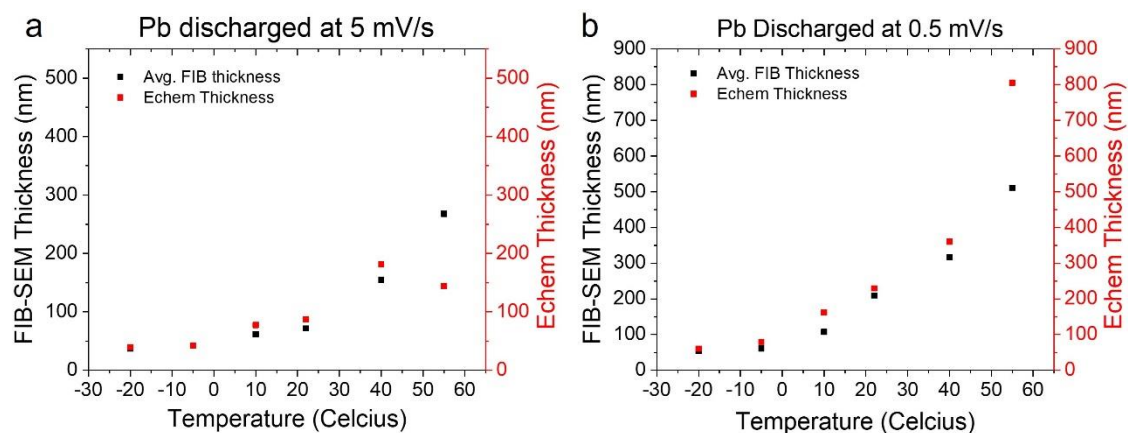


Figure 54. Comparison between electrochemical and measured $PbSO_4$ thickness.

Since $PbSO_4$ thickness is not uniform throughout the surface, individual thickness measurements are taken at every 25th pixel and an average thickness is calculated for $PbSO_4$ layer as shown in Figure 53. Electrochemical thickness of $PbSO_4$ layer is calculated from discharge capacity data using Equation 64 and it is compared with thickness measured by FIB-SEM. Figure 54a and b shows comparison of electrochemical l_{PbSO_4} and FIB-SEM measured l_{PbSO_4} . The calculated and measured thickness are in excellent agreement except for the results obtained at 55°C. The $PbSO_4$ thickness calculated using electrochemical data for higher temperature most likely has contribution from extra Pb^{2+} dissolution through the cracks and concentration change due to increased water loss.

6.8 Conductive Area of Discharged Pb Surface

Discharged Pb surface prepared for AFM using procedure mentioned in section 5.2.3. Passivated Pb surface covered with $PbSO_4$ layer is imaged using AFM PF-TUNA conductive microscope mode. $PbSO_4$ layer formed on Pb surface is

explored to identify conductive area of completely passivated surface. It was observed that $PbSO_4$ layer consist of tiny cracks which were detected using tunneling current between tip and sample surface by applying a DC voltage bias. These cracks may be playing important role in converting $PbSO_4$ back to Pb during charging process and may prove helpful in understanding electrical connectivity of electrode surface. AFM TUNA images of Pb samples discharge at various temperatures show a conductive area of $PbSO_4$ surface. Figures 55 and 56 show height images and TUNA images of Pb surface discharged at 5 mV/s. A comparison of height image and TUNA image indicates that this conductive area is due to cracks in passivation layer. AFM images show an obvious increase in $PbSO_4$ particle size with increase in temperature during discharge. And the TUNA image of the same area captured at the same time shows cracks inside $PbSO_4$ particles.

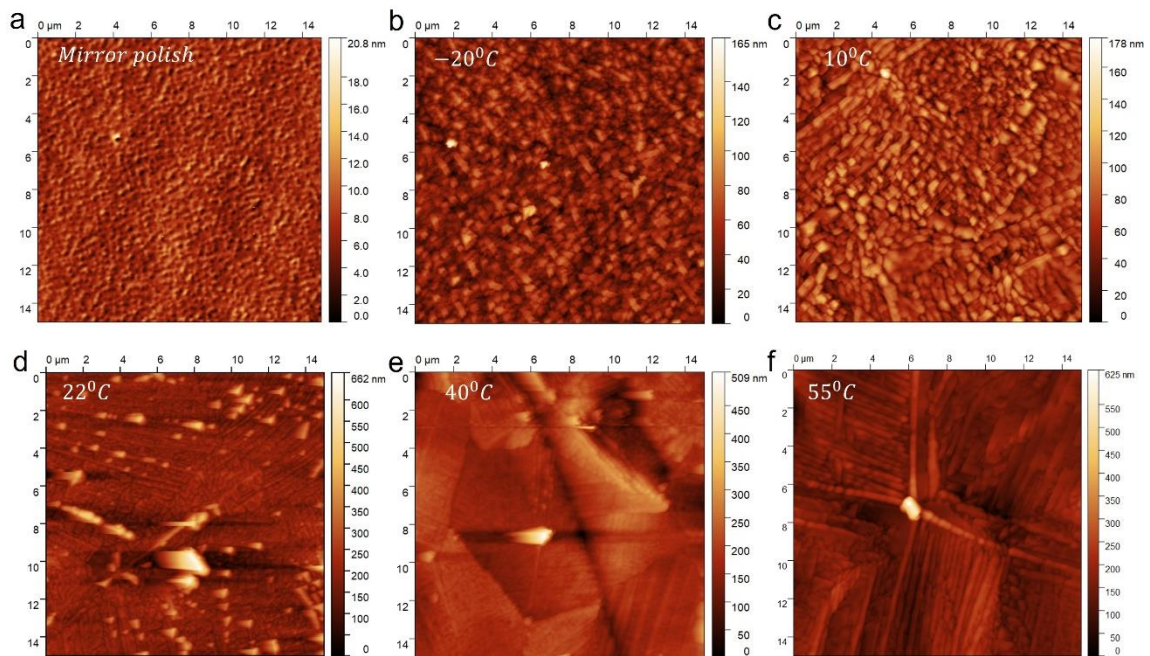


Figure 55. Height image showing $PbSO_4$ particles on discharge Pb surface at 5 mV/s.

In this section, an AFM TUNA image analysis method is proposed to quantify the conductive area of discharged surface. The images are analyzed in Imagej open-source software. First a scale defined for the TUNA image in the software using known size of AFM image and the image is converted to 8-bit format. The images have bright conductive areas and dark non-conductive areas. A global thresholding technique that uses single threshold value for entire image. A bimodal histogram of pixel intensity vs number of pixels is created that gives a threshold value for the image as shown in Figure 57.

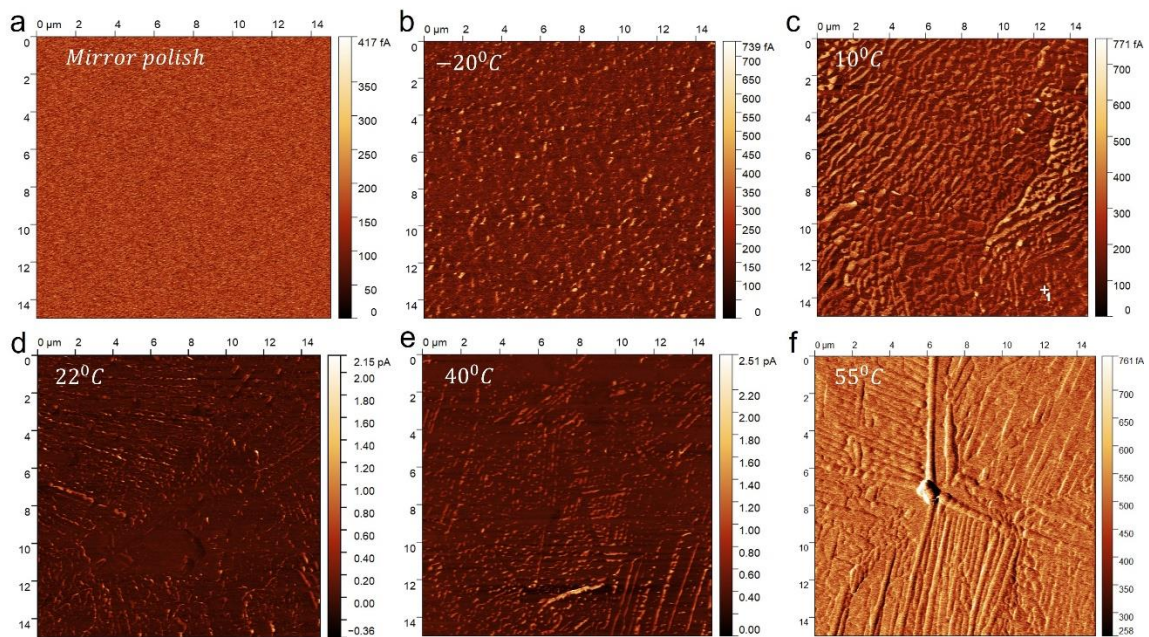


Figure 56. TUNA images of same sample area showing conductive area with pattern of crack on the surface.

Threshold value is used to separate the object from background. In this case, object is the conductive area of image and background in non-conductive area of image. Then a binary threshold image $g(x,y)$ is created with intensity value of 1

assigned for pixels of conductive area and 0 is assigned for pixels of non-conductive area in the image. The threshold image $g(x, y)$ is defined as

$$g(x, y) = \begin{cases} 1, & \text{if } (x, y) > T \\ 0, & \text{if } (x, y) < T \end{cases} \quad \text{Equation 67}$$

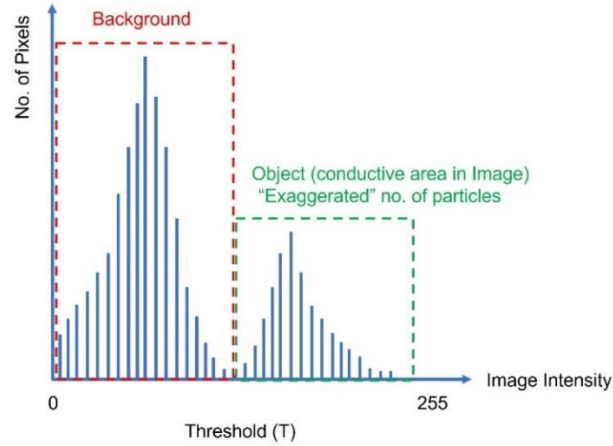


Figure 57. Bimodal histogram of TUNA image.

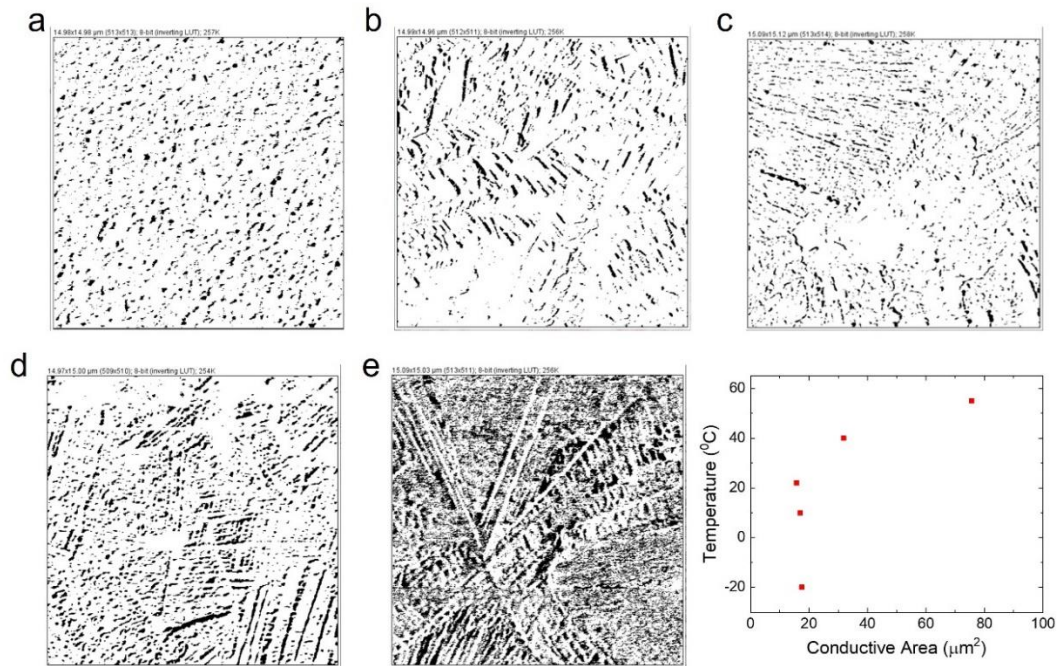


Figure 58. Threshold images of conductive area (a) -20°C , (b) 10°C , (c) 22°C , (d) 40°C , (e) 55°C , (f) Conductive area vs Temperature.

The threshold images showing conductive area in black and non-conductive area in white for Pb samples discharge with 5 mV/s at various temperatures is shown in Figure 58a-e. The bright area from TUNA image and dark area from threshold image are identical which confirms that the conductive area is separated from non-conductive area. The conductive area

The ‘Agglomerate of Spheres’ model used for deriving Peukert and KCA relationship with $PbSO_4$ morphology parameters can be used here assuming single layer $PbSO_4$ coverage on Pb surface for mathematical calculations of gaps in $PbSO_4$ spheres as shown in Figure 59. The area of spherical particle if radius, R is given as,

$$\text{Area}_{\text{covered}} = \frac{\pi}{2} R^2. \quad \text{Equation 68}$$

Area of gap between closely packed spheres is give as

$$\text{Area}_{\text{gap}} = \left(\sqrt{3} - \frac{\pi}{2} \right) R^2. \quad \text{Equation 69}$$

The exposed percent exposed area can be calculated using exposed surface fraction given as

$$\text{Exposed surface fraction} = \frac{\text{Area}_{\text{gap}}}{\text{Area}_{\text{covered}}}. \quad \text{Equation 70}$$

Therefore, exposed surface fraction is given as

$$\frac{2\sqrt{3} - \pi}{\pi} = 0.1026. \quad \text{Equation 71}$$

Assuming spherical shape of particles, mathematically calculated exposed area is about 10.26% of total area. The percent conductive area from threshold AFM TUNA

images of Pb discharged at temperatures from -20°C to 40°C is from 7% to 14% of total area which is close to mathematically calculated exposed area. For 55°C , more conductive area seen in AFM TUNA images indicates more cracks in PbSO_4 layer. More cracks in PbSO_4 layer most likely contribute to dissolution path for Pb^{2+} ion from underneath the PbSO_4 layer. This may be the reason for residual current transients in discharge curves at more positive potentials after the discharge peak. This may explain higher PbSO_4 thickness from electrochemical data than observed in FIB-SEM images.

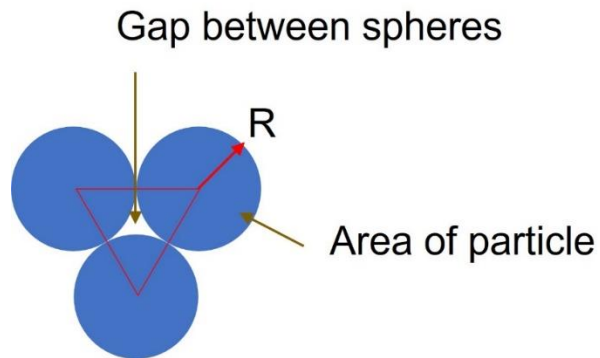


Figure 59. Area between spherical particles in 'Agglomerate of Spheres' model.

CONCLUSION

Conclusions from the research work in the dissertation are possible directions for future research work are discussed in this chapter. The first part will discuss the results from graphene synthesis. And second part will conclude the work on Pb electrode in 5 M H_2SO_4 , to explore fundamentals of negative electrode during discharge and charge at various temperatures.

The method developed for graphene synthesis is unique since it does not require complex equipment and uses all solid materials in inert atmosphere to produce good quality of graphene in copper. Raman maps of 2D peak for graphene proves graphene presence on copper after experiments. The 2D peak to G peak Raman intensity ratio of graphene synthesized using this method is about 0.86 to 0.9. Which indicates bilayer graphene with low defects since D peak intensity is lower than both G and 2D peaks. The graphene is weakly bonded to copper substrate therefore, it can be lifted from the surface as proved by using scotch tape exfoliation method. This method can be further developed to produce single layer graphene by studying various types of carbon dissolution in copper at high temperature and investigating quality of resulting graphene.

Lead electrode in lead-acid battery is investigated in this work for its baseline performance evaluation between temperatures of $-20^{\circ}C$ to $55^{\circ}C$. The advantage of investigation of electrode performed in this work is focuses examination of consistent Pb surface area undergoing changes during discharge and charge. An electropolished flat surface area revealed $PbSO_4$ morphological

development at various discharge rates and temperatures. A potentiostatic method is developed for analyzing Peukert relationship and KCA which can be used for studying not only lead-acid battery electrodes, but electrodes from other battery chemistries as well. An excellent resemblance of potentiostatic data to galvanostatic data has been shown so that scan rate can be used to control discharge and charge and the data can be related to real world battery operated under constant current. It has been concluded that $PbSO_4$ morphology depends on temperature at which it is discharged. Peukert coefficient and KCA are observed with temperature, and it is concluded that charge process is more sensitive to temperature. This observation along with High rate and steady state KCA can be used to improve charge acceptance of the electrode. Another important conclusion can be drawn is that control over $PbSO_4$ particle size and thickness can boost performance of lead-acid battery.

Further understanding of $PbSO_4$ layer formation and dissolution using in-situ AFM would be helpful in exploring nucleation and growth of $PbSO_4$ during discharge and dissolution during charge. Understanding these mechanisms on simple flat lead is essential since it is easier to use with imaging techniques. And the conclusions from flat Pb surface can be extrapolated to be used in pasted or any other electrode structures. Controlling electrode and $PbSO_4$ surface area by manufacturing electrode structures using lithography may prove useful. Performance for temperature stabilizing additives can be evaluated based on known standard performance of flat electrode.

REFERENCES

1. D. D. Sarma, A. K. Shukla, "Building better batteries: A travel back in time." *ACS Energy Letters*. **3** (2018), pp. 2841–2845.
2. D. Pavlov, in "Lead-Acid Batteries: Science and Technology." (Elsevier, 2011), pp. 3–28.
3. "The Rechargeable Battery Market and Main Trends 2018-2030" (2019).
4. "Lead Acid Battery Market Size Worth \$93.04 Billion By 2027," Grand view research, press report (February 2020).
5. U. Department of Energy, "Energy Storage Grand Challenge: Energy Storage Market Report" (2020).
6. K. R. Bullock, "Lead/acid batteries." *Journal of Power Sources*. **51**, 1–17 (1994).
7. J. Garche, in *Physical Chemistry Chemical Physics* (2001), vol. 3, pp. 356–367.
8. D. R. Battlebury, "A high performance lead–acid battery for EV applications." *Journal of Power Sources*. **80**, 7–11 (1999).
9. B. Hariprakash, A. U. Mane, S. K. Martha, S. A. Gaffoor, S. A. Shivashankar, A. K. Shukla, "A Low-Cost, High Energy-Density Lead/Acid Battery." *Electrochemical and Solid-State Letters*. **7** (2004), doi:10.1149/1.1645752.
10. SmithBucklin Statistics Group, "NATIONAL RECYCLING RATE STUDY," Chicago, Illinois (2019).

11. A. M. Genaidy, R. Sequeira, T. Tolaymat, J. Kohler, M. Rinder, "An exploratory study of lead recovery in lead-acid battery lifecycle in US market: An evidence-based approach." *Science of the Total Environment*. **407**, 7–22 (2008).
12. W. Zhang, J. Yang, X. Wu, Y. Hu, W. Yu, J. Wang, J. Dong, M. Li, S. Liang, J. Hu, R. V. Kumar, "A critical review on secondary lead recycling technology and its prospect." *Renewable and Sustainable Energy Reviews*. **61** (2016), pp. 108–122.
13. S. Machado Santos, J. Cabral Neto, M. Mendonça Silva, "Forecasting model to assess the potential of secondary lead production from lead acid battery scrap." *Environmental Science and Pollution Research*. **26**, 5782–5793 (2019).
14. Consortium for Battery Innovation, "Technical Roadmap," 2021.
15. Z.-I. Takehara, "Dissolution and precipitation reactions of lead sulfate in positive and negative electrodes in lead acid battery." *Journal of Power Sources*, **85** (1), pp. 29-37 (2000).
16. D. A. J. Rand, P. T. Moseley, in "Lead-Acid Batteries for Future Automobiles," J. Garche, E. Karden, P. T. Moseley, D. A. J. Rand, Eds. (Elsevier, Amsterdam, 2017), pp. 97–132.
17. M. A. (Martin A. Dasoiã, I. Avraamovich. Aguf, "*Current theory of lead acid batteries*," (Technicopy Limited, Stonehouse, 1979).

18. M. Paunovic, M. Schlesinger in "Fundamentals of Electrochemical Deposition" (John Wiley & Sons, Ltd, 2006), pp. 77–112.
19. D. Pavlov, in "Lead-Acid Batteries: Science and Technology," Ed. (Elsevier, Amsterdam, 2011), pp. 29–114.
20. K. R. Bullock, "The electromotive force of the lead-acid cell and its half-cell potentials." *Journal of Power Sources*. **35**, 197–223 (1991).
21. R. S. Treptow, "The Lead-Acid Battery: Its Voltage in Theory and in Practice." *Journal of Chemical Education*. **79**, 334 (2002).
22. K. R. Bullock, "The electromotive force of the lead-acid cell and its half-cell potentials." *Journal of Power Sources*. **35**, 197–223 (1991).
23. P. Delahay, M. Pourbaix, P. van Rysselberghe, "Potential-pH Diagram of Lead and its Applications to the Study of Lead Corrosion and to the Lead Storage Battery." *Journal of Electrochemical Society*. **98**(2), 57-64 (1951).
24. Y. Guo, "A New Potential-pH Diagram for an Anodic Film on Pb in H_2SO_4 ." *Journal of The Electrochemical Society*. **139**, 2114–2120 (1992).
25. P. Ruetschi, R. T. Angstadt, "Anodic Oxidation of Lead at Constant Potential." *Journal of The Electrochemical Society*. **111**, 1323 (1964).
26. R. Bianco, S. Wang, J. T. Hynes, in "Applications of Theoretical Methods to Atmospheric Science," M. E. Goodsite, M. S. Johnson, Eds. (Academic Press, 2008), vol. 55 of *Advances in Quantum Chemistry*, pp. 387–405.

27. A. v Levanov, O. Ya. Isaikina, U. D. Gurbanova, V. v Lunin, "Dissociation Constants of Perchloric and Sulfuric Acids in Aqueous Solution." *The Journal of Physical Chemistry B*. **122**, 6277–6286 (2018).
28. A. M. Margarella, K. A. Perrine, T. Lewis, M. Faubel, B. Winter, J. C. Hemminger, "Dissociation of sulfuric acid in aqueous solution: Determination of the photoelectron spectral fingerprints of H_2SO_4 , HSO_4^- , and SO_4^{2-} in water." *Journal of Physical Chemistry C*. **117**, 8131–8137 (2013).
29. D. A. Knopf, B. P. Luo, U. K. Krieger, T. Koop, "Thermodynamic Dissociation Constant of the Bisulfate Ion from Raman and Ion Interaction Modeling Studies of Aqueous Sulfuric Acid at Low Temperatures." *The journal of Physical Chemistry A*, **107**(21), 4322-4332 (2003), doi:10.1021/jp027775.
30. T. F. Young, L. A. Blatz, "The Variation of the Properties of Electrolytic Solutions with Degrees of Dissociation." *Chemical Reviews*. **44**, 93–115 (1949).
31. Y. Matsushima, A. Okuwaki, "The Second Dissociation Constant of Sulfuric Acid at Elevated Temperatures from Potentiometric Measurements." *Bulletin of the Chemical Society of Japan*. **61**, 3344–3346 (1988).
32. Y. C. Wu, D. Feng, "The second dissociation constant of sulfuric acid at various temperatures by the conductometric method." *Journal of Solution Chemistry*. **24**, 133–144 (1995).

33. H. Sippola, "Critical evaluation of the 2nd dissociation constants for aqueous sulfuric acid." *Thermochimica Acta*. **532**, 65–77 (2012).
34. V. Danel, V. Plichon, "Study of Pb (II) in various H₂O-H₂SO₄ mixtures by differential pulse polarography: solubility of lead sulphate, diffusion coefficient of Pb(II) and half-wave potential of Pb(Hg)/Pb(II)." *Electrochimica Acta*. **27**, 771–774 (1982).
35. H. D. Crockford, J. A. Addleston, "The Solubility of Lead Sulfate in Aqueous Solutions of Sulfuric Acid at High Concentrations." *The Journal of Physical Chemistry*. **40**, 303–305 (1936).
36. B. D. Nonnan Craig, G. W. Vinal, "SOLUBILITY OF LEAD SULFATE IN SOLUTIONS OF SULFURIC ACID, DETERMINED BY DITHIZONE WITH A PHOTRONIC CELL." *Journal of Research of National Bureau of Standards*, **22**, 55-70 (1939).
37. D. Pavlov, A. Kirchev, M. Stoycheva, B. Monahov, "Influence of H₂SO₄ concentration on the mechanism of the processes and on the electrochemical activity of the Pb/PbO₂/PbSO₄ electrode." *Journal of Power Sources*. **137**, 288–308 (2004).
38. J. McGinty, N. Yazdanpanah, C. Price, J. H. ter Horst, J. Sefcik, in "The Handbook of Continuous Crystallization" (The Royal Society of Chemistry, 2020), pp. 1–50.

39. A. Myerson, "Handbook of Industrial Crystallization" (Elsevier Science & Technology, Oxford, UNITED STATES, 2001).
40. W. A. G, "Nucleation of Crystals from Solution." *Science*. **148**, 601–607 (1965).
41. V. I. Kalikmanov, in "Nucleation Theory," Ed. (Springer Netherlands, Dordrecht, 2013), pp. 17–41.
42. J. J. de Yoreo, P. G. Vekilov, "Principles of Crystal Nucleation and Growth." *Reviews in Mineralogy and Geochemistry*. **54**, 57–93 (2003).
43. R. C. Snyder, M. F. Doherty, "Faceted crystal shape evolution during dissolution or growth." *AIChE Journal*. **53**, 1337–1348 (2007).
44. T. Chiku, K. Nakajima, "Formation of $PbSO_4$ Crystallites on Pb in the Lead-Acid Cell." *Journal of The Electrochemical Society*. **118**, 1395 (1971).
45. S. Trasatti, "Work function, electronegativity, and electrochemical behaviour of metals: III. Electrolytic hydrogen evolution in acid solutions." *Journal of Electroanalytical Chemistry and Interfacial Electrochemistry*. **39**, 163–184 (1972).
46. G. Burstein, "A hundred years of Tafel's Equation: 1905–2005." *CORROS SCI*. **47**, 2858–2870 (2005).
47. F. Wang, C. Hu, M. Zhou, K. Wang, J. Lian, J. Yan, S. Cheng, K. Jiang, "Research progresses of cathodic hydrogen evolution in advanced lead–acid batteries." *Science Bulletin*. **61**, 451–458 (2016).

48. S. Kang, M. Shang, M. A. Spence, M. Andrew, S. Liu, J. Niu, "Dynamic charge acceptance and hydrogen evolution of a new MXene additive in advanced lead-acid batteries via a rapid screening three-electrode method." *Chem. Commun.* **54**, 3456–3459 (2018).
49. M. A. Deyab, "Hydrogen evolution inhibition by l-serine at the negative electrode of a lead–acid battery." *RSC Advances*. **5**, 41365–41371 (2015).
50. J. O. Bockris, S. Srinivasan, "Elucidation of the mechanism of electrolytic hydrogen evolution by the use of H-T separation factors." *Electrochimica Acta*. **9**, 31–44 (1964).
51. D. Pavlov, in "Lead-Acid Batteries: Science and Technology," Ed. (Elsevier, Amsterdam, 2011), pp. 311–361.
52. E. Ebner, D. Burow, J. Panke, A. Börger, A. Feldhoff, P. Atanassova, J. Valenciano, M. Wark, E. Rühl, "Carbon blacks for lead-acid batteries in micro-hybrid applications – Studied by transmission electron microscopy and Raman spectroscopy." *Journal of Power Sources*. **222**, 554–560 (2013).
53. X. Li, Y. Zhang, Z. Su, Y. Zhao, X. Zhao, R. Wang, "Graphene nanosheets as backbones to build a 3D conductive network for negative active materials of lead–acid batteries." *Journal of Applied Electrochemistry*. **47**, 619–630 (2017).
54. H.-Y. Hu, N. Xie, C. Wang, L.-Y. Wang, R. Privette, H.-F. Li, M. Pan, F. Wu, X.-L. Yan, B.-B. Jiang, M. Wu, K. Vinodgopal, G. Dai, "Enhanced Performance of E-

- Bike Motive Power Lead–Acid Batteries with Graphene as an Additive to the Active Mass.” *ACS Omega*. **3**, 7096–7105 (2018).
55. S. Logeshkumar, R. Manoharan, “Influence of some nanostructured materials additives on the performance of lead acid battery negative electrodes.” *Electrochimica Acta*. **144**, 147–153 (2014).
 56. J. Garche, P. T. Moseley, E. Karden, in “Advances in Battery Technologies for Electric Vehicles,” B. Scrosati, J. Garche, W. Tillmetz, Eds. (Woodhead Publishing, 2015), pp. 75–101.
 57. P. T. Moseley, R. F. Nelson, A. F. Hollenkamp, “The role of carbon in valve-regulated lead–acid battery technology.” *Journal of Power Sources*. **157**, 3–10 (2006).
 58. O. J. Dada, “Higher capacity utilization and rate performance of lead acid battery electrodes using graphene additives.” *Journal of Energy Storage*. **23**, 579–589 (2019).
 59. P. Křivík, K. Micka, P. Bača, K. Tonar, P. Tošer, “Effect of additives on the performance of negative lead-acid battery electrodes during formation and partial state of charge operation.” *Journal of Power Sources*. **209**, 15–19 (2012).
 60. M. Shiomi, T. Funato, K. Nakamura, K. Takahashi, M. Tsubota, “Effects of carbon in negative plates on cycle-life performance of valve-regulated lead/acid batteries.” *Journal of Power Sources*. **64**, 147–152 (1997).

61. K. Nakamura, M. Shiomi, K. Takahashi, M. Tsubota, "Failure modes of valve-regulated lead/acid batteries." *Journal of Power Sources*. **59**, 153–157 (1996).
62. D. Pavlov, P. Nikolov, T. Rogachev, "Influence of expander components on the processes at the negative plates of lead-acid cells on high-rate partial-state-of-charge cycling. Part II. Effect of carbon additives on the processes of charge and discharge of negative plates." *Journal of Power Sources*. **195**, 4444–4457 (2010).
63. V. Naresh, U. Bhattacharjee, S. K. Martha, "Boron doped graphene nanosheets as negative electrode additive for high-performance lead-acid batteries and ultracapacitors." *Journal of Alloys and Compounds*. **797**, 595–605 (2019).
64. M. Fernández, J. Valenciano, F. Trinidad, N. Muñoz, "The use of activated carbon and graphite for the development of lead-acid batteries for hybrid vehicle applications." *Journal of Power Sources*. **195**, 4458–4469 (2010).
65. L. A. Yolshina, V. A. Yolshina, A. N. Yolshin, S. v Plaksin, "Novel lead-graphene and lead-graphite metallic composite materials for possible applications as positive electrode grid in lead-acid battery." *Journal of Power Sources*. **278**, 87–97 (2015).
66. H.-Y. Hu, N. Xie, C. Wang, L.-Y. Wang, R. M. Privette, H.-F. Li, M. Pan, F. Wu, X.-L. Yan, B.-B. Jiang, M. H. Wu, K. Vinodgopal, G.-P. Dai, "Enhanced Performance of E-Bike Motive Power Lead–Acid Batteries with Graphene as an Additive to the Active Mass." *ACS Omega*. **3**, 7096–7105 (2018).

67. H. Wei, J. Yang, W. Liu, J. Tai, S. Ji, F. Li, L. Lei, "Effects of sulfonated graphene on lead sulfate negative electrode of Pb-C batteries." *Journal of Energy Storage*. **34**, 102174 (2021).
68. J. Wang, L. Dong, M. Liu, J. Wang, Q. Shao, A. Li, W. Yan, J. C.-Y. Jung, J. Zhang, "Significantly improved high-rate partial-state-of-charge performance of lead-acid batteries induced by trace amount of graphene oxide nanosheets." *Journal of Energy Storage*. **29**, 101325 (2020).
69. M. Gelbke, C. Mondoloni, in "Lead-Acid Batteries for Future Automobiles," (Elsevier, Amsterdam, 2017), pp. 149–184.
70. D. Rand, in "SECONDARY BATTERIES-LEAD-ACID SYSTEMS." Pp. 550-575 (2018).
71. M. Kwiecien, P. Schröer, M. Kuipers, D. U. Sauer, in "Lead-Acid Batteries for Future Automobiles," (Elsevier, Amsterdam, 2017), pp. 133–146.
72. D. W. H. Lambert, P. H. J. Greenwood, M. C. Reed, "Advances in gelled-electrolyte technology for valve-regulated lead-acid batteries." *Journal of Power Sources*. **107**, 173–179 (2002).
73. J. Albers, E. Meissner, in "Lead-Acid Batteries for Future Automobiles," (Elsevier, Amsterdam, 2017), pp. 185–211.
74. D. Pavlov, in "Valve-Regulated Lead-Acid Batteries," (Elsevier, Amsterdam, 2004), pp. 37–108.

75. R. F. Nelson, in "Valve-Regulated Lead-Acid Batteries," (Elsevier, Amsterdam, 2004), pp. 241–293.
76. P. T. Moseley, "Consequences of including carbon in the negative plates of Valve-regulated Lead–Acid batteries exposed to high-rate partial-state-of-charge operation." *Journal of Power Sources*. **191**, 134–138 (2009).
77. L. T. Lam, R. Louey, N. P. Haigh, O. v Lim, D. G. Vella, C. G. Phyland, L. H. Vu, J. Furukawa, T. Takada, D. Monma, T. Kano, "VRLA Ultrabattery for high-rate partial-state-of-charge operation." *Journal of Power Sources*. **174**, 16–29 (2007).
78. G. J. May, A. Davidson, B. Monahov, "Lead batteries for utility energy storage: A review." *Journal of Energy Storage*. **15**, 145–157 (2018).
79. T. Hund, N. Clark, W. Baca, in "*18th, International Seminar on Double Layer Capacitors and Hybrid Energy Storage Devices*" (Redox Engineering; [United States], Deerfield Beach, FL), pp. 195–207.
80. D. Cericola, R. Kötz, "Hybridization of rechargeable batteries and electrochemical capacitors: Principles and limits." *Electrochimica Acta*. **72**, 1–17 (2012).
81. J. Furukawa, T. Takada, D. Monma, L. T. Lam, "Further demonstration of the VRLA-type UltraBattery under medium-HEV duty and development of the flooded-type UltraBattery for micro-HEV applications." *Journal of Power Sources*. **195**, 1241–1245 (2010).

82. J. Furukawa, K. Smith, L. T. Lam, D. A. J. Rand, in "Lead-Acid Batteries for Future Automobiles," (Elsevier, Amsterdam, 2017), pp. 349–391.
83. A. Cooper, J. Furakawa, L. Lam, M. Kellaway, "The UltraBattery—A new battery design for a new beginning in hybrid electric vehicle energy storage." *Journal of Power Sources*. **188**, 642–649 (2009).
84. E. Ebner, A. Börger, M. Gelbke, E. Zena, M. Wieger, "Temperature-dependent formation of vertical concentration gradients in lead-acid batteries under PSoC operation – Part 1: Acid stratification." *Electrochimica Acta*. **90**, 219–225 (2013).
85. A. Cooper, P. T. Moseley, "Progress in overcoming the failure modes peculiar to VRLA batteries." *Journal of Power Sources*. **113**, 200–208 (2003).
86. K. Tomantschger, "Effects of electrolyte agitation on the performance of lead—acid traction batteries at various temperatures." *Journal of Power Sources*. **13**, 137–149 (1984).
87. B. Culpin, D. A. J. Rand, "Failure modes of lead/acid batteries." *Journal of Power Sources*. **36**, 415–438 (1991).
88. J. Yang, C. Hu, H. Wang, K. Yang, J. B. Liu, H. Yan, "Review on the research of failure modes and mechanism for lead–acid batteries." *International Journal of Energy Research*. **41**, 336–352 (2017).

89. D. Pavlov, P. Nikolov, "Lead–Carbon Electrode with Inhibitor of Sulfation for Lead-Acid Batteries Operating in the HRPSoC Duty." *Journal of The Electrochemical Society*. **159**, A1215–A1225 (2012).
90. G. C. Zguris, "A review of physical properties of separators for valve-regulated lead/acid batteries." *Journal of Power Sources*. **59**, 131–135 (1996).
91. R. Wagner, "Failure modes of valve-regulated lead/acid batteries in different applications." *Journal of Power Sources*. **53**, 153–162 (1995).
92. H. Cao, Q. Yu, R. Colby, D. Pandey, C. S. Park, J. Lian, D. Zemlyanov, I. Childres, V. Drachev, E. A. Stach, M. Hussain, H. Li, S. S. Pei, Y. P. Chen, "Large-scale graphitic thin films synthesized on Ni and transferred to insulators: Structural and electronic properties." *Journal of Applied Physics*. **107**, 044310 (2010).
93. W. Wu, Z. Liu, L. A. Jauregui, Q. Yu, R. Pillai, H. Cao, J. Bao, Y. P. Chen, S.-S. Pei, "Wafer-scale synthesis of graphene by chemical vapor deposition and its application in hydrogen sensing." *Sensors and Actuators B: Chemical*. **150**, 296–300 (2010).
94. J. Campos-Delgado, A. R. Botello-Méndez, G. Algara-Siller, B. Hackens, T. Pardoén, U. Kaiser, M. S. Dresselhaus, J.-C. Charlier, J.-P. Raskin, "CVD synthesis of mono- and few-layer graphene using alcohols at low hydrogen concentration and atmospheric pressure." *Chemical Physics Letters*. **584**, 142–146 (2013).

95. R. Colby, Q. Yu, H. Cao, S. S. Pei, E. A. Stach, Y. P. Chen, "Cross-sectional transmission electron microscopy of thin graphite films grown by chemical vapor deposition." *Diamond and Related Materials*. **19**, 143–146 (2010).
96. J.-M. Aguiar-Hualde, Y. Magnin, H. Amara, C. Bichara, "Probing the role of carbon solubility in transition metal catalyzing single-walled carbon nanotubes growth." *Carbon*. **120**, 226–232 (2017).
97. Q. Yu, L. A. Jauregui, W. Wu, R. Colby, J. Tian, Z. Su, H. Cao, Z. Liu, D. Pandey, D. Wei, T. F. Chung, P. Peng, N. P. Guisinger, E. A. Stach, J. Bao, S.-S. Pei, Y. P. Chen, "Control and characterization of individual grains and grain boundaries in graphene grown by chemical vapour deposition." *Nature Materials*. **10**, 443–449 (2011).
98. H. A. Calderon, I. Estrada-Guel, F. Alvarez-Ramírez, V. G. Hadjiev, F. C. Robles Hernandez, "Morphed graphene nanostructures: Experimental evidence for existence." *Carbon*. **102**, 288–296 (2016).
99. C. Mattevi, H. Kim, M. Chhowalla, "A review of chemical vapour deposition of graphene on copper." *Journal of Materials Chemistry*. **21**, 3324–3334 (2011).
100. M. G. Cugnet, M. Dubarry, B. Y. Liaw, "Peukert's Law of a Lead-Acid Battery Simulated by a Mathematical Model." *ECS Transactions*. **25**, 223–233 (2019).
101. A. Manenti, S. Onori, Y. Guezennec, "A New Modeling Approach to Predict 'Peukert Effect' for Lead Acid Batteries." *IFAC Proceedings Volumes*. **44**, 12289–12294 (2011).

102. A. Manenti, S. Onori, Y. Guezennec, "A New Modeling Approach to Predict 'Peukert Effect' for Lead Acid Batteries." *IFAC Proceedings Volumes*. **44**, 12289–12294 (2011).
103. D. Doerffel, S. A. Sharkh, "A critical review of using the Peukert equation for determining the remaining capacity of lead-acid and lithium-ion batteries." *Journal of Power Sources*. **155**, 395–400 (2006).
104. N. Omar, P. van den Bossche, T. Coosemans, J. van Mierlo, "Peukert Revisited—Critical Appraisal and Need for Modification for Lithium-Ion Batteries." *Energies*. **6**, 5625–5641 (2013).
105. N. E. Galushkin, N. N. Yazvinskaya, D. N. Galushkin, "A Critical Review of Using the Peukert Equation and its Generalizations for Lithium-Ion Cells." *Journal of The Electrochemical Society*. **167**, 120516 (2020).
106. H. Yang, "Application of Peukert's law in supercapacitor discharge time prediction." *Journal of Energy Storage*. **22**, 98–105 (2019).
107. J. Garche, P. T. Moseley, E. Karden, in "Advances in Battery Technologies for Electric Vehicles," (Woodhead Publishing, 2015), pp. 75–101.
108. M. J. Smith, D. T. Gladwin, D. A. Stone, "An Analysis of the Influence of High-Frequency Ripple Currents on Dynamic Charge Acceptance," *Journal of Energy Storage*, **22**, 27-35 (2019).
109. M. J. Smith, D. T. Gladwin, D. A. Stone, "Experimental analysis of dynamic charge acceptance test conditions for lead-acid cells." *IECON 2016 - 42nd*

Annual Conference of the IEEE Industrial Electronics Society, 2046–2051 (2016).

110. H. A. Calderon, A. Okonkwo, I. Estrada-Guel, V. G. Hadjiev, F. Alvarez-Ramírez, F. C. Robles Hernández, “HRTEM low dose: the unfold of the morphed graphene, from amorphous carbon to morphed graphenes.” *Advanced Structural and Chemical Imaging*. **2**, 10 (2016).
111. H. A. Calderon, I. Estrada-Guel, F. Alvarez-Ramírez, V. G. Hadjiev, F. C. Robles Hernandez, “Morphed graphene nanostructures: Experimental evidence for existence.” *Carbon*. **102**, 288–296 (2016).
112. A. C. Ferrari, J. C. Meyer, V. Scardaci, C. Casiraghi, M. Lazzeri, F. Mauri, S. Piscanec, D. Jiang, K. S. Novoselov, S. Roth, A. K. Geim, “Raman Spectrum of Graphene and Graphene Layers.” *Physical Review Letters*. **97**, 187401 (2006).
113. P. Vandenabeele, D. J. Ando, “Practical Raman Spectroscopy: An Introduction” (John Wiley & Sons, Incorporated, Hoboken, UNITED KINGDOM, 2013).
114. J. S. Park, A. Reina, R. Saito, J. Kong, G. Dresselhaus, M. S. Dresselhaus, “G’ band Raman spectra of single, double and triple layer graphene.” *Carbon*. **47**, 1303–1310 (2009).
115. L. M. Malard, M. A. Pimenta, G. Dresselhaus, M. S. Dresselhaus, Raman spectroscopy in graphene. *Physics Reports*. **473**, 51–87 (2009).
116. M. Wall, “The Raman Spectroscopy of Graphene and the Determination of Layer Thickness.” *Thermo Fisher Scientific*, Madison, WI, USA (2011).

117. I. Childres, L. A. Jauregui, W. Park, H. Cao, Y. P. Chen, "Raman spectroscopy of graphene and related materials." *New developments in photon and materials research*. **1** (2013).
118. Allen J. Bard and Larry R. Faulkner, "Electrochemical Methods: Fundamentals and Applications," New York: Wiley, 2001, 2nd ed. *Russian Journal of Electrochemistry*. **38**, 1364–1365 (2002).
119. K. J. VETTER, in "Electrochemical Kinetics," (Academic Press, 1967), pp. 1–103.
120. M. Chen, Z. A. H. Goodwin, G. Feng, A. A. Kornyshev, "On the temperature dependence of the double layer capacitance of ionic liquids." *Journal of Electroanalytical Chemistry*. **819**, 347–358 (2018).
121. S. A. Watzele, L. Katzenmeier, J. P. Sabawa, B. Garlyyev, A. S. Bandarenka, "Temperature dependences of the double layer capacitance of some solid/liquid and solid/solid electrified interfaces. An experimental study." *Electrochimica Acta*. **391**, 138969 (2021).
122. D. M. Morales, M. Risch, "Seven steps to reliable cyclic voltammetry measurements for the determination of double layer capacitance." *Journal of Physics: Energy* (2021), doi:10.1088/2515-7655/abee33.
123. M. Raimondo, L. Guadagno, L. Vertuccio, C. Naddeo, G. Barra, G. Spinelli, P. Lamberti, V. Tucci, K. Lafdi, "Electrical conductivity of carbon nanofiber

reinforced resins: Potentiality of Tunneling Atomic Force Microscopy (TUNA) technique." *Composites Part B: Engineering*. **143**, 148–160 (2018).